# Intramolecular π–π Interactions with a Chiral Auxiliary Ligand Control Diastereoselectivity in a Cyclometalated Ir(III) Complex

Daniel G. Congrave,[1] Andrei S. Batsanov,[1] Mingxu Du,[2] Yu Liu,[2]* Dongxia Zhu,[3]* Martin R. Bryce[1]*

[1]Department of Chemistry, Durham University, South Road, Durham DH1 3LE, UK
[2] State Key Laboratory of Supramolecular Structure and Materials, College of Chemistry, Jilin University, Changchun 130012, People's Republic of China
[3]Key Laboratory of Nanobiosensing and Nanobioanalysis at Universities of Jilin Province, Department of Chemistry, North-east Normal University, 5268 Renmin Street, Changchun, Jilin 130024, People's Republic of China

*Supporting Information Placeholder*

**ABSTRACT:** The application of a chiral auxiliary ligand to control the diastereoselectivity in the synthesis of a cyclometalated iridium(III) complex is presented. The diastereomeric iridium(III) complexes **1a** and **1b** are reported in which a phenoxyoxazoline auxiliary ligand incorporates a chiral center functionalized with a pendant pentafluorophenyl group. The diastereomers were readily separated and their structural, electrochemical and photophysical properties are discussed. Solution-state NMR data and X-ray crystal structures establish that the pentafluorophenyl group engages in intramolecular π–π interactions. The X-ray analysis reveals that the two diastereomers display very different modes of intramolecular stacking. The variable temperature $^{19}$F NMR data indicate that rotation of the pendant pentafluorophenyl rings in **1b** and **1a** is a temperature dependent process, and that there is a smaller energy barrier to rotation in **1b** compared to **1a**. This correlates with variable temperature photoluminescence data which show that upon heating the integrated emission intensity is reduced substantially more for **1b** than for **1a**, which is ascribed to the enhanced rotation in **1b** providing a more easily populated non-radiative pathway compared to **1a**. These experimental data are supported by computational calculations. Phosphorescent organic light emitting devices (PhOLEDs) using **1a** as the dopant complex give blue-green emission with a high maximum external quantum efficiency ($EQE_{max}$) of 25.8% (at *ca.* 270 cd m$^{-2}$) and with a low efficiency roll-off to 24.9% at 1000 cd m$^{-2}$. Our results extend the scope of ligand design for cyclometalated iridium complexes which possess interesting structural and emission properties.

## INTRODUCTION

Iridium(III) complexes have been widely studied in applications[1,2] such as photocatalysis,[3] biological labelling,[4] sensing[5] and as emitters in highly efficient phosphorescent organic light-emissive devices (PhOLEDs)[6–12] They possess a range of advantageous properties such as high luminescence quantum efficiency (Φ), microsecond-scale phosphorescence lifetime (τ) and good electrochemical stability, while their metal-ligand based photochemistry has enabled their emission colour to be tuned across the entire visible spectrum through appropriate synthetic modification.[13–15]

Notably, highly phosphorescent heteroleptic complexes have received significant interest because they can be synthesized under milder conditions than *fac*-homoleptic complexes, allowing a wider scope for structural variation.[16–19] They typically feature two cyclometalating C^N chelates, which function as luminophores, alongside a 3$^{rd}$ auxiliary ligand that is not directly involved in the excited state (ancillary), but instead can influence emission color and orbital mixing through tuning the energy of the Ir d orbitals.[20–26]

An interesting way to alter this classic system is through the incorporation of phenoxyazole-based ligands as the 3$^{rd}$ chelate, which provides unusual complexes where the auxiliary ligands feature significant frontier orbital contribution. Several highly emissive derivatives have been reported by our group and others, including application in efficient PhOLEDs.[27–30] Particularly, we have established that synthetic modification of such auxiliary ligands can be used to control emission color through tuning either the frontier orbital energies or the emission bandwidth.[28,29]

Non-covalent interactions are another promising tool for altering the photophysical properties of luminophores.[31,32] Their incorporation can offer synthetic control while avoiding the difficulties associated with the construction of covalent bonds. For example, in a sky-blue bis[2-(4,6-difluorophenyl)pyridinato-C$^2$,*N*](picolinato)iridium(III) (FIrpic)-based system, comparison of hydroxy and methoxy-substituted derivatives unequivocally established that intramolecular hydrogen bonding decreased the non-radiative decay rate ($k_{nr}$) by an order of magnitude, and increased PhOLED operating time by over 50%.[31]

Intramolecular π–π stacking has been incorporated into a few specific iridium complexes[33–38] and has been shown to improve the operational stability of light-emitting electrochemical cells (LEECs).[33] Also, intramolecular π–π interactions can rigidify complexes, thereby enhancing their photoluminescence quantum yields (PLQYs) [35,38] when perfluoroaryl groups are included to augment stacking.[39–41] However, it is difficult to determine the exact consequences of intramolecular stacking, as its presence/absence inevitably alters secondary electronic and/or steric factors.[39,42–44]

In this study we intended to circumvent this issue by studying the new diastereomeric complexes **1a** and **1b** (Figure 1). Their phenoxyoxazoline auxiliary ligands (**6** – Figure 2) incorporate a chiral center functionalized with a pendant pentafluorophenyl group. As **1a** and **1b** are diastereomeric, they are expected to have near-identical electronic properties. However, the pentafluorophenyl ring was expected to display different stacking modes in **1a** and **1b**.[30,45] Consequently, it was anticipated that any significant differences in the photophysical properties of **1a** and **1b** would be specifically related to the nature of their intramolecular π–π interactions.

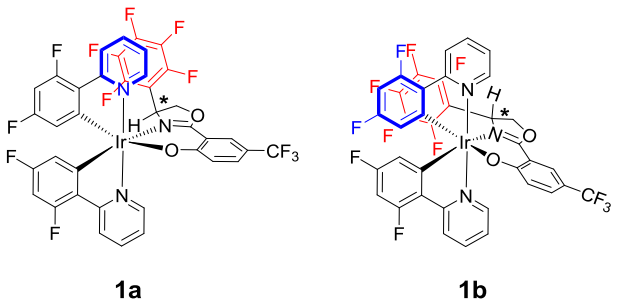


**Figure 1.** Structures of diastereomeric complexes **1a** and **1b** with their 3D configurations. The colored rings engage in intramolecular π–π interactions.

The diastereomers **1a** and **1b** were separated and their structural, electrochemical and photophysical properties are reported. Experimental data are supported by a density functional theory (DFT) study. Particularly, variable temperature (VT) $^{19}$F NMR and photoluminescence (PL) measurements provide insights into the influence of the intramolecular π–π interactions on the solution photophysical properties of **1a** and **1b**. Vacuum-processed PhOLEDs doped with **1a** as the emitter demonstrate notably good performance for a perfluoroaryl-functionalized Ir complex.

## RESULTS AND DISCUSSION

### Synthesis

Monari, Bandini, Ceroni and coworkers previously demonstrated that chiral phenoxyoxazoline auxiliary ligands functionalized with pendant phenyl rings afford highly emissive Ir complexes for which the diastereomers were separated.[30] Weak intramolecular π–π interactions were observed between cyclometalating pyridyl and pendant phenyl moieties in the $\Lambda_S$, $\Delta_R$ diastereomers (stereochemistry analogous to **1a**) by X-ray crystallography, with centroid–centroid distances of 3.65–4.31 Å. Inspired by this work, we devised the chiral auxiliary ligand **6** with a pendant pentafluorophenyl group to enhance intramolecular π–π interactions[39–41]. 2-(2,4-Difluorophenyl)pyridine (dfppy) cyclometalating ligands were selected because they afforded higher PLQYs than 2-(phenyl)pyridine (ppy) in previous work.[30] Also, when implemented alongside the $CF_3$ group on the phenoxy moiety of the auxiliary ligand, they would allow the study of intramolecular π–π interactions in a system with a higher emission energy than $Ir(ppy)_3$.[29]

The synthetic scheme for the ligand **6** and complexes **1a** and **1b** is shown in Figure 2. The racemic aminoethanol derivative **4** was synthesized via the dihydroxylation of pentafluorostyrene (**2**) followed by the Ritter rearrangement of **3**.[46] Subsequent $ZnCl_2$-catalyzed condensation with the commercial benzonitrile derivative **5** afforded racemic **6** in 41% yield. Reaction of **6** with the racemic dimeric complex $[Ir(dfppy)_2\mu\text{–}Cl]_2$ resulted in near-quantitative conversion to the diastereomers **1a** and **1b**, which are each formed as a racemic pair of enantiomers. Anhydrous diglyme was selected as solvent to avoid any nucleophilic aromatic substitution side reactions on the perfluoroaryl ring of **6**.

The diastereomers **1a** and **1b** were easily separated via column chromatography and isolated in yields of 66% and 30%, respectively. Analysis of the crude evaporated reaction mixture by $^1$H NMR (Figure 3) indicates a similar diastereomeric ratio i.e. 2:1 in favor of **1a**; as does a trace of the UV detector output from the preparative flash chromatography system used to separate **1a** and **1b** (Figure S19). $D_2$-1,1,2,2-tetrachloroethane was used as the NMR solvent in this study due its high boiling point which enabled the VT NMR study reported below. The diastereoselectivity is reproducible. Importantly, no discernible diastereoselectivity was reported for non-perfluorinated analogues,[30] indicating that perfluorination of the pendant ring on **6** is responsible for the diastereoselectivity encountered during the synthesis of **1a** and **1b**. We propose that this is due to more favorable intramolecular π–π interactions in **1a** than **1b** (see X-ray diffraction and VT NMR data below), as perfluorination is known to enhance π–π stacking[38–41] and Ar–H and Ar–F groups exert very similar steric effects.[47] Such a combination of diastereoselectivity and clean diastereomer separation is noteworthy. The separation of diastereomeric monoiridium complexes is often challenging[48] and has previously required HPLC separation.[49] Previously reported separations have often focused on statistical distributions of isomers for which no diastereoselectivity was observed.[30,50] The only completely diastereoselective synthesis of a diastereomeric monoiridium complex that we are aware of affords complexes with poor photophysical performance due to their proline auxiliary ligands (PLQY < 10%).[32]

The complexes show good thermal stability with decomposition temperatures ($T_d$ corresponding to 5% weight loss) of ca. 320 °C by thermal gravimetric analysis (TGA) (Figures S25 and S26).

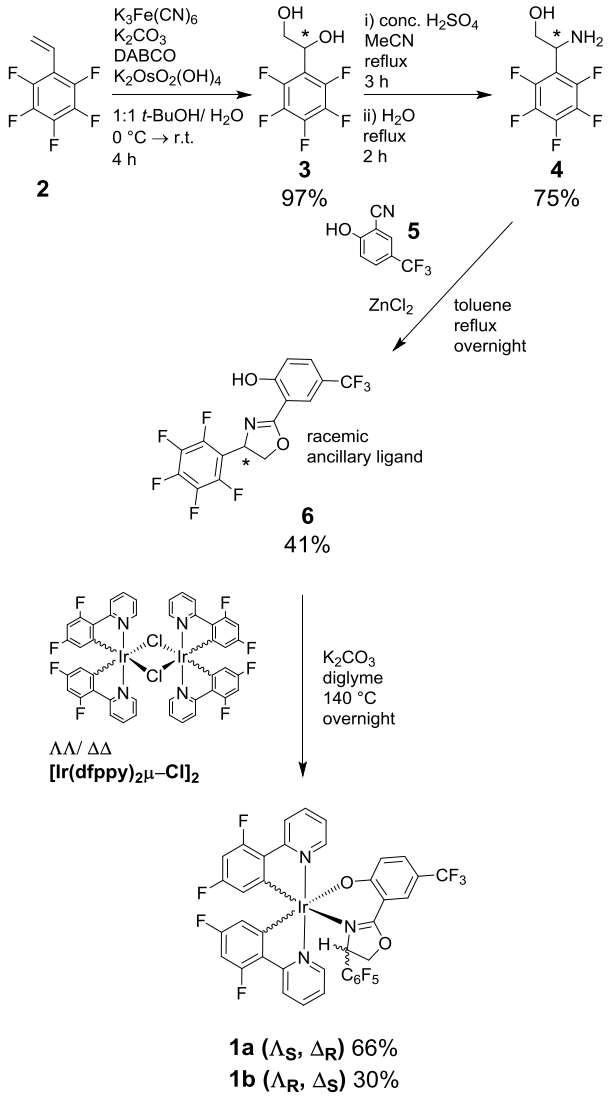


**Figure 2.** Syntheses of the chiral auxiliary ligand **6** and the diastereomeric complexes **1a** and **1b**.

### Intramolecular π–π interactions

### X-ray crystallography

The molecular structures of **1a** and **1b** were studied by single crystal X-ray diffraction. Important parameters are summarized in Table 1 and the structures are shown in Figure 4.

The crystals are racemic for both diastereomers, while the crystal of **1a** contains two crystallographically non-equivalent molecules (Figure S29). Both complexes **1a** and **1b** have distorted octahedral coordination about their Ir centers as expected, with the N atoms of the cyclometalating ligands occupying positions axial to the plane of the phenoxyoxazoline ligand coordination, and *trans* to each other. The phenoxyoxazoline ligand **6** coordinates via a 6-membered N^O chelate as expected.[28]

The structure of the $\Delta_R/\ \Lambda_S$ diastereomer **1a** features slipped face-to-face intramolecular π–π interactions (vector *D* in Figure 4) between the pendant pentafluorophenyl group (ring *A*) and the pyridyl component of a cyclometalating ligand (ring *B*) (Figure 1). This is analogous to $\Delta_R/\ \Lambda_S$ non-fluorinated analogues,[30] although the stacking in **1a** is closer (*D* = 3.30 Å vs. 3.57 Å) due to perfluorination of the pendant aryl group, as intended.

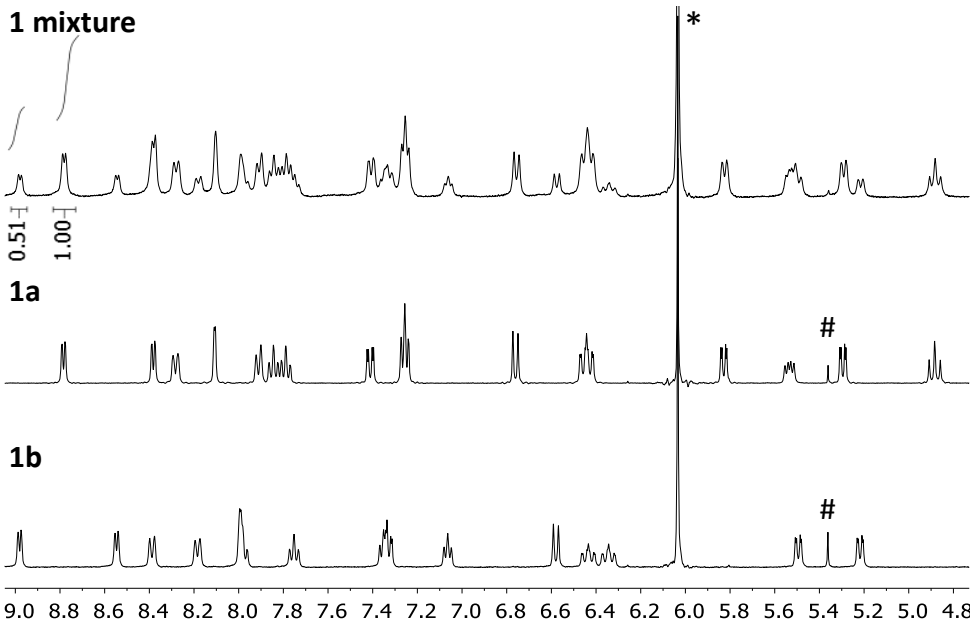


**Figure 3.** Aromatic regions of the $^1$H NMR spectra of crude **1** and the resolved diastereomers **1a** and **1b** in $D_2$-1,1,2,2-tetrachloroethane to highlight the *ca.* 2:1 diastereomeric ratio; * = residual $D_1,H_1$-1,1,2,2-tetrachloroethane in the NMR solvent; # = $CH_2Cl_2$, chemical shifts are in ppm.

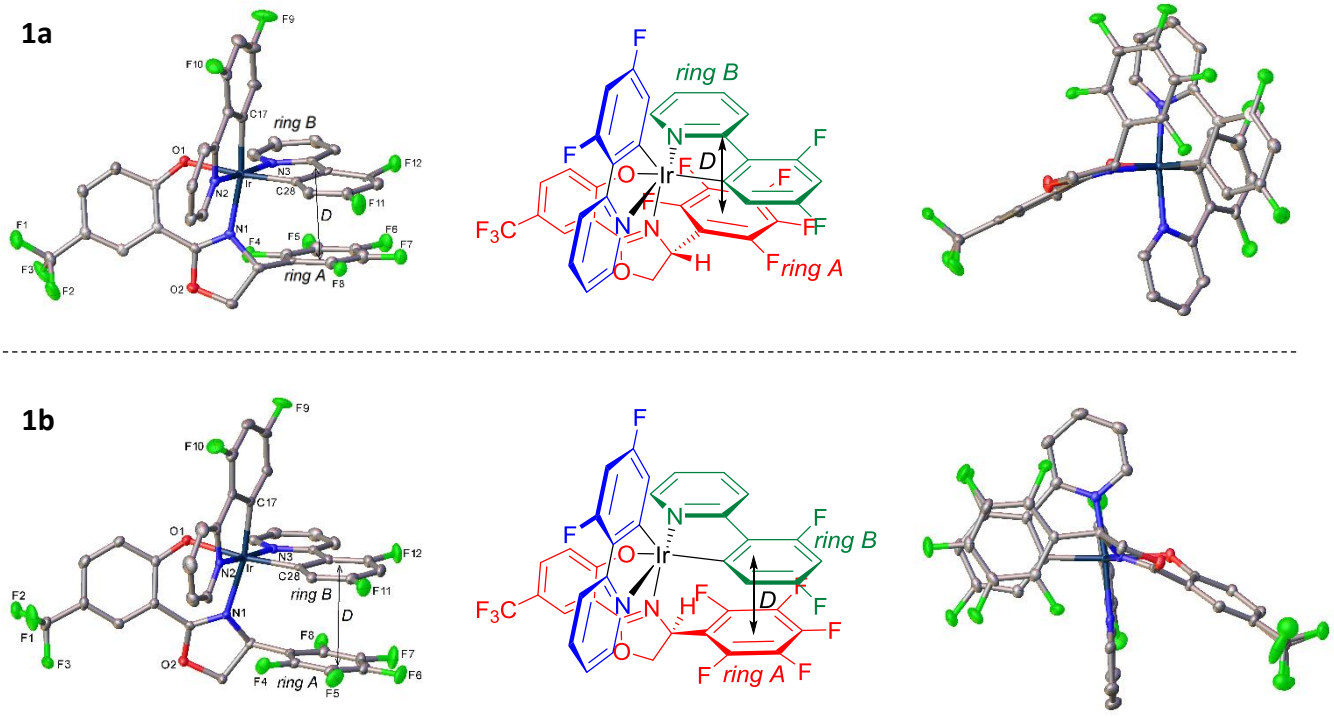

**Figure 4.** (Top) Two depictions of the X-ray crystal structure of $\Delta_R$-**1a**. The left OLEX2[51] perspective plot highlights intramolecular π–π interactions. The central structure is drawn in the same projection as this plot to clarify the differing stereochemistry of the diastereomers. The right perspective plot is projected along the auxiliary ligand Ir–N–O coordination plane. Cyclometalating ligands are drawn in green and blue while the auxiliary ligand is drawn in red. (Bottom) Similar diagrams for $\Delta_S$-**1b**. Thermal ellipsoids are drawn at the 50% probability level and H atoms are omitted for clarity. Vector *D* identifies intramolecular π–π interactions (see Table 1 and discussion in the text).

Close intramolecular stacking (*D* = 3.33 Å) is also observed for the diastereomer **1b** (Figure 4, bottom). However, unlike **1a**, it is between the pendant pentafluorophenyl group (ring *A*) and one of the cyclometalating phenyl moieties (ring *B*). The face-to-face overlap is greater (less slipped) for **1b** than for **1a**. However, the stacking in **1b** is not as close and is less parallel (**1a** Θ = 5.0/ 6.7°, *D* = 3.30 Å, **1b** Θ = 7.8°, *D* = 3.33 Å – see Table 1). The stacking in both **1a** and **1b** is facilitated by distortion of the auxiliary ligand from its coordination plane to increase the intramolecular π–π overlap. For **1a**, the plane of the phenoxy ring is bent from the auxiliary ligand's Ir–N–O coordination plane by 24.2/ 25.0°, whereas for **1b** a larger distortion of 33.8° is required to facilitate stacking. These distortions are much greater than for literature analogues that do not feature perfluoroaryl rings (5.8–15.6°).[29,30] Such notable distortions to enhance stacking in **1a** and **1b** (particularly **1b**) highlight the effectiveness of perfluorination for promoting π–π interactions.

To summarize, the intramolecular π–π stacking appears to be marginally weaker in **1b** than for **1a** while also requiring a greater structural distortion of the ancillary ligand to facilitate it. This indicates that the intramolecular π–π interactions are more favorable in **1a**, which is reinforced by the diastereoselectivity of the complex formation and the VT NMR data below.

**Table 1.** Selected geometrical parameters (bond distances in Å).

| | **1a**[a] | **1b** |
|---|---|---|
| Space group | $P2_1/n$ | $I4_1/a$ |
| Stereochemistry | $\Delta_R/\ \Lambda_S$ | $\Delta_S/\ \Lambda_R$ |
| **Bonds to cyclometalating ligands** | | |
| Ir–C (*trans*-O) | 1.99(1)/ 2.00(1) | 1.994(3) |
| Ir–C (*trans*-N) | 2.01(1)/ 2.00(1) | 1.999(3) |
| Ir–N, stacked | 2.026(9)/ 2.02(1) | 2.028(2) |
| Ir–N, non-stacked | 2.06(1)/ 2.04(1) | 2.049(2) |
| **Bonds to auxiliary ligand** | | |
| Ir–O | 2.117(8)/ 2.134(7) | 2.137(2) |
| Ir–N | 2.140(8)/ 2.14(1) | 2.165(2) |
| Deviation of phenoxy plane from Ir–N1–O1 coordination plane, ° | 25.0/ 24.2 | 33.8 |
| **Intramolecular stacking (π–π)** | | |
| Θ, °[b] | 5.0/ 6.7 | 7.8 |
| *D*, Å[c] | 3.30 | 3.33 |

[a] Contains two crystallographically non-equivalent molecules. [b] Interplanar angle between pendant pentafluorophenyl ring *A* of the ancillary ligand and ring *B* of the cyclometalating ligand (pyridine for **1a**, phenyl for **1b** - see Figure 4); [c] distance between the plane of ring *B* and the centroid of ring *A*.

**Variable temperature $^{19}$F NMR spectroscopy**

The intramolecular π–π interactions in **1a** and **1b** were also studied in solution by VT $^{19}$F NMR spectroscopy (Figure 5) to compliment the single crystal X-ray data.

At 25 °C (Figure 5, top left) both diastereomers exhibit five $^{19}$F environments between *ca.* −140 and −160 ppm of equal integration, which are assigned to the pentafluorophenyl groups. The presence of five distinct environments (in contrast to the free ligand **6** for which there are three environments – Figure S15) is ascribed to a breakdown in molecular symmetry, and indicates that the intramolecular π–π interactions in both **1a** and **1b** are strong enough to restrict rotation of the pendant pentafluorophenyl units in solution.[38] No such restriction of rotation is observed in the $^1$H NMR spectra of the non-perfluorinated analogues reported by Monari, Bandini and Ceroni, indicating that the intramolecular π–π interactions in our perfluorinated derivatives are stronger.[30]

*Meta* $^{19}$F–$^{19}$F coupling appears to be absent from the spectra, as previously reported for other heavily fluorinated aromatics.[38,52–56] Consequently, both diastereomers **1a** and **1b** display well-resolved triplets corresponding to the pentafluorophenyl 4 positions at room temperature. However, whereas the signals corresponding to the 2, 3, 4 and 5 positions are sharp for **1a**, they are broader and less well defined for **1b**. This suggests that rotation of the pentafluorophenyl group at room temperature is more restricted (i.e. exchange is slower) for **1a** and this was further investigated using VT $^{19}$F NMR spectroscopy.

Upon heating, no significant change is observed in the shape of the triplets corresponding to the 4 positions across the entire temperature range for both **1a** and **1b**. This is expected as the 4 positions are *para* to the freely rotating C–C bond.

For **1a** the signals corresponding to the 2 and 6 positions slightly broaden upon heating to 100 °C, resolving into doublets (Figure 5, bottom left). They also move towards one another, although at 100 °C they are still far from their coalescence point – their frequency difference ($\delta\nu$) is *ca.* 330 Hz at 25 °C, which decreases to *ca*. 250 Hz at 100 °C. Similarly, the signals corresponding to the 3 and 5 positions slightly broaden upon heating, while $\delta\nu$ decreases from *ca.* 550 Hz at 25 °C to *ca.* 460 Hz at 100 °C. These changes indicate that the rate at which the pendant pentafluorophenyl ring rotates increases with temperature. However, as none of the signals is close to coalescing at 100 °C, it is concluded that exchange is slow across the entire studied temperature range and a significant energetic barrier exists for rotation of the pendant pentafluorophenyl ring of **1a**.

The VT NMR data for **1b** (Figure 5, right) contrast with those obtained for **1a**, as the rate of exchange for **1b** increases more drastically with temperature. The signals corresponding to the 2 and 6 positions ($\delta\nu$ at 25 °C = *ca.* 740 Hz) and the 3 and 5 positions ($\delta\nu$ at 25 °C = *ca.* 835 Hz) coalescence at *ca.* 85 °C and *ca.* 95 °C, respectively. This is because upon heating the pentafluorophenyl ring of **1b** starts to rotate sufficiently fast that the 2 and 6 positions become indistinguishable on the NMR timescale (millisecond-scale in this case – see SI discussion). The same applies to the 3 and 5 positions. As coalescence is observed for **1b**, the free energy barrier to exchange ($\Delta G^{\ddagger}$) can be tentatively estimated at 70 kJ mol$^{-1}$ (see SI).[57] This value is comparable to the room temperature $\Delta G^{\ddagger}$ values of *ca.* 80 kJ mol$^{-1}$ reported by Cozzi and

Siegel et al. for rotation of intramolecularly-stacked perfluoroaryl rings in diarylnaphthalenes.[40,41]

Importantly, coalescence is observed for **1b**, but not **1a**. From this it is clear that intramolecular π–π interactions are more effective at restricting rotation of the pentafluorophenyl ring in **1a**. This is in agreement with the more favorable stacking observed in **1a** by X-ray diffraction above.

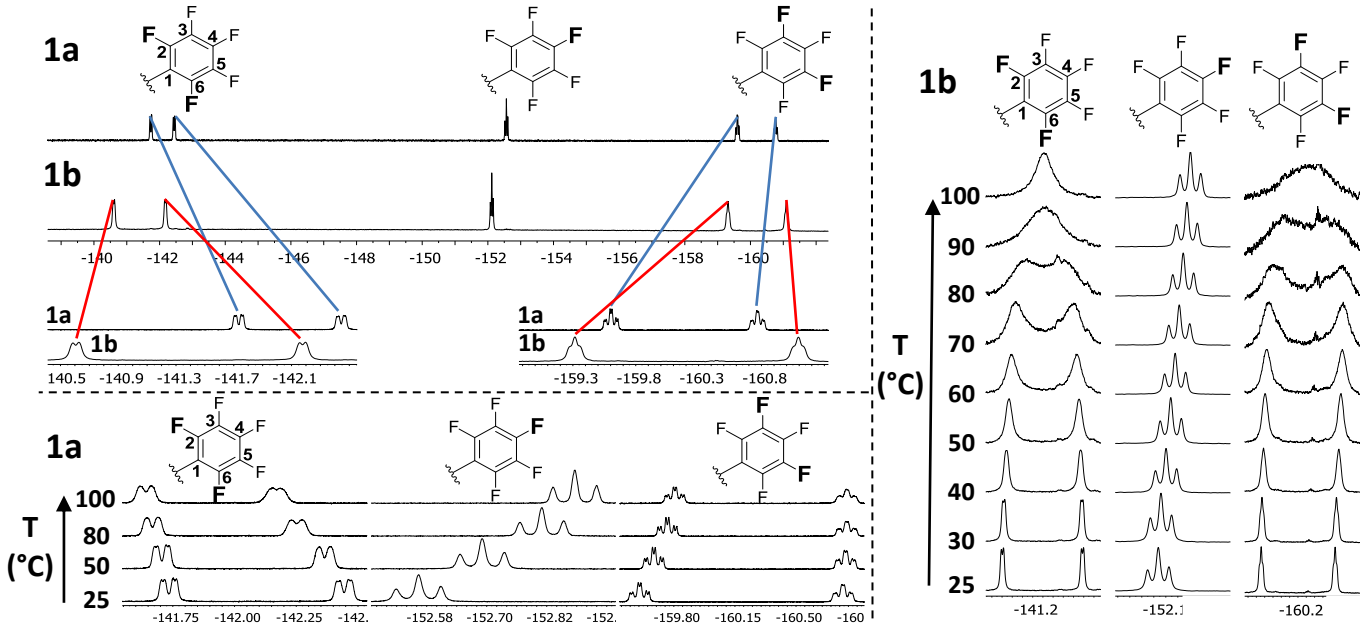


**Figure 5.** (Top left) Expansions of the pentafluorophenyl regions of the $^{19}$F NMR spectra of **1a** and **1b** at room temperature. (Bottom left) VT $^{19}$F NMR spectra for **1a** recorded between 25 and 100 °C. (Right) VT $^{19}$F NMR spectra for **1b** recorded between 25 and 100 °C. All spectra were recorded in $D_2$-1,1,2,2-tetrachloroethane; temperatures are ± 5 °C; chemical shifts are in ppm.

### Electrochemical and photophysical properties

The oxidation and reduction potentials for **1a** and **1b** were obtained via cyclic voltammetry (CV). The key data are listed in Table 2, and the voltammograms are shown in Figure S20.

**Table 2.** Electrochemical data for complexes **1a** and **1b** referenced to $E_{1/2}$ FcH/ FcH$^+$ = 0.00 V.

| Complex | $E^{ox}$/V $E_{pa}$/ $E_{pc}$ [$E_{1/2}$] | $E^{red}_{onset}$ /V[a] | HOMO /eV[b] | LUMO /eV[c] | $E_g$[d] |
|---|---|---|---|---|---|
| **1a** | 0.88/ 0.69 [0.78] | –2.37 | –5.58 | –2.43 | 3.15 |
| **1b** | 0.87/ 0.74 [0.81] | –2.35 | –5.61 | –2.45 | 3.16 |

[a]All reductions are electrochemically irreversible; [b]HOMO levels calculated from CV potentials by HOMO = –4.8 + (–$E_{1/2}^{ox}$), using ferrocene as the standard; [c]LUMO levels calculated from CV potentials by LUMO = –4.8 + (–$E^{red}_{onset}$), using ferrocene as the standard; [d]Estimated electrochemical HOMO–LUMO gap.

Both diastereomers **1a** and **1b** display electrochemically reversible oxidations. The variation between their oxidation potentials is minimal (30 mV), as expected for diastereomers.[38,58,59] The oxidations were determined to be chemically reversible over 10 cycles for both **1a** and **1b** (Figure S21).

The estimated reduction potentials for **1a** and **1b** are typical for ppy-based cyclometalated heteroleptic Ir complexes (i.e. within *ca.* 2.2–2.8 V).[60] While their irreversiblity adds error to their accurate determination, it is clear from the voltammograms that the reduction potentials of **1a** and **1b** are similar (within 20 mV), as expected. Because of their similar redox potentials, the electrochemical band gaps ($E_g$) for **1a** and **1b** are practically identical.

The absorption and emission spectra for **1a** and **1b** are shown in Figure 6 and the key data are listed in Table 3. The absorption spectra for both diastereomers are very similar and display profiles and extinction coefficients typical of cyclometalated Ir complexes.[60,61] The bands below 300 nm are ascribed to spin-allowed ligand-centered (LC) $^1$π–π* transitions, while the longer wavelength bands which extend to 490 nm are assigned to both singlet and triplet metal-to-ligand charge transfer states ($^1$MLCT and $^3$MLCT).[61]

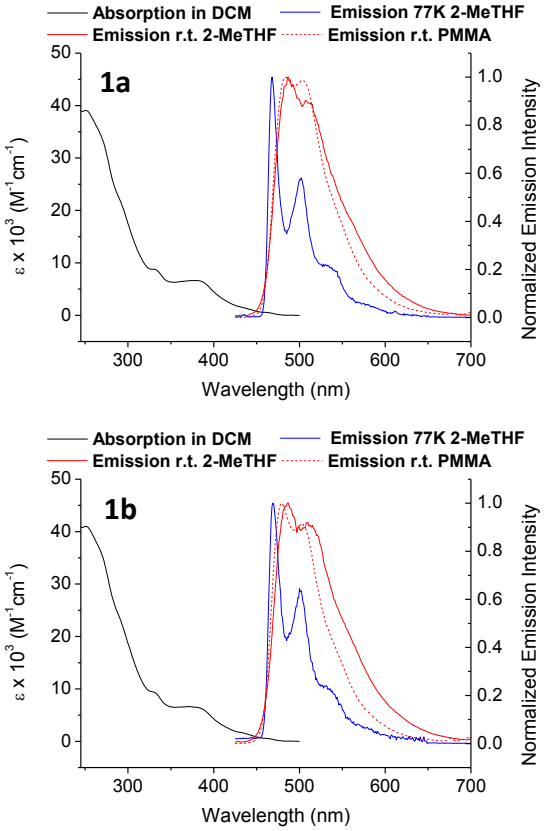


**Figure 6.** Absorption and PL spectra of **1a** and **1b**; $\lambda_{ex}$ = 355 nm.

The PL properties of **1a** and **1b** in degassed 2-MeTHF solution at 20 °C are identical within experimental error. They each display broad profiles with subtle vibronic features, indicative of emission from admixed $^3$LC/ $^3$MLCT states,[62] with full width half maxima (FWHM) of *ca.* 80 nm. The PLQYs of **1a** and **1b** are *ca.* 50% and their phosphorescence lifetimes are around 1.5 µs. These data are within the range reported for Ir(III) complexes with 2-phenoxyazole auxiliary ligands, including non-perfluorinated analogues of **1a** and **1b**, and are typical of heteroleptic phosphorescent iridium complexes.[16,26,60] **1a** and **1b** display the same 77 K emission spectra in 2-MeTHF, with estimated Huang-Rhys factors and triplet energies ($E_T$) of 0.6 (1 s.f.) and 2.70 eV, respectively. This similarity in the photophysical properties between **1a** and **1b** is important information for future work, demonstrating that diastereomeric mixtures of monoiridium complexes can be studied without concern that the diastereomers are behaving differently.

**Table 3.** Photophysical properties of complexes **1a** and **1b**.

| | **DCM solution** | | **2-MeTHF solution**[a] | | | | |
|---|---|---|---|---|---|---|---|
| **Complex** | **$\lambda_{abs}$ /nm ($\varepsilon \times 10^3$ / $M^{-1}cm^{-1}$)** | | **$\lambda_{max\ em}$ /nm [$CIE_{xy}$]** | **PLQY /% (± 5%)** | **$\tau$ /µs** | **$k_r$ /× $10^5$ $s^{-1}$** | **$k_{nr}$ /× $10^5$ $s^{-1}$** |
| **1a** | 251 (39), 270sh (33), 291sh (22), 332 (8.7), 383 (6.5), 439sh (1.3), 464 (0.5), 490 (0.1) | | 487 [0.23, 0.49] | 51 | 1.56 | 3.27 | 3.14 |
| **1b** | 252 (41), 269sh (36), 290sh (23), 332 (9.0), 384 (6.3), 438sh (1.4), 465 (0.5), 490 (0.1) | | 487 [0.24, 0.49] | 50 | 1.54 | 3.25 | 3.25 |
| | **2-MeTHF glass**[b] | | **Doped into PMMA 1% wt.**[c] | | | | |
| **Complex** | **$\lambda_{max\ em}$ /nm ($\lambda_{10\%\ em}$ /nm)**[d] **[$E_T$ /eV]**[e] | **$\tau$ /µs** | **$\lambda_{max\ em}$ /nm [$CIE_{xy}$]** | **PLQY /% (± 10%)** | **$\tau$ /µs** | **$k_r$ /× $10^5$ $s^{-1}$** | **$k_{nr}$ /× $10^5$ $s^{-1}$** |
| **1a** | 468 (459) [2.70] | 2.79 | 485 [0.18, 0.46] | 67 | 1.72 | 3.90 | 1.92 |
| **1b** | 469 (459) [2.70] | 2.49 | 479 [0.17, 0.42] | 60 | 1.73 | 3.47 | 2.31 |

sh = Shoulder. [a]Solution photoluminescence measurements were recorded in degassed 2-MeTHF solutions at *ca.* 20 °C with an excitation wavelength of 355 nm with quinine sulfate in 0.5 M $H_2SO_4$ as standard ($\Phi$ = 0.546);[16] under the same experimental conditions a value of 73 ± 5% was obtained for FIrpic; [b]Measured at 77 K using an excitation wavelength of 355 nm; [c]Measured in an integrating sphere under air using an excitation wavelength of 355 nm; [d]Wavelength at 10% intensity on the blue edge of the spectrum obtained at 77 K; [e]Estimated using $E_T = hc/\lambda_{10\%\ em}$. $\tau = 1/k_{nr} + k_r$.

When doped into poly(methyl methacrylate) (PMMA) both **1a** and **1b** feature longer $\tau$ values of *ca.* 1.7 µs. The PLQYs are slightly increased to 60/ 67 ± 10%, although within experimental error they are similar to the solution values. This can mainly be attributed to decreases in $k_{nr}$, due to the more rigid PMMA matrix, although there is also a small increase in the radiative rate constant ($k_r$) for both complexes. Despite very similar lifetimes and PLQYs in PMMA, a noteworthy difference is observed between the spectral profiles of **1a** and **1b**. Doping either complex into PMMA leads to PL spectra that are blue-shifted (by 2 nm for **1a** and 8 nm for **1b**) and narrower (FWHM **1a** = *ca.* 70 nm, **1b** = 65 nm) than in 2-MeTHF solution. These effects are more pro-

nounced for **1b**, and may be related either to the higher rigidity of PMMA in comparison to 2-MeTHF, or its polarity.

While **1a** and **1b** display similar PL properties at room temperature and 77 K, the VT NMR data above suggest that they may display different photophysical properties at elevated temperatures, prompting a high temperature PL study. The PL spectra of **1a** and **1b** in xylenes upon cycling the temperature between 30 and 100 °C are shown in Figure 7.

Upon heating from 30→100 °C the emission intensities for both complexes decrease. The decrease in intensity is not due to decomposition or ingress of oxygen as the initial spectral intensities are retained upon cooling back to 30 °C. The normalized spectral profiles do not change for either diastereomer (shown for **1b** in Figure S22), suggesting that PL originates from the same state at both temperatures. A decrease in the emission intensities of **1a** and **1b** upon heating implies the existence of a temperature dependent non-radiative pathway which becomes more accessible at higher temperatures. For cyclometalated iridium complexes this has been ascribed to the thermal population of low-lying metal centered (MC) states.[62,63]

The integrated emission intensity for **1a** drops to 44% of its initial intensity upon heating to 100 °C, whereas it drops to 18% for **1b**. Both complexes have the same solution PL $\lambda_{max}$, PLQY and phosphorescence lifetime, display identical $E_T$ and have the same coordination environment about their Ir centers. Therefore, the energy gaps between the MC and emitting states for **1a** and **1b** are expected to be very similar, meaning that non-radiative deactivation via thermally accessible MC states alone cannot explain such a significant difference in the temperature dependence of their PL properties. The VT $^{19}$F NMR data above indicate that there is a smaller energy barrier to rotation of the $C_6F_5$ ring in **1b**. Therefore, such rotation can be expected to constitute a more easily populated non-radiative pathway for **1b** than **1a**, which leads to a more substantial decrease in emission intensity upon heating for **1b** and explains the observed differences in the high temperature PL data.

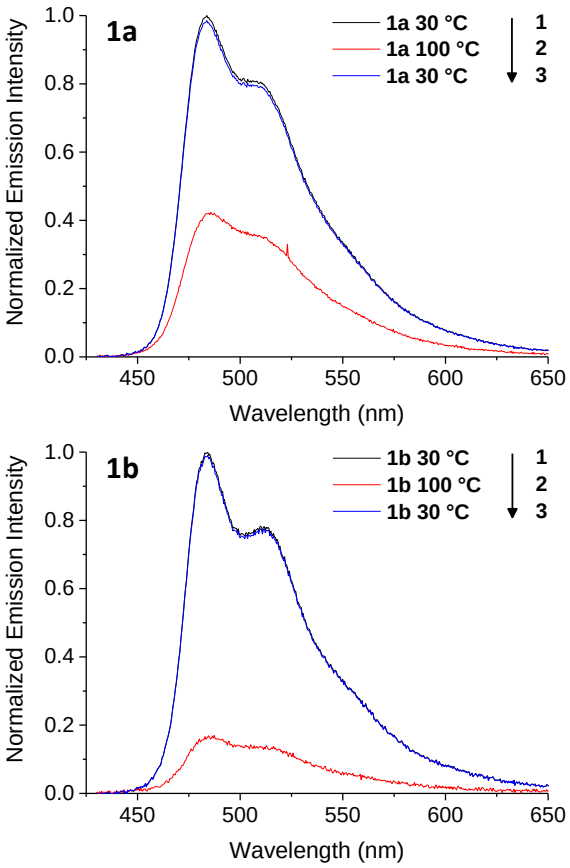


**Figure 7.** Variable temperature PL spectra of **1a** and **1b** recorded in degassed xylenes. The spectra are normalized to the initial emission intensity at 30 °C. Temperatures are ± 5 °C; $\lambda_{ex}$ = 405 nm. The numbers refer to the order in which the spectra were run.

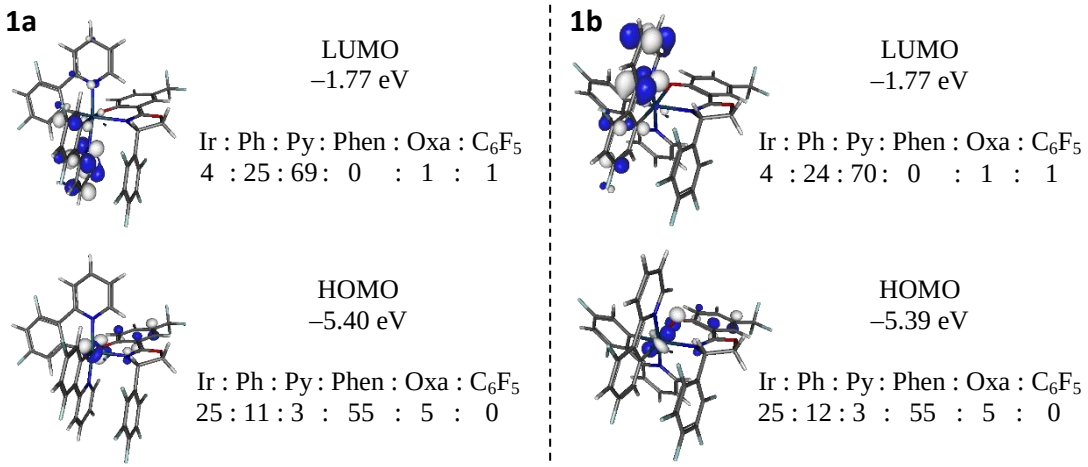


**Figure 8.** Molecular orbital compositions for **1a** and **1b**. Contributions are percentages. Ph = phenyl, Py = pyridyl, Phen = phenoxy, Oxa = oxazoline.

## Computational study

Electronic structure calculations were carried out on **1a** and **1b** to explore their molecular orbitals and to support their electrochemical and photophysical properties. The optimized $S_0$ geometries were calculated at the B3LYP/LANL2DZ:6–31G* level. They are in good agreement with the X-ray crystallographic data above - intramolecular π–π interactions are observed for both diastereomers and the auxiliary ligand of **1b** is more distorted. Complex **1a** is less stable than **1b** by 2.3 kJ mol$^{-1}$, suggesting that **1a** is the kinetic product, although it could not be isomerized to **1b** photochemically.

Molecular orbital plots for the highest occupied molecular orbitals (HOMO) and lowest unoccupied molecular orbitals (LUMO) of **1a** and **1b** are shown in Figure 8. Further plots and tabulated contributions for the HOMO−1 – LUMO+2 orbitals are given in Figure S23 and Table S1.

The HOMO−1 – LUMO+2 compositions are near-identical for both complexes. The HOMOs are primarily localized on the phenoxy moieties of the auxiliary ligands (55%) and the Ir atoms (25%), with small contributions from the cyclometalating phenyl groups (*ca.* 10%). This suggests that the $CF_3$ and oxazoline-functionalized phenoxy moiety is more electron rich than a cyclometalated dfppy ring. The LUMOs are almost exclusively localized on the cyclometallating ligands with *ca.* 70% and 25% contributions from the pyridyl and phenyl moieties, respectively. Therefore, the FMO contributions for **1a** and **1b** are in good agreement with previous complexes that feature a phenoxyoxazole auxiliary ligand.[29] It should be noted that there is no LUMO contribution from the pendant pentafluorophenyl groups for either **1a** or **1b**.

Time dependent density functional theory (TD-DFT) was also employed to simulate the absorption spectra of **1a** and **1b** and to investigate the character of their lowest energy excited states (Figure S24, Table S2). The simulated absorption spectra for both complexes broadly agree with the experimental data, while the predicted lowest energy triplet states of both **1a** and **1b** are mainly localized as expected from analysis of their frontier molecular orbitals (HOMO and LUMO) (a more detailed discussion is included in the SI). Both DFT and TD-DFT data suggest that any contributions from the pentafluorophenyl groups to the excited states of **1a** and **1b** are small, rendering them ancillary.

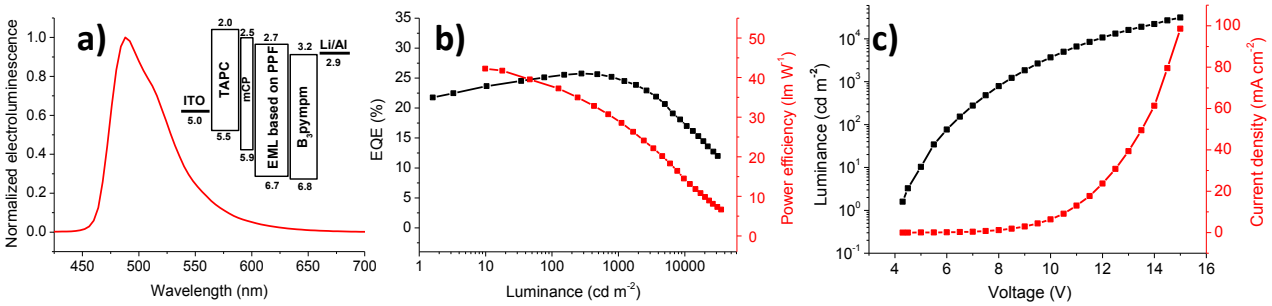


**Figure 9.** PhOLED data (8 wt%) for **1a**. a) EL spectrum at a luminance of 100 cd m$^{-2}$ (inset) Energy level diagram for the device (eV). b) External quantum efficiency and power efficiency curves vs. voltage. c) Luminance and current density curves vs. voltage.

**Table 4.** Device data for **1a**.

| wt% | $V_{on}$ [V][a] | $L_{max}$ /cd $m^{-2}$ | EQE /%[b] | PE /lm $W^{-1}$ [b] | $CIE_{xy}$[c] |
|---|---|---|---|---|---|
| 3.5 | 4.7 | 9190 | 23.6, 23.5, 19.1 | 34.0, 28.5, 15.3 | 0.17, 0.46 |
| 8 | 4.3 | 31480 | 25.8, 25.3, 24.9 | 42.3, 33.6, 24.8 | 0.17, 0.48 |
| 15 | 4.0 | 21870 | 24.3, 23.7, 23.1 | 41.9, 31.2, 22.0 | 0.18, 0.50 |

$L_{max}$ = maximum luminance. [a]Applied voltage required to reach a luminance of 1 cd $m^{-2}$; [b]The efficiencies listed are the maximum values and the values at 100 and 1000 cd $m^{-2}$, respectively; [c]Recorded at 1000 cd $m^{-2}$.

### PhOLEDs

To evaluate the major diastereomer **1a** as an emitter in PhOLEDs, devices were fabricated in the following configuration: ITO/ TAPC (30 nm)/ mCP (10 nm)/ PPF: **1a** (30 nm)/ $B_3$pympm (30 nm)/ LiF/ Al. The devices were fabricated by thermal evaporation onto a cleaned glass substrate precoated with conductive transparent indium tin oxide (ITO), where 4,4′-cyclohexylidenebis[*N*,*N*-bis(4-methylphenyl)benzenamine] (TAPC) served as hole-transporting layer, 1,3-bis-(carbazol-9-yl)benzene (mCP) as an electron/exciton-blocking layer (EBL) between TAPC and the emissive layer, 4,6-bis(3,5-di(pyridin-3-yl)phenyl)-2-methylpyrimidine ($B_3$pympm) as an electron-transporting layer and 2,8-bis(diphenylphosphoryl)dibenzofuran (PPF) is the host. Devices were fabricated with doping levels of **1a** of 3.5, 8 and 15 wt%. The device data are summarized in Table 4. Data are plotted for the best performing device (8 wt%) in Figure 9; the comparable data for the 3.5 and 15 wt% devices are presented in Figures S27 and S28. Generally, the most commonly used and suitable concentration of an Ir complex for doping PhOLEDs is 5-10 wt%.[6-12] Indeed our results in this manuscript confirmed this, as the devices employing 8 wt% showed the highest performance. Here, other devices adopting lower (3.5 wt%) and higher (15 wt%) concentrations of **1a** were also fabricated to investigate the dependence of the doping concentration on the EL performance, as discussed below.

The electroluminescence (EL) spectrum of the 8 wt% device at 100 cd $m^{-2}$ is consistent with the PL spectrum recorded for **1a** in PMMA, although the EL spectrum is narrower (by 15 nm). The device displays a turn on voltage of 4.3 V. It also features a high maximum external quantum efficiency ($EQE_{max}$) of 25.8% (at *ca.* 270 cd $m^{-2}$) with a low efficiency roll-off to 24.9% at 1000 cd $m^{-2}$, which is better than previously reported data for other heteroleptic complexes functionalized with phenoxyoxazole/ thiazole auxiliary ligands.[28,29] However, the maximum brightness and luminance efficiency are lower than compared to the previous derivatives. The overall EL performance for the 3.5 wt% device is poorer than for the 8 wt% devices (Table 4). This is presumably because of the low content of the dopant molecules, which means that almost all holes and/or electrons must inject into the emissive layer from the host molecules. For this to occur, the large energy barriers between the charge transport layers and emissive layer due to the rather wide HOMO−LUMO gap of the host must be overcome, resulting in a high buildup of charge carriers at the corresponding interfaces. The decreased performance of the 15 wt% device is likely due to an increased probability of triplet-triplet annihilation.

Notably, the maximum EQE, power efficiency (PE) and luminance efficiency ($L_{max}$) values for 8 wt% **1a** are either notably better than, or highly competitive with those obtained by Shan, Xie and Su et al. for a device doped with a different pentafluorophenyl-functionalized heteroleptic Ir complex (max EQE = 10.7%, max PE = 27.6 lm $W^{-1}$, $L_{max}$ = 32710 cd $m^{-2}$ ).[64] At 10,000 cd $m^{-2}$ an EQE of > 15% is maintained for the device doped with 8 wt% **1a**, compared with *ca.* 10% reported by Shan, Xie and Su et al at this brightness. These new data provide a further example for which multi-fluorination of an Ir(III) phosphor does not mandate poor PhOLED performance. This is in contrast to what would be expected considering that only four aromatic fluorine atoms are known to adversely effect the PhOLED performance of FIrpic, and **1a** incorporates and additional five Ar–F groups (nine in total).[65–67] This is likely related to the ancillary nature of the additional aromatic fluorine atoms on the pentafluorophenyl substituent in **1a**, which is also the case for the example presented by Shan, Xie and Su and coworkers.[64] Literature precedent from work on emitters for light emitting electrochemical cells suggests that the intramolecular π–π interactions in **1a** may also play a significant role in the good device performance.[33]

## Conclusions

In conclusion, the new diastereomeric Ir complexes **1a** and **1b** were obtained in a 2:1 ratio. They were easily separated and their structural, electrochemical and photophysical properties were studied in detail.

In both diastereomers the pendant pentafluorophenyl ring on the chiral auxiliary ligand engages in close (D = *ca.* 3.3 Å) intramolecular π–π stacking with a cyclometalating ligand on the periphery of the complexes. The intramolecular π–π stacking was studied in the solid state by single crystal X-ray diffraction and in solution by VT $^{19}$F NMR. The interactions are stronger in **1a**, leading to the observed diastereoselectivity. The different intramolecular π–π interactions in **1a** and **1b** have little influence on their photophysical properties at room temperature. This is likely because the interactions occur on the periphery of an already highly emissive Ir complex core. However, upon heating to high temperatures the weaker intramolecular π–π interactions in **1b** provide a more efficient thermally activated pathway to quench phosphorescence through rotation of the pentafluorophenyl ring. Overall the photophysical differences between **1a** and **1b** are small. Nevertheless, the separation and study of diastereomeric Ir(III) phosphors in detail is still relatively rare, and further enhances the understanding of the effects of stereochemistry on the photophysical properties of Ir(III) complexes.

This study also enriches the literature on phosphorescent Ir complexes, especially related to the effects of intramolecular π–π interactions and ancillary aromatic fluorine atoms on structural and photophysical properties. This is evident from PhOLED results: A vacuum-processed PhOLED doped with **1a** as the emissive dopant gave a high $EQE_{max}$ and low efficiency roll-off (EQE 24.9% at 1000 cd $m^{-2}$) for a complex with such a highly fluorinated aryl substituent. This is likely related to the ancillary nature of the pentafluorophenyl group, which is predicted by DFT/ TD-DFT for both **1a** and **1b**. Future work should address the significance of ancillary fluorine atoms on the stability of Ir complexes, as this may provide new insights into designing highly fluorinated Ir(III) complexes that improve upon complexes such as FIrpic, for which the non-ancillary fluorine atoms are known to be a source of instability.[65,68]

# EXPERIMENTAL SECTION

## General

$^1$H, $^{13}$C and $^{19}$F NMR spectra were recorded on Bruker Avance 400 MHz, Varian Mercury 400 MHz, Varian Inova 500 MHz or Varian VNMRS 600 MHz spectrometers. All spectra were referenced against the residual solvent signal and peak shifts are reported in ppm. Electrospray ionization (ESI) mass spectra were

recorded on a Waters Ltd. TQD spectrometer. Elemental analyses were obtained on an Exeter Analytical Inc. CE-440 elemental analyser. Thermal analysis was run under a helium atmosphere at a rate of 10 °C $min^{-1}$ using a Perkin-Elmer Pyris 1 instrument. Melting points were determined in open ended capillaries using a Stuart Scientific SMP3 melting point apparatus at a ramp rate of 3 °C $min^{-1}$ and are uncorrected. Reactions requiring an inert atmosphere were carried out under argon which was first passed through a phosphorus pentoxide column. For reaction monitoring analytical thin layer chromatography (TLC) was carried out on silica gel (Merck, silica gel 60, F254) or alumina (Merck, neutral alumina 60 type E, F254) plates and visualized using UV light (254, 315, 365 nm). GCMS data were recorded on a Thermo-Finnigan Trace GCMS. Flash chromatography was carried out using either glass columns or a Biotage® Isolera One™ automated flash chromatography machine on 60 micron silica gel purchased from Fluorochem Ltd. All commercial chemicals were of ≥ 95% purity and were used as received without further purification. All solvents used were of analytical reagent grade or higher. Anhydrous solvents were dried through a HPLC column on an Innovative Technology Inc. solvent purification system or obtained commercially.

## Calculations

All calculations were carried out with the Gaussian 09 package.[69] All optimized $S_0$ geometries of the iridium complexes were carried out using B3LYP[70,71] with the pseudopotential (LANL2DZ)[72–74] for iridium and 6–31G* basis set for all other atoms.[75,76]All $S_0$ geometries were true minima based on no imaginary frequencies found. Electronic structure calculations were also carried out on the optimized geometries at B3LYP/LANL2DZ:6–31G*. The MO diagrams and orbital contributions were generated with the aid of Gabedit[77] and GaussSum[78] packages, respectively.

## X-ray crystallography

X-ray diffraction experiments were carried out on a Bruker 3-circle D8 Venture diffractometer with a PHOTON 100 CMOS area detector, using Mo-*K*α radiation from an Incoatec IμS microsource with focussing mirrors (λ=0.71073 Å) and a Cryostream open-flow $N_2$ gas cryostat. The structures were solved by direct methods (SHELXS[79]) and refined by full-matrix least squares using SHELXL[80] programs on OLEX2 platform.[51]
*Crystal data*: **1a**, $C_{38}H_{18}F_{12}IrN_3O_2$, *M*=968.75, monoclinic, space group $P2_1/n$ (#14), *a*=11.2459(6), *b*=15.8876(9), *c*=36.256(2) Å, β=96.748(1)°, *V*=6433.0(6) $Å^3$, *Z*=8, $D_x$=2.000 g $cm^{-3}$, μ=4.26 $mm^{-1}$, T=120 K, 78522 data with 2θ≤50.7° (11783 unique, $R_{int}$=0.085), $R_1$=0.071 on 8751 data with $I>2\sigma(I)$, $wR_2$=0.150 on all data, CCDC-1850087. **1b**: tetragonal, space group $I4_1/a$ (#88), *a*=19.2978(8), *c*=34.5207(15) Å, *V*=12855.7(12) $Å^3$, *Z*=16, $D_x$=2.002 g $cm^{-3}$, μ=4.27 $mm^{-1}$, T=120 K, 110471 data with 2θ≤58° (8529 unique, $R_{int}$=0.070), $R_1$=0.025 on 6701 data with $I>2\sigma(I)$, $wR_2$=0.049 on all data, CCDC-1850088.

## Electrochemistry

Cyclic voltammetry data were recorded using a BAS CV50W electrochemical analyzer fitted with a three-electrode system consisting of a glassy carbon disk (Ø = 1.8 mm) as the working electrode, a Pt wire as an auxiliary electrode and a Pt wire as a quasireference electrode. Experiments were conducted in dry THF solution with *n*-$Bu_4NPF_6$ (0.1 M) as the supporting electrolyte at a scan rate of 100 mV $s^{-1}$. All potentials were referenced internally to ferrocene.

## Photophysics

The absorption spectra were measured on either a Unicam UV2-100 spectrometer operated with the Unicam Vision software or a Thermo Scientific Evolution 220 spectrometer with the Thermo Scientific Insight software in quartz cuvettes with a path length of 10 mm. The pure solvent (DCM) was used for the baseline correction. The extinction coefficients were calculated using the Beer-Lambert Law, A = εcl. They were measured using a titration method, whereby a stock solution of known concentration was incrementally added using a calibrated glass pipette to a cuvette of pure solvent. A minimum of 1 mg of sample was weighed out for the stock solutions, and the measurements were carried out in triplicate to minimise weighing and dilution-error. photoluminescence spectra were recorded on a Horiba Jobin Yvon SPEX Fluorolog 3-22 spectrofluorometer in quartz cuvettes with a path length of 10 mm. All solutions were degassed via multiple freeze-pump-thaw cycles using a turbomolecular pump before acquisition of any spectra. For quantum yield measurements the absorption values for the samples were determined on a Unicam UV2-100 spectrometer operated with the Unicam Vision software in quartz cuvettes with a path length of 20 mm. The PLQYs of all samples were determined in triplicate by the comparative method relative to a literature standard following the literature procedure.[81] PMMA films were prepared according to a literature procedure.[38] The quantum yields of complexes doped into PMMA were recorded on a Horiba Jobin Yvon SPEX Fluorolog 3 using a calibrated Quanta-Φ integrating sphere and were calculated according to the literature method.[81] Solid state PLQY data were obtained in triplicate from three samples that were prepared in parallel: the calculated standard error values were ≤10%. Lifetime measurements were recorded using an $N_2$ laser (337 nm, 10 μJ, 10 Hz) as an excitation source in a custom spectrometer which produced a 1 kHz train of pulses of 20 ns duration. The luminescence was collected at 90° and focused onto the entrance slit of a monochromator (Bethan TM 300V). The emission was detected by a photon counting PMT and the arrival times of photons at the detector determined using a multichannel scaler. The data were transferred to a PC and analyzed using non-linear regression. The decay data were fitted to exponential functions. Low temperature emission spectra and lifetime data were measured in a DN1704 optical cryostat (Oxford Instruments) with an ITC601 temperature controller (Oxford Instruments). For high temperature PL measurements, samples were degassed via multiple freeze-pump-thaw cycles in an NMR tube fitted with a Young's tap. The sample was heated in a silicone oil bath. A 405 nm laser was focussed on the sample perpendicular to the detector of an Ocean Optics Maya Pro spectrometer.

### PhOLED fabrication and measurements

Prior to the fabrication of the devices, patterned indium tin oxide (ITO)-coated glass substrates (20 Ω/square) were first cleaned in detergent solutions, followed by de-ionized water, acetone, and isopropanol ultrasonic baths. Then, the ITO substrates were treated using a Plasma Cleaner (PDC-32G-2, 100 W) with the oxygen ambient for 5 min to increase the work function. The OLEDs were fabricated by thermal evaporation at the pressure of *ca.* 3.5 x $10^{-4}$ Pa. All organic materials were purified by sublimation and were continuously deposited onto the substrate at the rate of 0.3 Å $s^{-1}$, then a very thin layer of LiF (0.5 nm) was deposited at the rate of 0.2 Å $s^{-1}$ and the Al electrode (cathode) was deposited at the rate of 3.0~4.0 Å $s^{-1}$, where the active area of the diode segments was 2 × 2.5 $mm^2$. The EL spectra and CIE coordinates of the devices were measured using a PR650 spectrometer. The current density-voltage-luminance curves of the devices were measured using a Keithley 2400 source meter. EQEs were calculated from the *J*–*V*–*L* characteristics and EL spectra. All characterizations were carried out under ambient conditions at room temperature.

## Synthesis

Compounds **3** and **4**[46] and $[Ir(dfppy)_2\mu–Cl]_2$[82] were synthesized according to literature procedures.

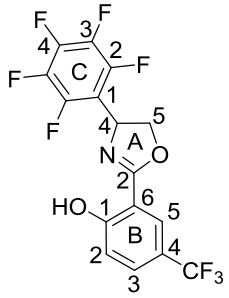


**_rac_-4-(Pentafluorophenyl)-2-(2-hydroxy-5-trifluoromethylphenyl)oxazoline (6).** *rac*-2-Amino-2-

(pentafluorophenyl)ethanol (**4**) (1.21 g, 5.33 mmol, 1.21 eq.) and 2-hydroxy-5-trifluoromethylbenzonitrile (**5**) (829 mg, 4.40 mmol, 1.00 eq.) were combined in dry toluene (12 mL). A solution of $ZnCl_2$ in THF was added (0.7 M, 0.31 mL, 0.22 mmol, 5 mol%) and the resulting mixture was heated to reflux for 20 h. The reaction mixture was cooled to room temperature and evaporated under reduced pressure. The residue was purified by flash chromatography on silica gel (eluent: gradient 1:0–1:3 *n*-hexane/ DCM with *ca*. 0.5% $NEt_3$ as additive) to afford *rac*-4-(pentafluorophenyl)-2-(2-hydroxy-5-trifluoromethylphenyl)oxazoline (**7**) as a white powder (730 mg, 1.80 mmol, 41%). M.pt. 117–119 °C; $^1$H NMR (700 MHz, $CDCl_3$) δ (ppm) = 11.91 (s, $1H_{OH}$), 8.02 (d, *J* = 2.3 Hz, $1H_{B5}$), 7.64 (dd, *J* = 8.8, 2.3 Hz, $1H_{B3}$), 7.09 (d, *J* = 8.8 Hz, $1H_{B2}$), 5.83 (dd, *J* = 10.7, 7.6 Hz, $1H_{A4}$), 4.81 (dd, *J* = 10.7, 8.8 Hz, $1H_{A5}$), 4.51 (dd, *J* = 8.2, 7.6 Hz, $1H_{A5}$); $^{13}$C NMR (101 MHz, $CDCl_3$) δ (ppm) = 166.5 ($C_{A2}$), 161.3 ($C_{B1}$), 146.0 – 136.0 ($C_{ring\ C}$), 130.7 ($C_{B3}$), 126.2 ($C_{B5}$), 123.9 (q, *J* = 270 Hz, $C_{CF3}$), 121.4 (q, *J* = 32.3 Hz, $C_{B4}$), 117.6 ($C_{B2}$), 109.9 ($C_{B6}$), 71.2 ($C_{A5}$), 58.93 ($C_{A4}$); $^{19}$F{$^1$H} NMR (376 MHz, $CDCl_3$) δ (ppm) = -61.7 (d, *J* = 1.1 Hz, $3F_{CF3}$), -143.3 – -143.5 (m, $2F_{C2}$), -153.1 (ddt, *J* = 23.1, 21.0, 2.2 Hz, $1F_{C4}$), -160.9 – -161.1 (m, $2F_{C3}$); HRMS (ESI): *m/z* 398.0459 [$MH^+$]. Calcd. for $C_{16}H_8F_8NO_2^+$: 398.0422. Due to extensive coupling to $^{19}$F nuclei, the $^{13}$C signals for ring C are stated as a range.

**Complexes 1a** and **1b.** $[Ir(dfppy)_2\mu\text{–}Cl]_2$ (315 mg, 0.26 mmol, 1.00 eq.), *rac*-4-(pentafluorophenyl)-2-(2-hydroxy-5-trifluoromethylphenyl)oxazoline (**6**) (211 mg, 0.53 mmol, 2.05 eq.) and $K_2CO_3$ (90 mg, 0.65 mmol, 2.50 eq.) were combined in dry diglyme (10 mL) under argon and heated in a 140 °C heating mantle overnight under argon. The reaction mixture was cooled to room temperature and the solvent evaporated under reduced pressure. Repeated co-evaporation with toluene to remove final traces of diglyme was beneficial for obtaining facile separation of **1a** and **1b**. The residue was purified by flash chromatography on silica gel (eluent: gradient 1:9–4:6 DCM sat. $K_2CO_3$/ *n*-hexane v/v) to elute **1a**. Increasing the solvent polarity to 6:4 DCM sat. $K_2CO_3$/ *n*-hexane v/v eluted **1b**. Each diastereomer was further purified through dissolving it in minimal DCM (*ca*. 10 mL), adding *n*-hexane (30 mL), and reducing the solvent volume to *ca.* 15 mL to induce precipitation. After cooling in a freezer for *ca.* 1 h the precipitates were isolated via filtration and washed with ice cold pentane before being dried under high vacuum.

**1a.** Isolated as a yellow microcrystalline powder (331 mg, 0.34 mmol, 66%). $^1$H NMR (600 MHz, $d_2$-1,1,2,2-TCE) δ (ppm) = 8.76 (dt, *J* = 5.5, 1.3 Hz, $1H_{A6}$), 8.36 (dt, *J* = 5.5, 1.6 Hz, $1H_{B6}$), 8.26 (d, *J* = 8.5 Hz, $1H_{B3}$), 8.08 (dd, *J* = 2.7, 1.0 Hz, $1H_{F5}$), 7.89 (d, *J* = 8.4 Hz, $1H_{A3}$), 7.82 (td, *J* = 8.5, 1.6 Hz, $1H_{B4}$), 7.76 (ddd, *J* = 8.4, 7.6, 1.3 Hz, $1H_{A4}$), 7.39 (dd, *J* = 9.2, 2.7 Hz, $1H_{F3}$), 7.25 – 7.21 (m, $2H_{A5,\ B5}$), 6.74 (d, *J* = 9.2 Hz, $1H_{F2}$), 6.45 – 6.39 (m, $2H_{C4,\ D4}$), 5.80 (dd, *J* = 8.6, 2.3 Hz, $1H_{C6}$), 5.51 (dd, *J* = 10.5, 5.7 Hz, $1H_{E4}$), 5.27 (dd, *J* = 8.8, 2.4 Hz, $1H_{D6}$), 4.86 (dd, *J* = 10.5, 9.4 Hz, $1H_{E5}$), 4.29 (dd, *J* = 9.4, 5.7 Hz, $1H_{E5}$); $^{19}$F{$^1$H} NMR (376 MHz, $d_2$-1,1,2,2-TCE) δ (ppm) = -60.34 (s, $3F_{CF3}$), -107.03 (d, *J* = 10.5 Hz, $1F_{dfppy}$), -107.63 (d, *J* = 9.9 Hz, $1F_{dfppy}$), -109.80 (d, *J* = 10.0 Hz, $1F_{dfppy}$), -110.36 (dd, *J* = 10.5, 2.8 Hz, $1F_{dfppy}$), -141.73 (dd, *J* = 22.6, 7.5 Hz, $1F_{G2/\ G6}$), -142.44 (dd, *J* = 22.2, 7.7 Hz, $1F_{G2/\ G6}$), -152.55 (t, *J* = 21.0 Hz, $1F_{G4}$), -159.59 (td, *J* = 21.0, 7.5 Hz, $1F_{G3/\ G5}$), -160.76 (td, *J* = 21.0, 7.5 Hz, $1F_{G3/\ G5}$); $^{13}$C NMR (151 MHz, $d_2$-1,1,2,2-TCE) δ (ppm) = 171.4 ($C_{F1}$), 165.5 (d, *J* = 9 Hz, $C_{B2}$), 164.4 (d, *J* = 263 Hz, $C_{D5}$), 165.0 – 160.0 ($C_{Ring\ G}$), 164.2 (d, J = 258 Hz, $C_{C5}$), 164.1 (d, *J* = 7 Hz, $C_{A2}$), 163.82 ($C_{F6}$), 161.6 (t, *J* = 273 Hz, $C_{C3}$), 161.6 (t, *J* = 273 Hz, $C_{D3}$), 155.5 (d, *J* = 6.0 Hz, $C_{D1}$), 150.5 (d, *J* = 7.1 Hz, $C_{C1}$), 148.7 ($C_{A6}$), 147.56 ($C_{B6}$), 138.30 ($C_{B5}$), 137.9 ($C_{A4}$), 130.1 ($C_{F3}$), 128.8 ($C_{F5}$), 128.4 ($C_{D2}$), 128.3 ($C_{C2}$), 125.8 ($C_{F2}$), 123.4 (d, *J* = 20.4 Hz, $C_{B3}$), 122.6 ($C_{B5}$), 122.2 ($C_{A5}$), 121.9 (d, *J* = 19.5 Hz, $C_{A3}$), 115.0 (d, *J* = 14.7 Hz, $C_{C6}$), 114.9 ($C_{CF3}$), 113.5 ($C_{E2}$), 113.3 (d, *J* = 15.9 Hz, $C_{D6}$), 108.7 ($C_{F4}$), 98.1 (t, *J* = 26.5 Hz, $C_{D4}$), 97.4 (t, *J* = 26.9 Hz, $C_{C4}$), 72.4 ($C_{E5}$), 61.3 ($C_{E4}$); HRMS (ESI): *m/z* 968.0905 [$MH^+$]. Calcd. for $C_{38}H_{19}F_{12}IrN_3O_2^+$: 968.0892; Anal. Calcd. for $C_{38}H_{18}F_{12}IrN_3O_2$: C, 47.11; H, 1.87; N, 4.34. Found: C, 46.98; H, 1.97; N, 4.26. Due to extensive coupling to $^{19}$F nuclei, the $^{13}$C signals for ring G are stated as a range. Crystals for X-ray analysis were grown by slow diffusion of *n*-hexane into a DCM solution of **1a**.

**1b.** Isolated as an amorphous yellow powder (151 mg, 0.16 mmol, 30%). $^1$H NMR (600 MHz, $d_2$-1,1,2,2-TCE) δ (ppm) = 8.96 (ddd, *J* = 5.8, 1.6, 0.7 Hz, $1H_{A6}$), 8.52 (dt, *J* = 5.6, 1.3 Hz, $1H_{B6}$), 8.36 (d, *J* = 8.5 Hz, $1H_{A3}$), 8.16 (d, *J* = 7.4 Hz, $1H_{B3}$), 7.98 – 7.93 (m, $2H_{A4,\ F5}$), 7.73 (td, *J* = 7.4, 1.3 Hz, $1H_{B4}$), 7.35 – 7.29 (m, $2H_{A5,\ F3}$), 7.04 (ddd, *J* = 7.4, 5.6, 1.4 Hz, $1H_{B5}$), 6.56 (d, *J* = 9.0 Hz, $1H_{F2}$), 6.41 (ddd, *J* = 12.0, 9.2, 2.4 Hz, $1H_{C4}$), 6.32 (ddd, *J* = 12.0, 9.3, 2.4 Hz, $1H_{D4}$), 5.47 (dd, *J* = 8.7, 2.4 Hz, $1H_{C6}$), 5.19 (dd, *J* = 8.6, 2.4 Hz, $1H_{D6}$), 4.63 – 4.54 (m, $2H_{E4,\ E5}$), 4.36 – 4.29 (m, $1H_{E5}$); $^{19}$F{$^1$H} NMR (376 MHz, $d_2$-1,1,2,2-TCE) δ (ppm) = -60.36 (s, $3F_{CF3}$), -107.94 (d, *J* = 9.7 Hz, $1F_{dfppy}$), -108.78 (d, *J* = 10.2 Hz, $1F_{dfppy}$), -109.21 (d, *J* = 10.3 Hz, $1F_{dfppy}$), -109.98 (d, *J* = 9.8 Hz, $1F_{dfppy}$), -140.59 (d, *J* = 22.5 Hz, $1F_{G2/\ G6}$), -142.17 (d, *J* = 22.5 Hz, $1F_{G2/\ G6}$), -152.11 (t, *J* = 20.9 Hz, $1F_{G4}$), -159.31 (t, *J* = 19.5 Hz, $1F_{G3/\ G5}$), -161.08 (t, *J* = 22.1 Hz, $1F_{G3/\ G5}$); $^{13}$C NMR (151 MHz, $d_2$-1,1,2,2-TCE) δ (ppm) = 172.50 ($C_{F1}$), 165.0 – 160.0 ($C_{Ring\ G}$), 164.9 ($C_{A2}$), 164.7 ($C_{B2}$), 164.2 ($C_{F6}$), 162.4 (d, J = 259 Hz, $C_{D5}$), 162.3 (d, *J* = 249 Hz, $C_{C5}$), 161.2 (d, J = 261 Hz, $C_{D3}$), 160.6 Hz (d, J = 259 Hz, $C_{C3}$), 154.2 (d, *J* = 6.2 Hz, $C_{C1}$), 151.4 (d, *J* = 7.5 Hz, $C_{D1}$), 149.6 ($C_{B6}$), 149.0 ($C_{A6}$), 138.8 ($C_{A4}$), 138.3 ($C_{B4}$), 130.4 ($C_{F3}$), 128.6 ($C_{C2}$), 128.4 ($C_{D2}$), 128.0 ($C_{F5}$), 124.9 ($C_{F2}$), 122.9 ($C_{B3}$), 122.8 ($C_{A3}$), 122.5 ($C_{A5}$), 121.8 ($C_{B5}$), 115.3 ($C_{CF3}$), 114.0 (d, *J* = 15.7 Hz, $C_{D6}$), 113.5 (d, *J* = 16.5 Hz, $C_{C6}$), 113.1 ($C_{E2}$), 110.7 ($C_{F4}$), 97.9 (t, J = 25.9 Hz, $C_{C4}$), 96.8 (t, *J* = 27.9 Hz, $C_{D4}$), 71.5 ($C_{E5}$), 59.7 ($C_{E4}$); HRMS (ESI): *m/z* 968.0919 [$MH^+$]. Calcd. for $C_{38}H_{19}F_{12}IrN_3O_2^+$: 968.0892; Anal. Calcd. for $C_{38}H_{18}F_{12}IrN_3O_2$: C, 47.11; H, 1.87; N, 4.34; Anal. Calcd. for $C_{38}H_{18}F_{12}IrN_3O_2{\cdot}0.6CH_2Cl_2$: C, 45.46; H, 1.90; N, 4.12; Found: C, 45.30; H, 1.84; N, 4.11. Due to extensive coupling to $^{19}$F nuclei, the $^{13}$C signals for ring G are stated as a range. Crystals for X-ray analysis were grown by slow diffusion of *n*-hexane into a DCM solution of **1a**.

## ASSOCIATED CONTENT

## Supporting Information

The Supporting Information is available free of charge on the ACS Publications website at DOI: 10.1021/xxxxxxxx.

X-ray crystal structures CCDC-1850087, 1850088 (CIF)
NMR spectra, cyclic voltammograms, thermogravimetric analysis and PhOLED data (PDF); computational atomic coordinates (xyz).

## AUTHOR INFORMATION


### Corresponding Authors

Martin R. Bryce: m.r.bryce@durham.ac.uk
Yu Liu: yuliu@jlu.edu.cn
Dongxia Zhu: zhudx047@nenu.edu.cn


### Notes

The authors declare no competing financial interest.

## ACKNOWLEDGMENTS


Dr Alan Kenwright and Dr Juan Aguilar-Malavia are acknowledged for their help with the variable temperature NMR experiments. Prof. Andrew Beeby is acknowledged for his help with the variable temperature PL experiments. We thank the EPSRC for funding the work in Durham (grant EP/L02621X/1). NSFC (No. 51773078, 51473028), the key scientific and technological project of Jilin province (20160307016GX), the development and reform commission of Jilin province (20160058) are thanked for funding the work in China.


## REFERENCES


(1) Chen, Z. Q.; Bian, Z. Q.; Huang, C. H. Functional Ir(III) Complexes and Their Applications. *Adv. Mater.* **2010**, *22*, 1534–1539.

(2) *Iridium(III) in Optoelectronic and Photonics Applications*; Zysman-Colman, E., Ed.; John Wiley & Sons, 2017.

(3) Lowry, M. S.; Bernhard, S. Synthetically Tailored Excited States: Phosphorescent, Cyclometalated Iridium(III) Complexes and Their Applications. *Chem. Eur. J.* **2006**, *12*, 7970–7977.

(4) Lo, K. K.-W.; Tsang, K. H.-K.; Sze, K.-S.; Chung, C.-K.; Lee, T. K.-M.; Zhang, K. Y.; Hui, W.-K.; Li, C.-K.; Lau, J. S.-Y.; Ng, D. C.-M.; et al. Non-Covalent Binding of Luminescent Transition Metal Polypyridine Complexes to Avidin, Indole-Binding Proteins and Estrogen Receptors. *Coord. Chem. Rev.* **2007**, *251*, 2292–2310.

(5) Gao, R.; Ho, D. G.; Hernandez, B.; Selke, M.; Murphy, D.; Djurovich, P. I.; Thompson, M. E. Bis-Cyclometalated Ir(III) Complexes as Efficient Singlet Oxygen Sensitizers. *J. Am. Chem. Soc.* **2002**, *124*, 14828–14829.

(6) Yang, X.; Zhou, G.; Wong, W.-Y. Functionalization of Phosphorescent Emitters and Their Host Materials by Main-Group Elements for Phosphorescent Organic Light-Emitting Devices. *Chem. Soc. Rev.* **2015**, *44*, 8484–8575.

(7) Ulbricht, C.; Beyer, B.; Friebe, C.; Winter, A.; Schubert, U. S. Recent Developments in the Application of Phosphorescent Iridium(III) Complex Systems. *Adv. Mater.* **2009**, *21*, 4418–4441.

(8) Kwon, Y.; Han, S. H.; Yu, S.; Lee, J. Y.; Lee, K. M. Functionalized Phenylimidazole-Based Facial-Homoleptic Iridium(III) Complexes and Their Excellent Performance in Blue Phosphorescent Organic Light-Emitting Diodes. *J. Mater. Chem. C* **2018**, *6*, 4565–4572.

(9) Zhang, D.; Qiao, J.; Zhang, D.; Duan, L. Ultrahigh-Efficiency Green PHOLEDs with a Voltage under 3 V and a Power Efficiency of Nearly 110 Lm $W^{-1}$ at Luminance of 10 000 cd $m^{-2}$. *Adv. Mater.* **2017**, 1702847.

(10) Udagawa, K.; Sasabe, H.; Igarashi, F.; Kido, J. Simultaneous Realization of High EQE of 30%, Low Drive Voltage, and Low Efficiency Roll-Off at High Brightness in Blue Phosphorescent OLEDs. *Adv. Opt. Mater.* **2016**, *4*, 86–90.

(11) Li, C.; Fan, X.; Han, C.; Xu, H. A Ternary Phosphine Oxide Host Featuring Thermally Activated Delayed Fluorescence for Blue PHOLEDs with >20% EQE and Extremely Low Roll-Offs. *J. Mater. Chem. C* **2018**, *6*, 6747–6754.

(12) Miao, Y.; Tao, P.; Gao, L.; Li, X.; Wei, L.; Liu, S.; Wang, H.; Xu, B.; Zhao, Q. Highly Efficient Chlorine Functionalized Blue Iridium(III) Phosphors for Blue and White Phosphorescent Organic Light-Emitting Diodes with the External Quantum Efficiency Exceeding 20%. *J. Mater. Chem. C* **2018**, *6*, 6656–6665.

(13) Chi, Y.; Chou, P.-T. Transition-Metal Phosphors with Cyclometalating Ligands: Fundamentals and Applications. *Chem. Soc. Rev.* **2010**, *39*, 638–655.

(14) Ladouceur, S.; Zysman-Colman, E. Iridium Complexes A Comprehensive Survey of Cationic Iridium(III) Complexes Bearing Nontraditional Ligand Chelation Motifs. *Eur. J. Inorg. Chem.* **2013**, 2985–3007.

(15) Henwood, A. F.; Zysman-Colman, E. Lessons Learned in Tuning the Optoelectronic Properties of Phosphorescent Iridium(III) Complexes. *Chem. Commun.* **2017**, *53*, 807–826.

(16) Benjamin, H.; Zheng, Y.; Batsanov, A. S.; Fox, M. A.; Al-Attar, H. A.; Monkman, A. P.; Bryce, M. R. Sulfonyl-Substituted Heteroleptic Cyclometalated Iridium(III) Complexes as Blue Emitters for Solution-Processable Phosphorescent Organic Light-Emitting Diodes. *Inorg. Chem.* **2016**, *55*, 8612–8627.

(17) Yang, X.; Sun, N.; Dang, J.; Huang, Z.; Yao, C.; Xu, X.; Ho, C.-L.; Zhou, G.; Ma, D.; Zhao, X.; et al. Versatile Phosphorescent Color Tuning of Highly Efficient Borylated Iridium(III) Cyclometalates by Manipulating the Electron-Accepting Capacity of the Dimesitylboron Group. *J. Mater. Chem. C* **2013**, *1*, 3317–3326.

(18) Baranoff, E.; Curchod, B. F. E.; Frey, J.; Scopelliti, R.; Kessler, F.; Tavernelli, I.; Rothlisberger, U.; Gra, M.; Nazeeruddin, K. Acid-Induced Degradation of Phosphorescent Dopants for OLEDs and Its Application to the Synthesis of Tris-Heteroleptic Iridium(III) Bis-Cyclometalated Complexes. *Inorg. Chem.* **2012**, *51*, 215–224.

(19) Baranoff, E.; Jung, I.; Scopelliti, R.; Solari, E.; Grätzel, M.; Nazeeruddin, M. K. Room-Temperature Combinatorial Screening of Cyclometallated Iridium(III) Complexes for a Step towards Molecular Control of Colour Purity. *Dalton Trans.* **2011**, *40*, 6860–6867.

(20) Rausch, A. F.; Thompson, M. E.; Yersin, H. Blue Light Emitting Ir(III) Compounds for OLEDs - New Insights into Ancillary Ligand Effects on the Emitting Triplet State. *J. Phys. Chem. A* **2009**, *113*, 5927–5932.

(21) Li, J.; Djurovich, P. I.; Alleyne, B. D.; Yousufuddin, M.; Ho, N. N.; Thomas, J. C.; Peters, J. C.; Bau, R.; Thompson, M. E. Synthetic Control of Excited-State Properties in Cyclometalated Ir(III) Complexes Using Ancillary Ligands. *Inorg. Chem.* **2005**, *44*, 1713–1727.

(22) Gu, X.; Fei, T.; Zhang, H.; Xu, H.; Yang, B.; Ma, Y.; Liu, X. Tuning the Emission Color of Iridium(III) Complexes with Ancillary Ligands: A Combined Experimental and Theoretical Study. *Eur. J. Inorg. Chem.* **2009**, *2009*, 2407–2414.

(23) Chiu, Y.-C.; Chi, Y.; Hung, J.-Y.; Cheng, Y.-M.; Yu, Y.-C.; Chung, M.-W.; Lee, G.-H.; Chou, P.-T.; Chen, C.-C.; Wu, C.-C.; et al. Blue to True-Blue Phosphorescent Ir(III) Complexes Bearing a Nonconjugated Ancillary Phosphine Chelate: Strategic Synthesis, Photophysics, and Device Integration. *ACS Appl. Mater. Interfaces* **2009**, *1*, 433–442.

(24) Kim, T.; Lee, J.; Lee, S. U.; Lee, M. H. *O* -Carboranyl–Phosphine as a New Class of Strong-Field Ancillary Ligand in Cyclometalated Iridium(III) Complexes: Toward Blue Phosphorescence. *Organometallics* **2015**, *34*, 3455–3458.

(25) Henwood, A. F.; Evariste, S.; Slawin, A. M. Z.; Zysman-Colman, E. Rigid Biimidazole Ancillary Ligands as an Avenue to Bright Deep Blue Cationic iridium(III) Complexes. *Faraday Discuss.* **2014**, *174*, 165–182.

(26) Benjamin, H.; Fox, M. A.; Batsanov, A. S.; Al-Attar, H. A.; Li, C.; Ren, Z.; Monkman, A. P.; Bryce, M. R. Pyridylpyrazole N^N Ligands Combined with Sulfonyl-Functionalised Cyclometalating Ligands for Blue-Emitting I Iridium(III)

Complexes and Solution-Processable PhOLEDs. *Dalton Trans.* **2017**, *46*, 10996–11007.

(27) You, Y.; Seo, J.; Kim, S. H.; Kim, K. S.; Ahn, T. K.; Kim, D.; Park, S. Y. Highly Phosphorescent Iridium Complexes with Chromophoric 2-(2-Hydroxyphenyl)oxazole-Based Ancillary Ligands: Interligand Energy-Harvesting Phosphorescence. *Inorg. Chem.* **2008**, *47*, 1476–1487.

(28) Chao, K.; Shao, K.; Peng, T.; Zhu, D.; Wang, Y.; Liu, Y.; Su, Z.; Bryce, M. R. New Oxazoline- and Thiazoline-Containing Heteroleptic Iridium(III) Complexes for Highly-Efficient Phosphorescent Organic Light-Emitting Devices (PhOLEDs): Colour Tuning by Varying the Electroluminescence Bandwidth. *J. Mater. Chem. C* **2013**, *1*, 6800–6806.

(29) Benjamin, H.; Liang, J.; Liu, Y.; Geng, Y.; Liu, X.; Zhu, D.; Batsanov, A. S.; Bryce, M. R. Color Tuning of Efficient Electroluminescence in the Blue and Green Regions Using Heteroleptic Iridium Complexes with 2‑Phenoxyoxazole Ancillary Ligands. *Organometallics* **2017**, *36*, 1810–1821.

(30) Marchi, E.; Sinisi, R.; Bergamini, G.; Tragni, M.; Monari, M.; Bandini, M.; Ceroni, P. Easy Separation of Δ and Λ Isomers of Highly Luminescent [Ir(III)]-Cyclometalated Complexes Based on Chiral Phenol-Oxazoline Ancillary Ligands. *Chem. Eur. J.* **2012**, *18*, 8765–8773.

(31) Yi, S.; Kim, J. H.; Cho, Y. J.; Lee, J.; Choi, T. S.; Cho, D. W.; Pac, C.; Han, W. S.; Son, H. J.; Kang, S. O. Stable Blue Phosphorescence Iridium(III) Cyclometalated Complexes Prompted by Intramolecular Hydrogen Bond in Ancillary Ligand. *Inorg. Chem.* **2016**, *55*, 3324–3331.

(32) Li, L. P.; Yao, S. Y.; Ou, Y. L.; Wei, L. Q.; Ye, B. H. Diastereoselective Synthesis and Photophysical Properties of Bis-Cyclometalated Ir(III) Stereoisomers with Dual Stereocenters. *Organometallics* **2017**, *36*, 3257–3265.

(33) Bünzli, A. M.; Constable, E. C.; Housecroft, C. E.; Prescimone, A.; Zampese, J. A.; Longo, G.; Gil-Escrig, L.; Pertegás, A.; Ortí, E.; Bolink, H. J. Exceptionally Long-Lived Light-Emitting Electrochemical Cells: Multiple Intra-Cation π-Stacking Interactions in [Ir(C^N)2(N^N)][PF6] Emitters. *Chem. Sci.* **2015**, *6*, 2843–2852.

(34) Constable, E. C.; Housecroft, C. E.; Kopecky, P.; Martin, C. J.; Wright, I. A.; Zampese, J. A.; Bolink, H. J.; Pertegas, A. Solution, Structural and Photophysical Aspects of Substituent Effects in the N^N Ligand in [Ir(C^N)2(N^N)]+ Complexes. *Dalton Trans.* **2013**, *42*, 8086–8103.

(35) He, L.; Ma, D.; Duan, L.; Wei, Y.; Qiao, J.; Zhang, D.; Dong, G.; Wang, L.; Qiu, Y. Control of Intramolecular π-π Stacking Interaction in Cationic Iridium Complexes via Fluorination of Pendant Phenyl Rings. *Inorg. Chem.* **2012**, *51*, 4502–4510.

(36) Kumar, S.; Hisamatsu, Y.; Tamaki, Y.; Ishitani, O.; Aoki, S. Design and Synthesis of Heteroleptic Cyclometalated Iridium(III) Complexes Containing Quinoline-Type Ligands That Exhibit Dual Phosphorescence. *Inorg. Chem.* **2016**, *55*, 3829–3843.

(37) Li, P.; Shan, G. G.; Cao, H. T.; Zhu, D. X.; Su, Z. M.; Jitchati, R.; Bryce, M. R. Intramolecular π Stacking in Cationic Iridium(III) Complexes with Phenyl-Functionalized Cyclometalated Ligands: Synthesis, Structure, Photophysical Properties, and Theoretical Studies. *Eur. J. Inorg. Chem.* **2014**, 2376–2382.

(38) Congrave, D. G.; Hsu, Y.-T.; Batsanov, A. S.; Beeby, A.; Bryce, M. R. Sky-Blue Emitting Bridged Diiridium Complexes: Beneficial Effects of Intramolecular π–π Stacking. *Dalton Trans.* **2018**, *47*, 2086–2098.

(39) Cockroft, S. L.; Hunter, C. A.; Lawson, K. R.; Perkins, J.; Urch, C. J. Electrostatic Control of Aromatic Stacking Interactions. *J. Am. Chem. Soc.* **2005**, *127*, 8594–8595.

(40) Cozzi, F.; Cinquini, M.; Annuziata, R.; Siegel, J. S. Dominance of Polar/pi over Charge-Transfer Effects in Stacked Phenyl Interactions. *J. Am. Chem. Soc.* **1993**, *115*, 5330–5331.

(41) Cozzi, F.; Ponzini, F.; Annunziata, R.; Cinquini, M.; Siegel, J. S. Polar Interactions between Stacked Pi Systems in Fluorinated 1,8-Diarylnaphthalenes: Importance of Quadrupole Moments in Molecular Recognition. *Angew. Chem. Int. Ed. Engl.* **1995**, *34*, 1019–1020.

(42) Cockroft, S. L.; Hunter, C. A. Chemical Double-Mutant Cycles : Dissecting Non-Covalent Interactions. *Chem. Soc. Rev.* **2007**, *36*, 172–188.

(43) Camara-Campos, A.; Musumeci, D.; Hunter, C. A.; Turega, S. Chemical Double Mutant Cycles for the Quantification of Cooperativity in H-Bonded Complexes. *J. Am. Chem. Soc.* **2009**, *131*, 18518–18524.

(44) Adams, H.; Carver, F. J.; Hunter, C. A.; Morales, J. C.; Seward, E. M. Chemical Double-Mutant Cycles for the Measurement of Weak Intermolecular Interactions: Edge-to-Face Aromatic Interactions. *Angew. Chem. Int. Ed. Engl.* **1996**, *35*, 1542–1544.

(45) Li, T.-Y.; Zheng, Y.-X.; Zhou, Y.-H. Iridium(III) Phosphorescent Complexes with Dual Stereogenic Centers: Single Crystal, Electronic Circular Dichroism Evidence and Circularly Polarized Luminescence Properties. *Dalton Trans.* **2016**, *45*, 19234–19237.

(46) Bandini, M.; Cozzi, P. G.; Gazzano, M.; Umani-Ronchi, A. An Effective and Useful Synthesis of Enantiomerically Enriched Arylglycinols. *Eur. J. Org. Chem.* **2001**, 1937–1942.

(47) Wang, J.; Luis, J.; Pozo, C.; Sorochinsky, A. E.; Fustero, S.; Soloshonok, V. A.; Liu, H. Fluorine in Pharmaceutical Industry : Fluorine-Containing Drugs Introduced to the Market in the Last Decade ( 2001 − 2011 ). *Chem. Rev.* **2014**, *114*, 2432–2506.

(48) Martir, D. R.; Momblona, C.; Pertegás, A.; Cordes, D. B.; Slawin, A. M. Z.; Bolink, H. J.; Zysman-Colman, E. Chiral Iridium(III) Complexes in Light-Emitting Electrochemical Cells: Exploring the Impact of Stereochemistry on the Photophysical Properties and Device Performances. *ACS Appl. Mater. Interfaces* **2016**, *8*, 33907–33915.

(49) Cudre, Y.; de Carvalho, F. F.; Burgess, G. R.; Male, L.; Pope, S. J. A.; Tavernelli, I.; Baranoff, E. Tris-Heteroleptic Iridium Complexes Based on Cyclometalated Ligands with Different Cores. *Inorg. Chem.* **2017**, *56*, 11565–11576.

(50) Feldman, J.; Vo, G. D.; McLaren, C. D.; Gehret, T. C.; Park, K. H.; Meth, J. S.; Marshall, W. J.; Buriak, J.; Bryman, L. M.; Dobbs, K. D.; et al. Highly Quantum Efficient Phosphorescent Sky Blue Emitters Based on Diastereomeric Iridium(III) Complexes of Atropisomeric 5-Aryl-4H-1,2,4-Triazole Ligands. *Organometallics* **2015**, *34*, 3665–3669.

(51) Bourhis, L. J.; Dolomanov, O. V; Gildea, R. J.; Howard, J. A. K.; Puschmann, H. OLEX2: A Complete Structure Solution, Refinement and Analysis Program. *J. Appl. Cryst.* **2009**, *42*, 339-341.

(52) Berger, S.; Braun, S.; Kalinowski, H.-O. *NMR Spectroscopy of the Non-Metallic Elements*, 1st edition; Wiley, 1997.

(53) Banks, R. E.; Haszeldine, R. N. Heterocyclic Polyfluoro-Compounds. Part X. Nucleophilic Substitution in Tetrafluoropyrimidine. *J. Chem. Soc* **1967**, 1822–1826.

(54) Klauke, E.; Oehlmann, L.; Baasner, B. Fluorinated Heterocyclic Compounds: Selective Chlorine/ Fluorine Exchange Reactions on Pyrimidines. *J. Fluor. Chem.* **1982**, *21*, 495–513.

(55) Zhou, J.; Kuntze-Fechner, M. W.; Bertermann, R.; Paul, U. S. D.; Berthel, J. H. J.; Friedrich, A.; Du, Z.; Marder, T. B.; Radius, U. Preparing (Multi)Fluoroarenes as Building Blocks for Synthesis: Nickel-Catalyzed Borylation of Polyfluoroarenes via C-F Bond Cleavage. *J. Am. Chem. Soc.* **2016**, *138*, 5250–5253.

(56) Abraham, R. J.; Macdonald, D. B.; Pepper, E. S. The Nuclear Magnetic Resonance Spectra of Fluorobenzenes. II. The Effect of Substituents on the Meta and Para Fluorine-Fluorine Coupling Constants. *J. Am. Chem. Soc.* **1968**, *90*, 147–153.

(57) Günther, H. *NMR Spectroscopy: Basic Principles, Concepts and Applications in Chemistry*, Second edition; John Wiley & Sons: Chichester, 1995.

(58) Congrave, D. G.; Hsu, Y.; Batsanov, A. S.; Beeby, A.; Bryce, M. R. Synthesis, Diastereomer Separation, and Optoelectronic and Structural Properties of Dinuclear Cyclometalated Iridium(III) Complexes with Bridging Diarylhydrazide Ligands. *Organometallics* **2017**, *36*, 981–993.

(59) Yang, X.; Xu, X.; Dang, J.; Zhou, G.; Ho, C.-L.; Wong, W.-Y. From Mononuclear to Dinuclear Iridium(III) Complex: Effective Tuning of the Optoelectronic Characteristics for Organic Light-Emitting Diodes. *Inorg. Chem.* **2016**, *55*, 1720–1727.

(60) Frey, J.; Curchod, B. F. E.; Scopelliti, R.; Tavernelli, I.; Rothlisberger, U.; Nazeeruddin, M. K.; Baranoff, E. Structure-Property Relationships Based on Hammett Constants in

Cyclometalated iridium(III) Complexes: Their Application to the Design of a Fluorine-Free FIrPic-like Emitter. *Dalton Trans.* **2014**, *43*, 5667–5679.

(61) Tamayo, A. B.; Alleyne, B. D.; Djurovich, P. I.; Lamansky, S.; Tsyba, I.; Ho, N. N.; Bau, R.; Thompson, M. E. Synthesis and Characterization of Facial and Meridional Tris-Cyclometalated iridium(III) Complexes. *J. Am. Chem. Soc.* **2003**, *125*, 7377–7387.

(62) Sajoto, T.; Djurovich, P. I.; Tamayo, A.; Yousufuddin, M.; Bau, R.; Thompson, M. E.; Holmes, R. J.; Forrest, S. R. Blue and near-UV Phosphorescence from Iridium Complexes with Cyclometalated Pyrazolyl or N-Heterocyclic Carbene Ligands. *Inorg. Chem.* **2005**, *44*, 7992–8003.

(63) Sajoto, T.; Djurovich, P. I.; Tamayo, A. B.; Oxgaard, J.; Goddard, W. A.; Thompson, M. E. Temperature Dependence of Blue Phosphorescent Cyclometalated Ir(III) Complexes. *J. Am. Chem. Soc.* **2009**, *131*, 9813–9822.

(64) Mao, H. T.; Zang, C. X.; Wen, L. L.; Shan, G. G.; Sun, H. Z.; Xie, W. F.; Su, Z. M. Ir(III) Phosphors Modified with Fluorine Atoms in Pyridine-1,2,4-Triazolyl Ligands for Efficient OLEDs Possessing Low-Efficiency Roll-Off. *Organometallics* **2016**, *35*, 3870–3877.

(65) Sivasubramaniam, V.; Brodkorb, F.; Hanning, S.; Loebl, H. P.; van Elsbergen, V.; Boerner, H.; Scherf, U.; Kreyenschmidt, M. Fluorine Cleavage of the Light Blue Heteroleptic Triplet Emitter FIrpic. *J. Fluor. Chem.* **2009**, *130*, 640–649.

(66) Tordera, D.; Delgado, M.; Orti, E.; Bolink, H. J.; Frey, J.; Nazeeruddin, M. K.; Baranoff, E. Stable Green Electroluminescence from an Iridium Tris-Heteroleptic Ionic Complex. *Chem. Mater.* **2012**, *24*, 1896–1903.

(67) Tordera, D.; Serrano-Perez, J. J.; Pertegas, A.; Orti, E.; Bolink, H. J.; Baranoff, E.; Nazeeruddin, M. K.; Frey, J. Correlating the Lifetime and Fluorine Content of Iridium(III) Emitters in Green Light-Emitting Electrochemical Cells. *Chem. Mater.* **2013**, *25*, 3391–3397.

(68) Baranoff, E.; Curchod, B. F. E. FIrpic: Archetypal Blue Phosphorescent Emitter for Electroluminescence. *Dalton Trans.* **2015**, *44*, 8318–8329.

(69) Frisch, M. J.; Trucks, G.W.; Schlegel, H. B.; Scuseria, G. E.; Robb, M. A.; Cheeseman, J. R.; Scalmani, G.; Barone, V.;Mennucci, B.; Petersson, G. A.; Nakatsuji, H.; Caricato, M.; Li, X.; Hratchian, H. P.; Izmaylov, A. F.; Bloino, J.; Zheng, G.; Sonnenber, D. J. Gaussian 09. *Gaussian, Inc. Wallingford CT* **2009**, 2–3.

(70) Becke, A. D. Density-Functional Thermochemistry. III. The Role of Exact Exchange. *J. Chem. Phys.* **1993**, *98*, 5648.

(71) Lee, C.; Yang, W.; Parr, R. G. Development of the Colle-Salvetti Correlation-Energy Formula into a Functional of the Electron Density. *Phys. Rev. B* **1988**, *37*, 785–789.

(72) Hay, P. J.; Wadt, W. R. Ab Initio Effective Core Potentials for Molecular Calculations. Potentials for the Transition Metal Atoms Sc to Hg. *J. Chem. Phys.* **1985**, *82*, 270–283.

(73) Wadt, W. R.; Hay, P. J. Ab Initio Effective Core Potentials for Molecular Calculations. Potentials for Main Group Elements Na to Bi. *J. Chem. Phys.* **1985**, *82*, 284–298.

(74) Hay, P. J.; Wadt, W. R. Ab Initio Effective Core Potentials for Molecular Calculations. Potentials for K to Au Including the Outermost Core Orbitals. *J. Chem. Phys.* **1985**, *82*, 293–310.

(75) Petersson, G. A.; Bennett, A.; Tensfeldt, T. G.; Al-Laham, M. A.; Shirley, W. A.; Mantzaris, J. A Complete Basis Set Model Chemistry. II. Open-Shell Systems and the Total Energies of the First-Row Atoms. *J. Chem. Phys.* **1991**, *94*, 6081–6090.

(76) Melorose, J.; Perroy, R.; Careas, S. A Complete Basis Set Model Chemistry. I. The Total Energies of Closed-Shell Atoms and Hydrides of the First-Row Elements. *J. Chem. Phys.* **1988**, *89*, 2193–2218.

(77) Allouche, A.-R. Gabedit: A Graphical User Interface For Computational Chemistry Softwares. *J. Comput. Chem.* **2011**, *32*, 174–182.

(78) O'Boyle, N. M.; Tenderholt, A. L.; Langner, K. M. Cclib: A Library for Package-Independent Computational Chemistry Algorithms. *J. Comput. Chem.* **2008**, *29*, 839–845.

(79) Sheldrick, G. M. A Short History of SHELX. *Acta Crystallogr. A* **2008**, *A64*, 112–122.

(80) Sheldrick, G. M. Crystal Structure Refinement With SHELXL. *Acta Crystallogr. C* **2015**, *71*, 3–8.

(81) Pålsson, B. L.; Monkman, A. P. Measurements of Solid-State Photoluminescence Quantum Yields of Films Using a Fluorimeter. *Adv. Mater.* **2002**, *14*, 757–758.

(82) Sprouse, S.; King, K. A.; Spellane, P. J.; Watts, R. J. Photophysical Effects of Metal-Carbon Bonds in Ortho-Metalated Complexes of Ir (III) and Rh (III). *J. Am. Chem. Soc.* **1984**, *106*, 6647–6653.

Table of contents synopsis

Two diastereomeric cyclometalated iridium complexes **1a** and **1b** were synthesised and easily separated. Different intramolecular π–π interactions between a pendant perfluoroaryl group and a cyclometalating ligand in the complexes leads to diastereoselectivity and influences their photophysical properties. DFT/ TD-DFT calculations indicate that the pentafluorophenyl groups are ancillary, which may contribute to good PhOLED performance of **1a** ($EQE_{max}$ 25.8%) and low efficiency roll-off (24.9% at 1000 cd $m^{-2}$).

For Table of Contents Only

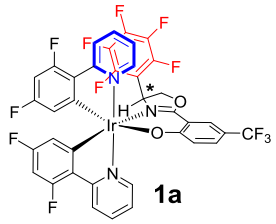

**1a**

**($\Lambda_S$, $\Delta_R$)** 66% yield

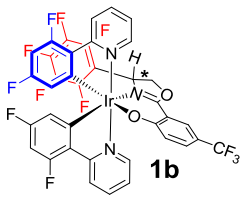

**1b**

**($\Lambda_R$, $\Delta_S$)** 30% yield

- Reproducible diastereoselectivity due to **intramolecular π–π interactions**
- **High EQE PhOLEDs** for a highly fluorinated Ir complex (25% at 270 cd $m^{-2}$)

## Supporting Information

# Intramolecular π–π Interactions with a Chiral Auxiliary Ligand Control Diastereoselectivity in a Cyclometalated Ir(III) Complex

Daniel G. Congrave,[1] Andrei S. Batsanov,[1] Mingxu Du,[2] Yu Liu,[2]* Dongxia Zhu,[3]* Martin R. Bryce[1]*

[1]Department of Chemistry, Durham University, South Road, Durham DH1 3LE, UK
[2] State Key Laboratory of Supramolecular Structure and Materials, College of Chemistry, Jilin University, Changchun 130012, People's Republic of China
[3]Key Laboratory of Nanobiosensing and Nanobioanalysis at Universities of Jilin Province, Department of Chemistry, Northeast Normal University, 5268 Renmin Street, Changchun, Jilin 130024, People's Republic of China

**Contents** **Page**

## Copies of NMR Spectra of Novel Compounds

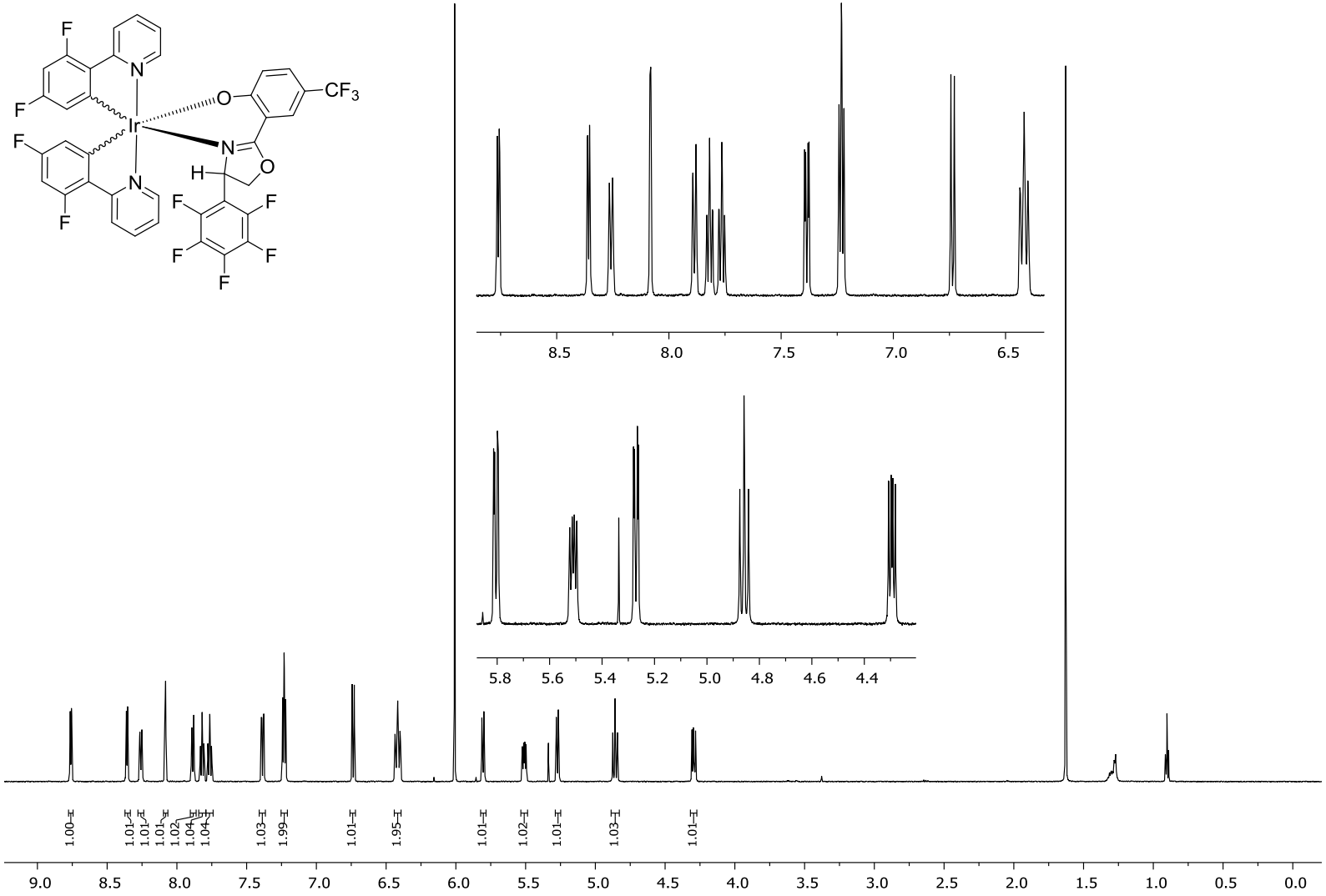


**Figure S1.** $^{1}$H NMR (600 MHz) spectrum of **1a** in 1,1,2,2-TCE-$d_2$

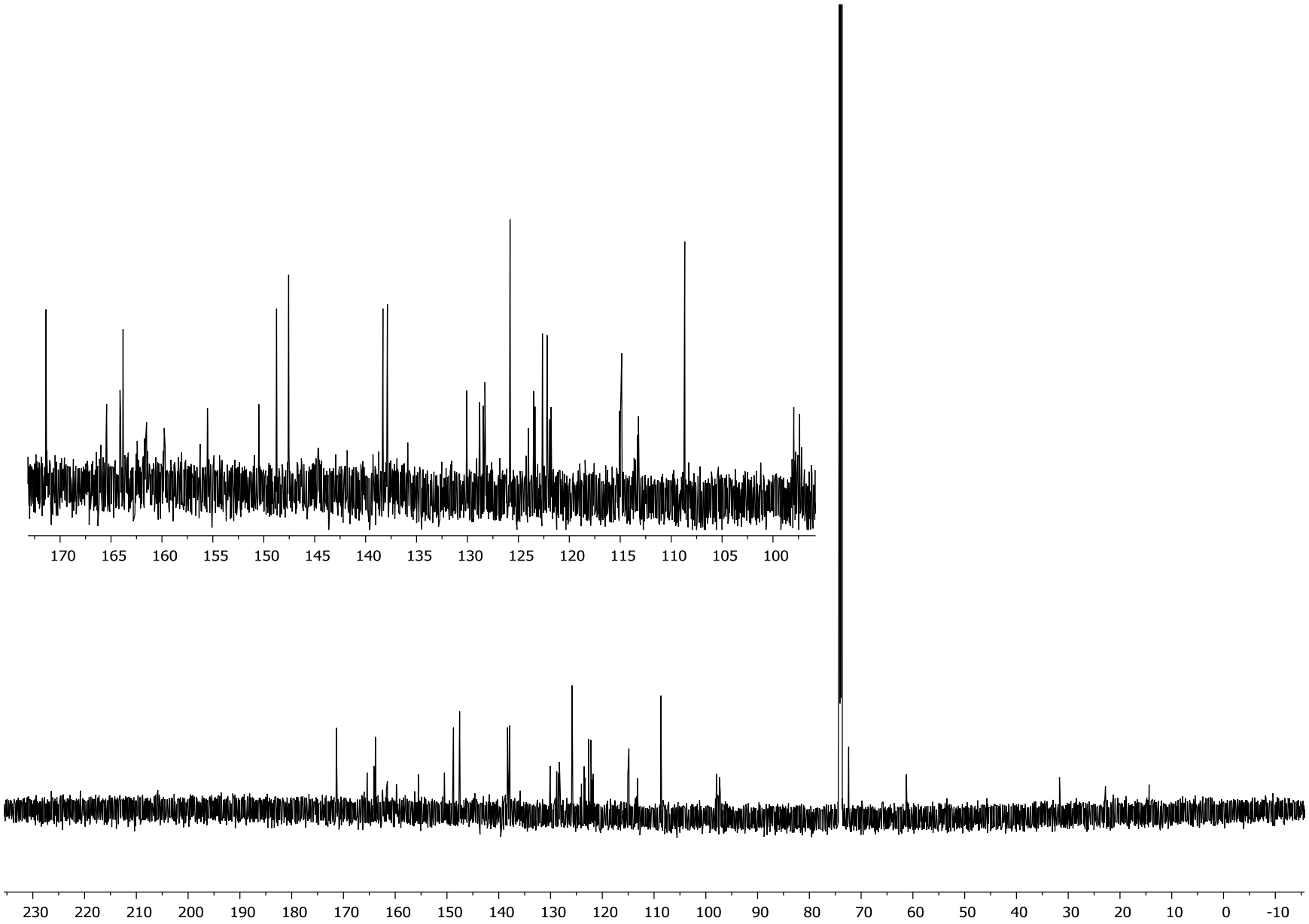


**Figure S2.** $^{13}$C NMR (151 MHz) spectrum of **1a** in 1,1,2,2-TCE-$d_2$

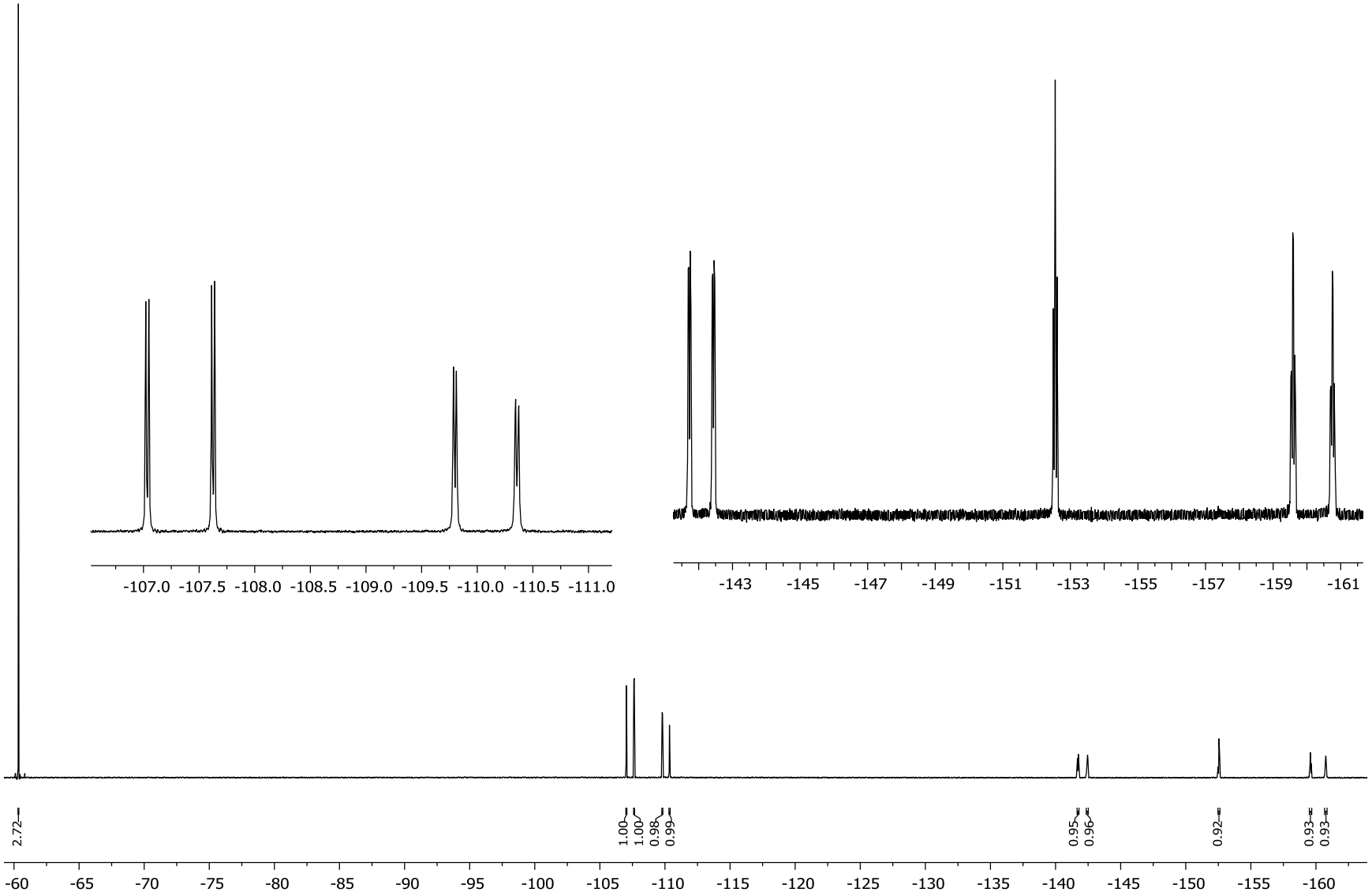


**Figure S3.** $^{19}F\{^{1}H\}$ NMR (376 MHz) spectrum of **1a** in 1,1,2,2-TCE-$d_2$

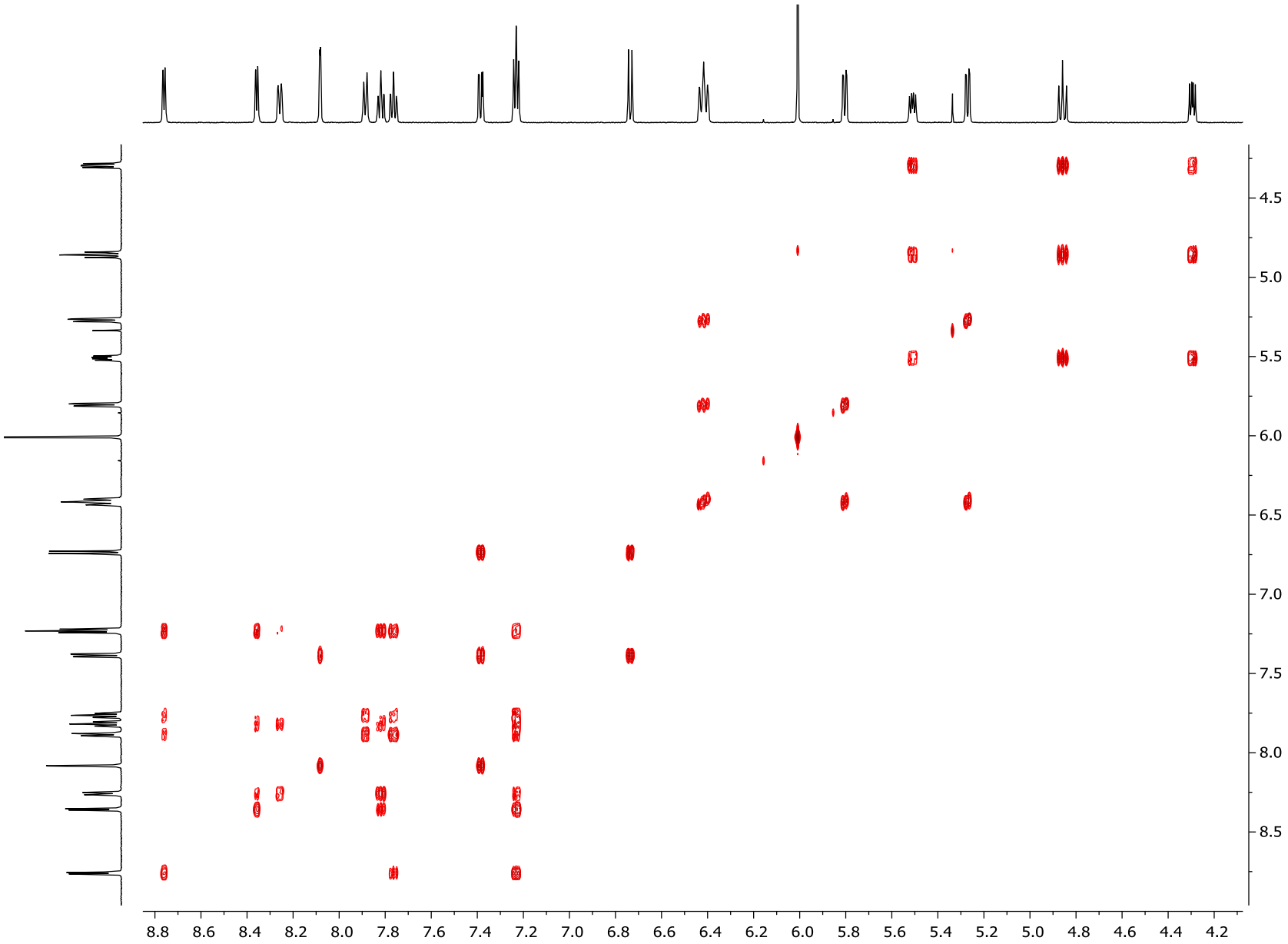


**Figure S4.** $^{1}H-^{1}H$ COSY NMR spectrum of **1a** in 1,1,2,2-TCE-$d_2$

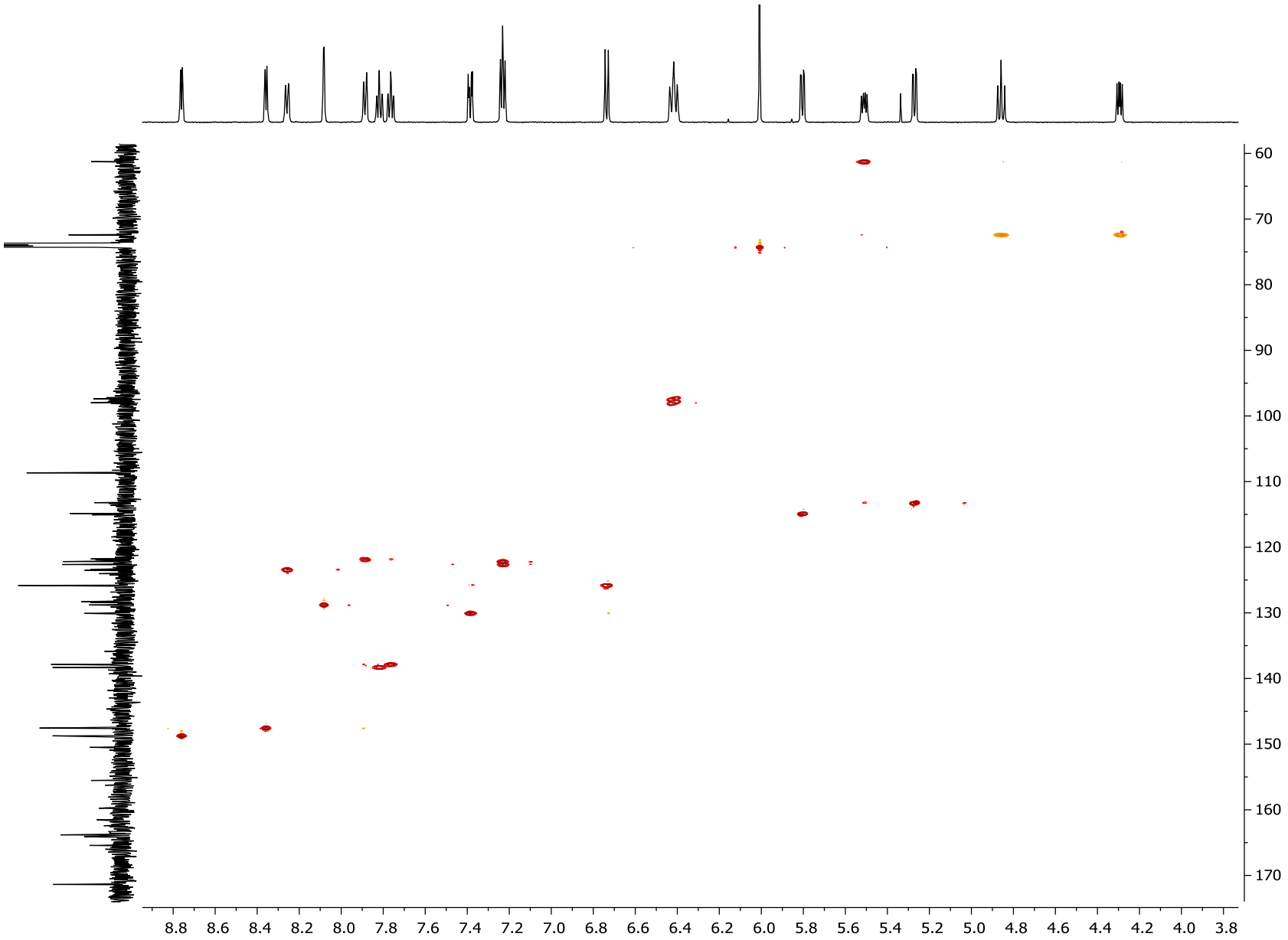


**Figure S5.** $^{1}H-^{13}C$ HSQC NMR spectrum of **1a** in 1,1,2,2-TCE-$d_2$

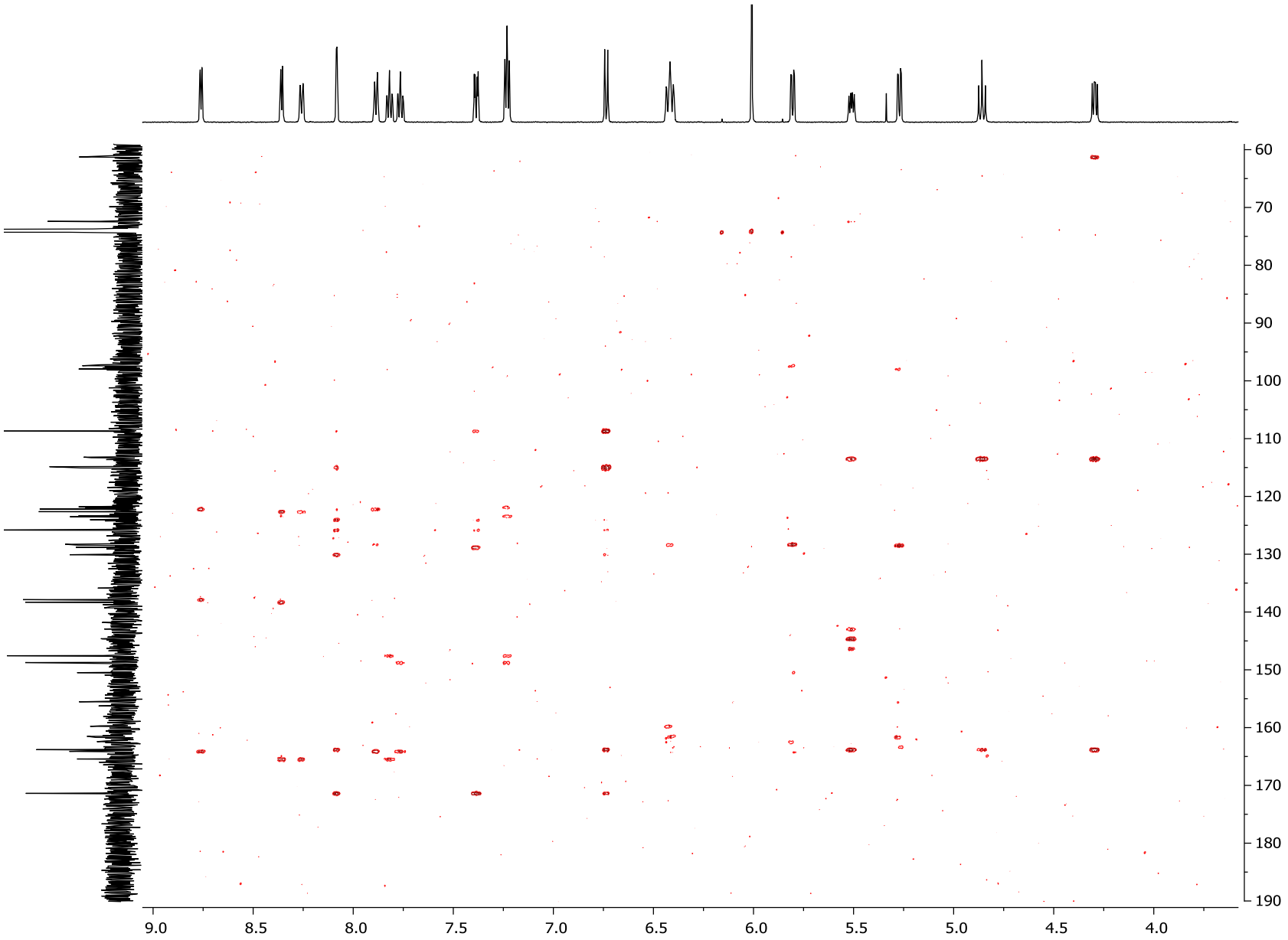


**Figure S6.** $^{1}H-^{13}C$ HMBC NMR spectrum of **1a** in 1,1,2,2-TCE-$d_2$

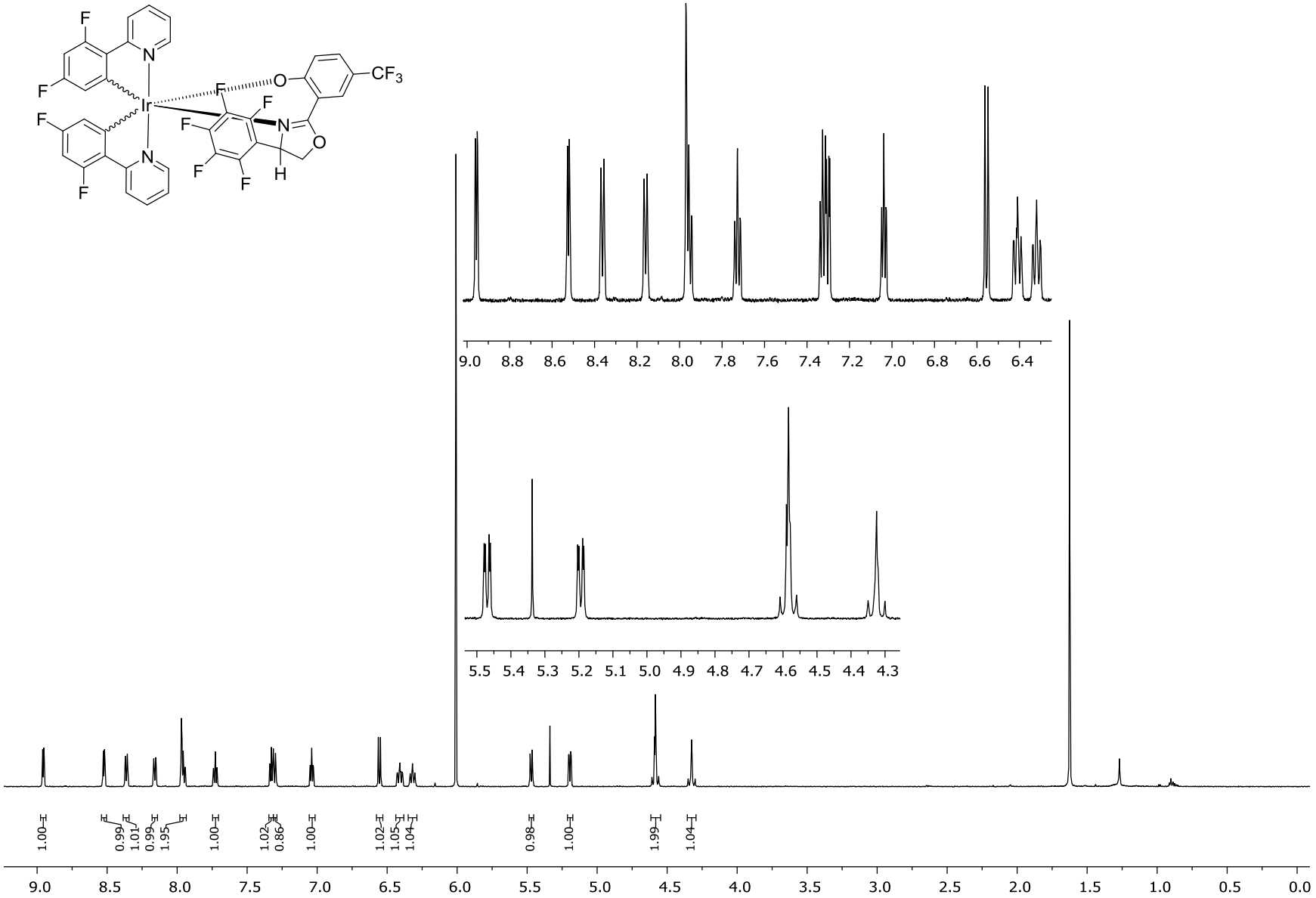


**Figure S7.** $^{1}$H NMR spectrum (600 Hz) of **1b** in 1,1,2,2-TCE-$d_2$

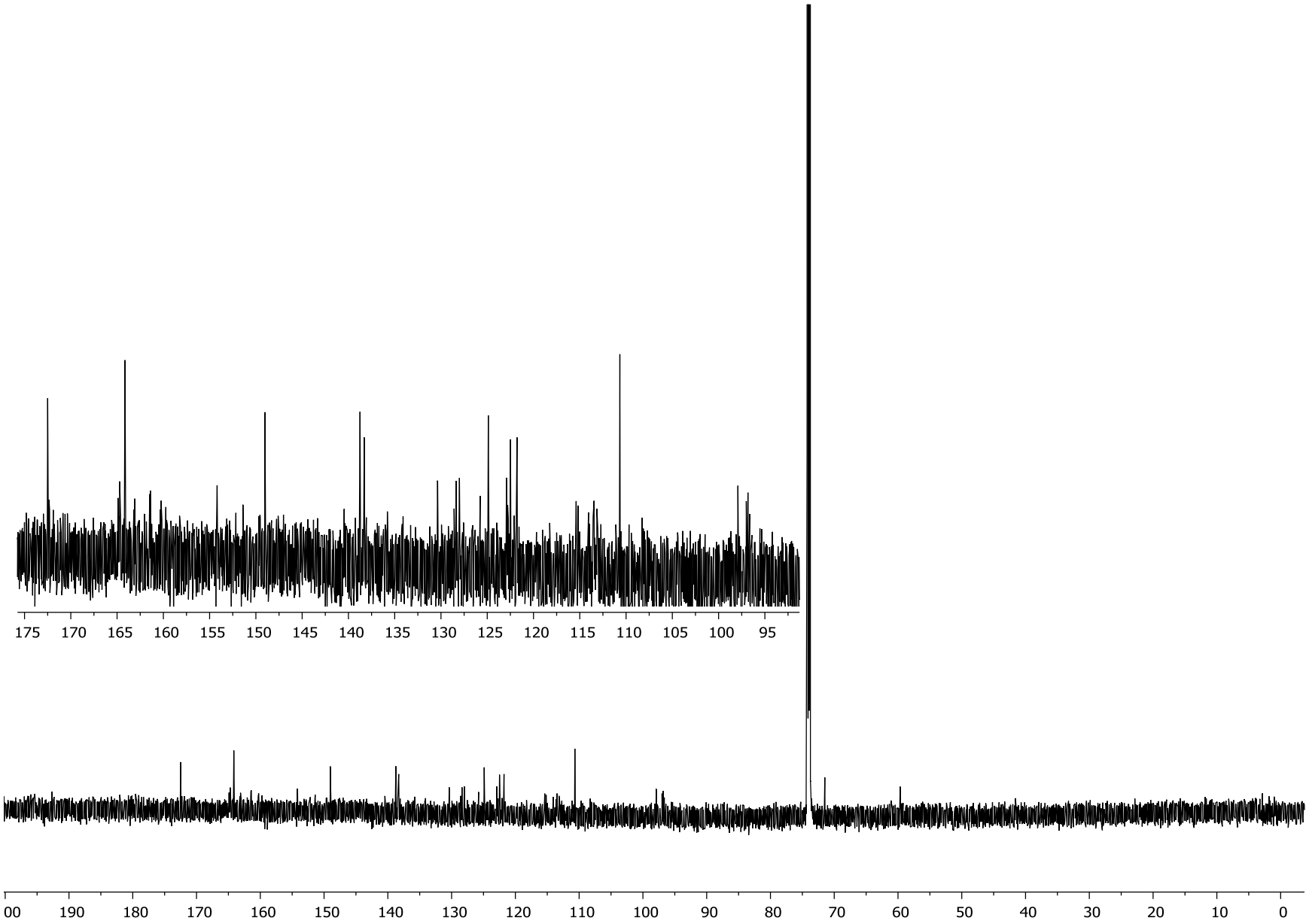


**Figure S8.** $^{13}C$ NMR spectrum (151 Hz) of **1b** in 1,1,2,2-TCE-$d_2$

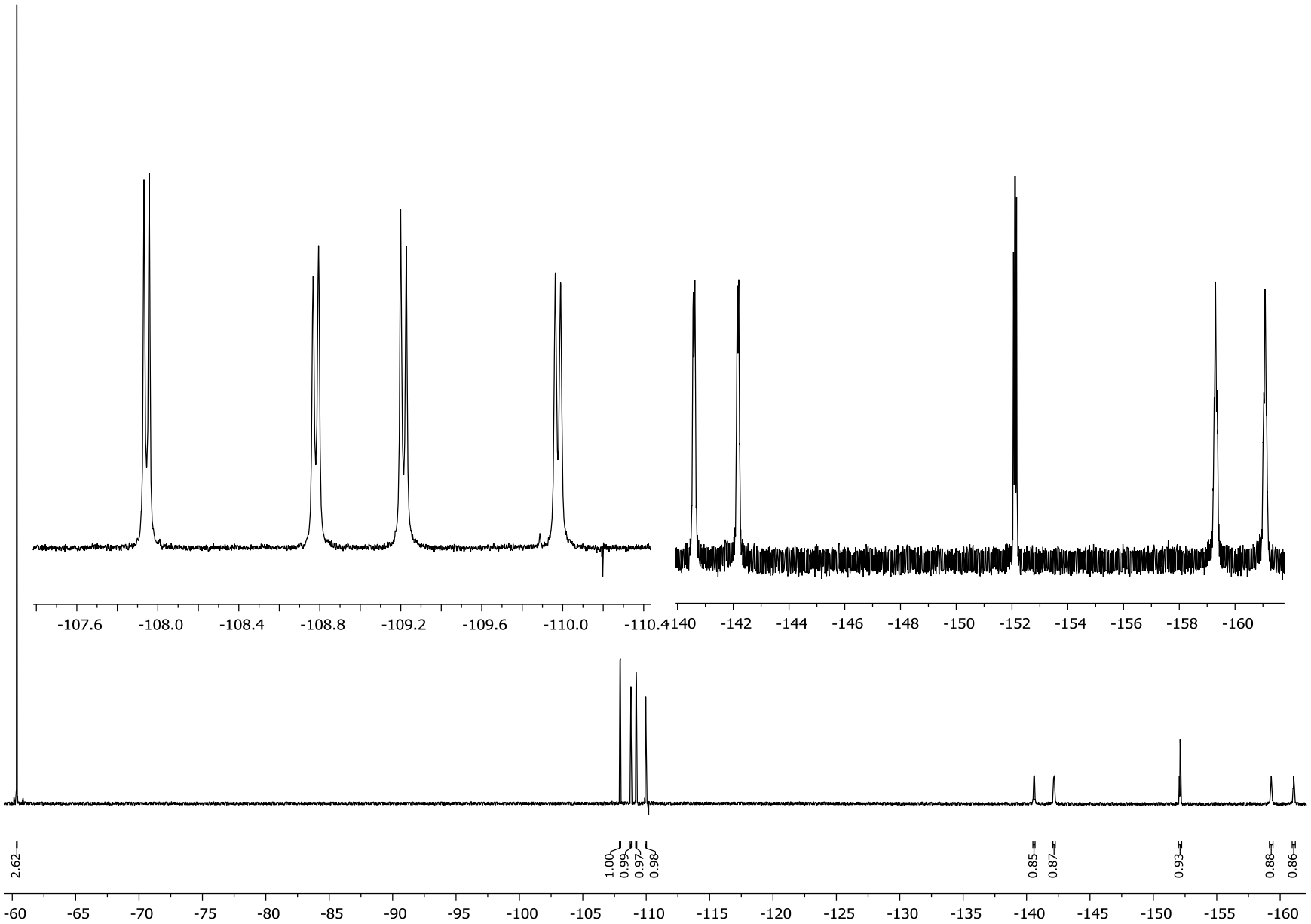


**Figure S9.** $^{19}F\{^{1}H\}$ NMR spectrum (376 Hz) of **1b** in 1,1,2,2-TCE-$d_2$

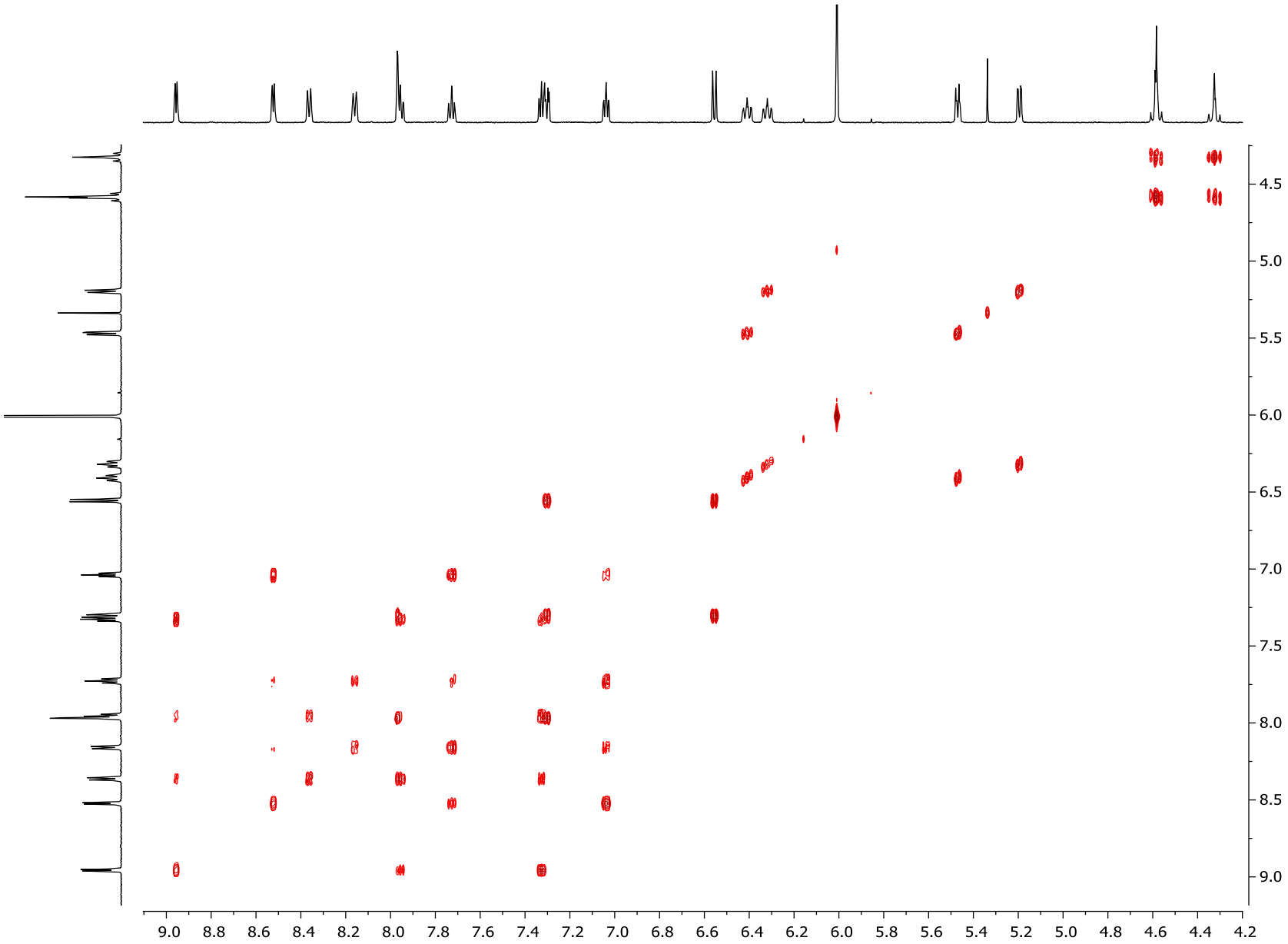


**Figure S10.** $^{1}H-^{1}H$ COSY NMR spectrum of **1b** in 1,1,2,2-TCE-$d_2$

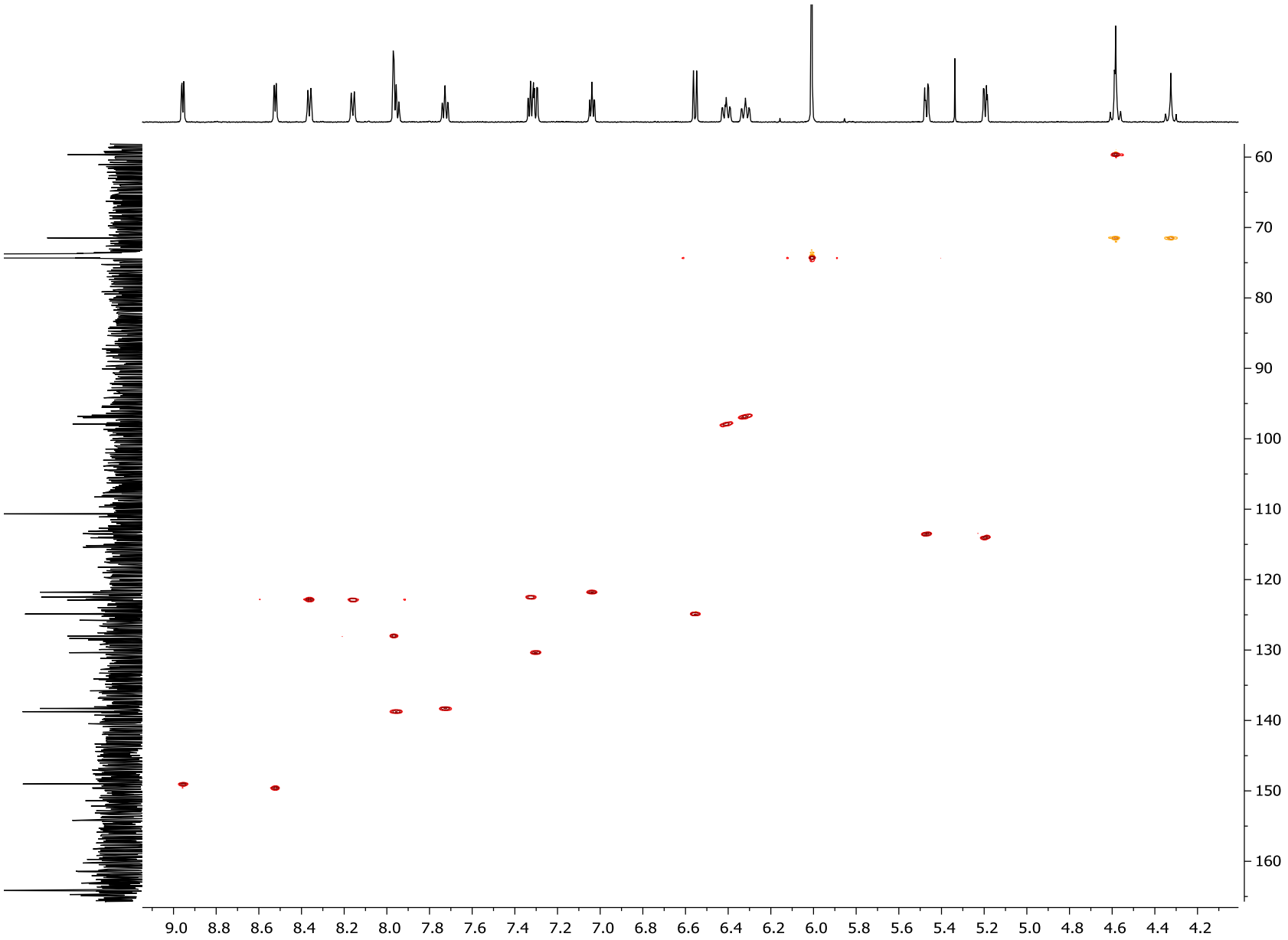


**Figure S11.** $^{1}H–^{13}C$ HSQC NMR spectrum of **1b** in 1,1,2,2-TCE-$d_2$

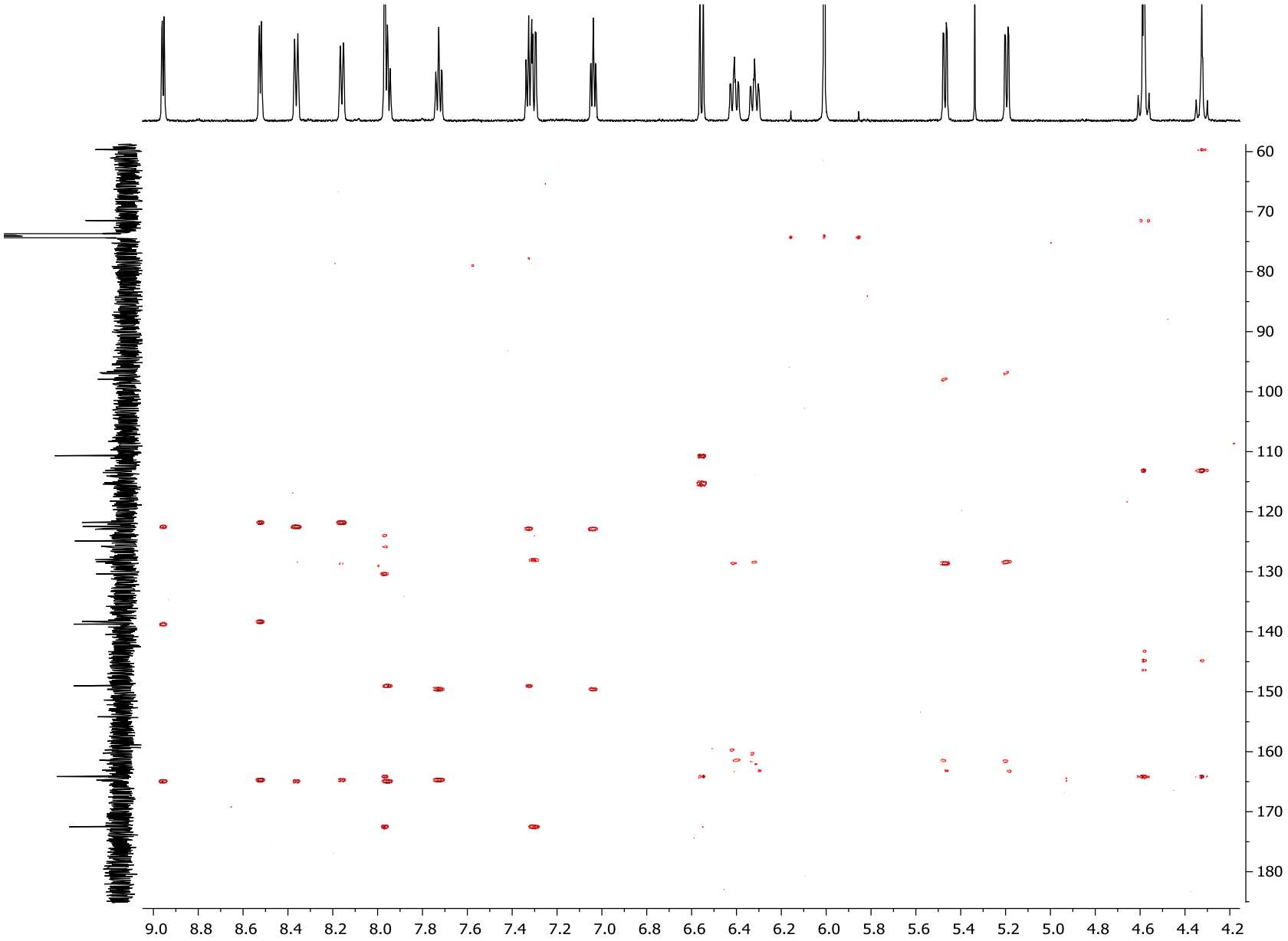


**Figure S12.** $^{1}H–^{13}C$ HMBC NMR spectrum of **1b** in 1,1,2,2-TCE-$d_2$

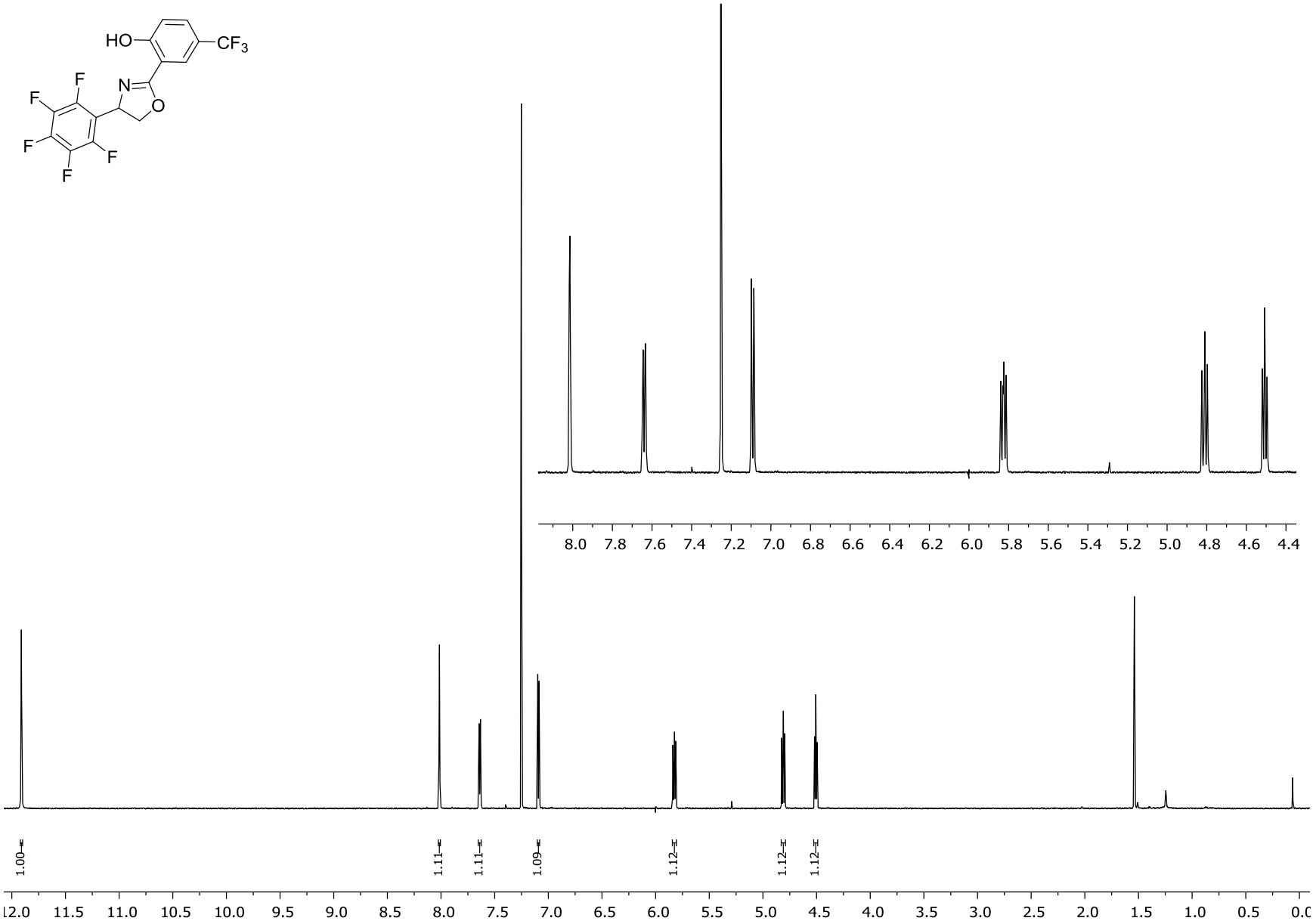


**Figure S13.** $^{1}$H NMR spectrum (700 MHz) of **6** in $CDCl_3$

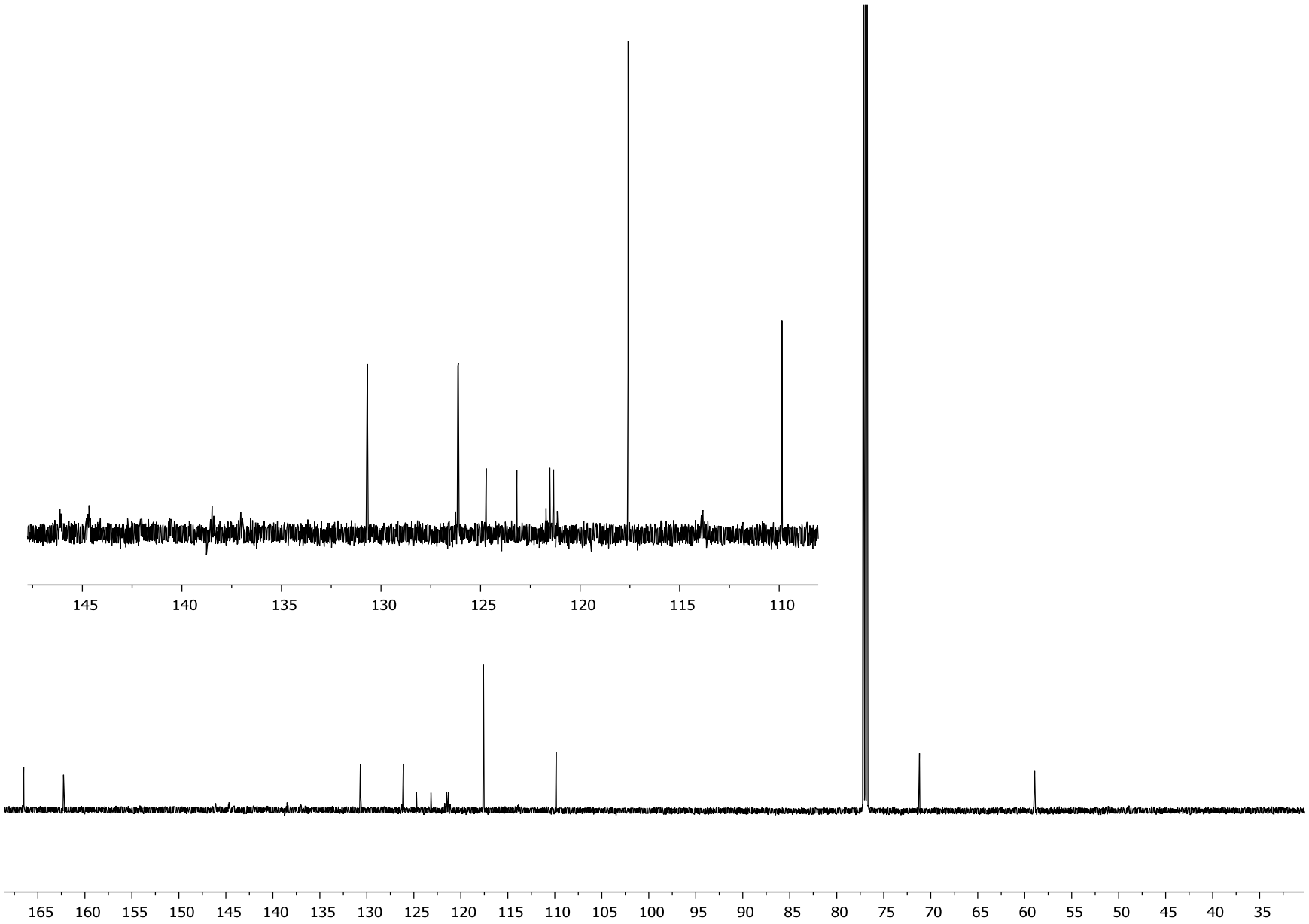


**Figure S14.** $^{13}C$ NMR spectrum (176 MHz) of **6** in $CDCl_3$

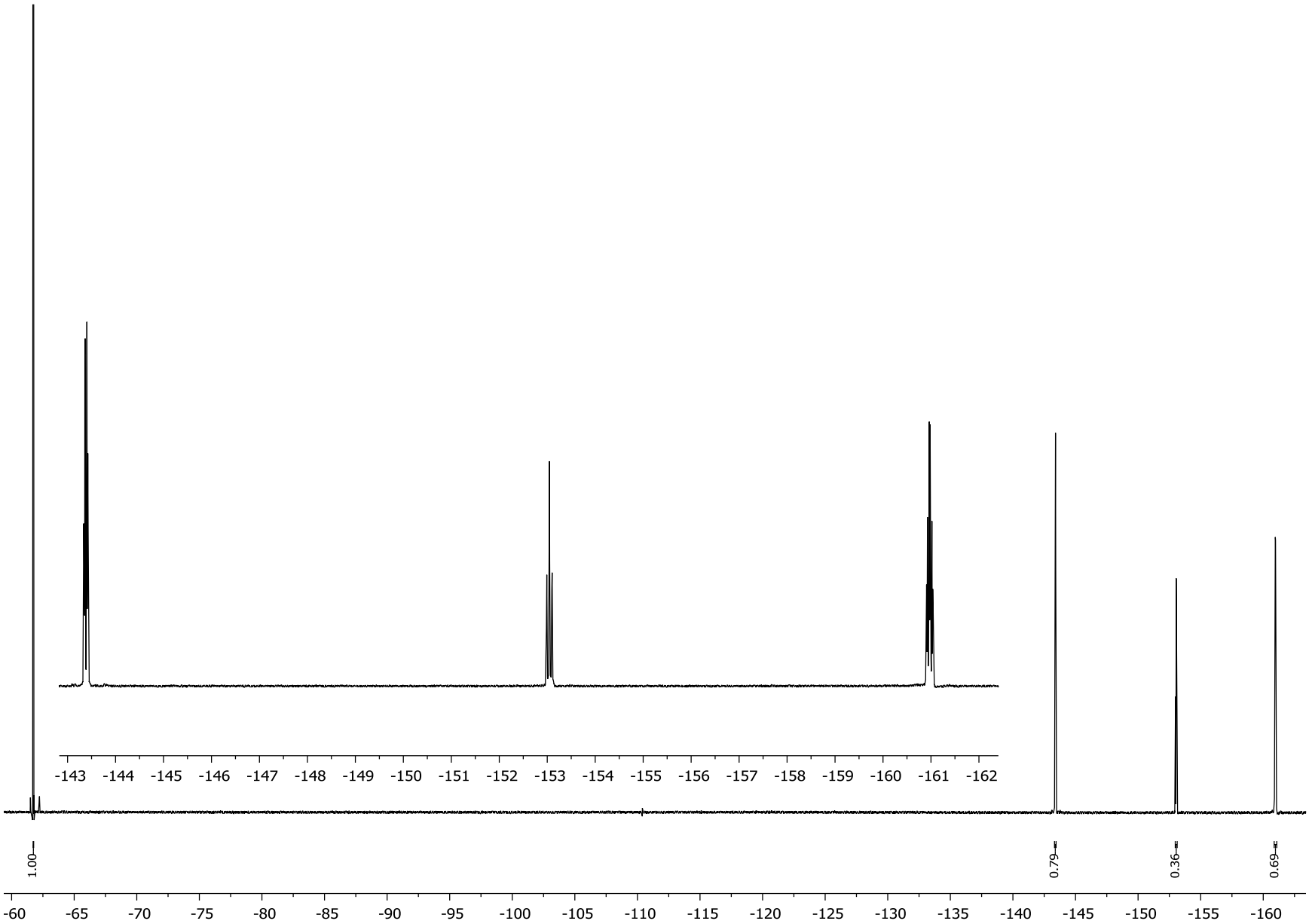


**Figure S15.** $^{19}F$ NMR spectrum (376 MHz) of **6** in $CDCl_3$

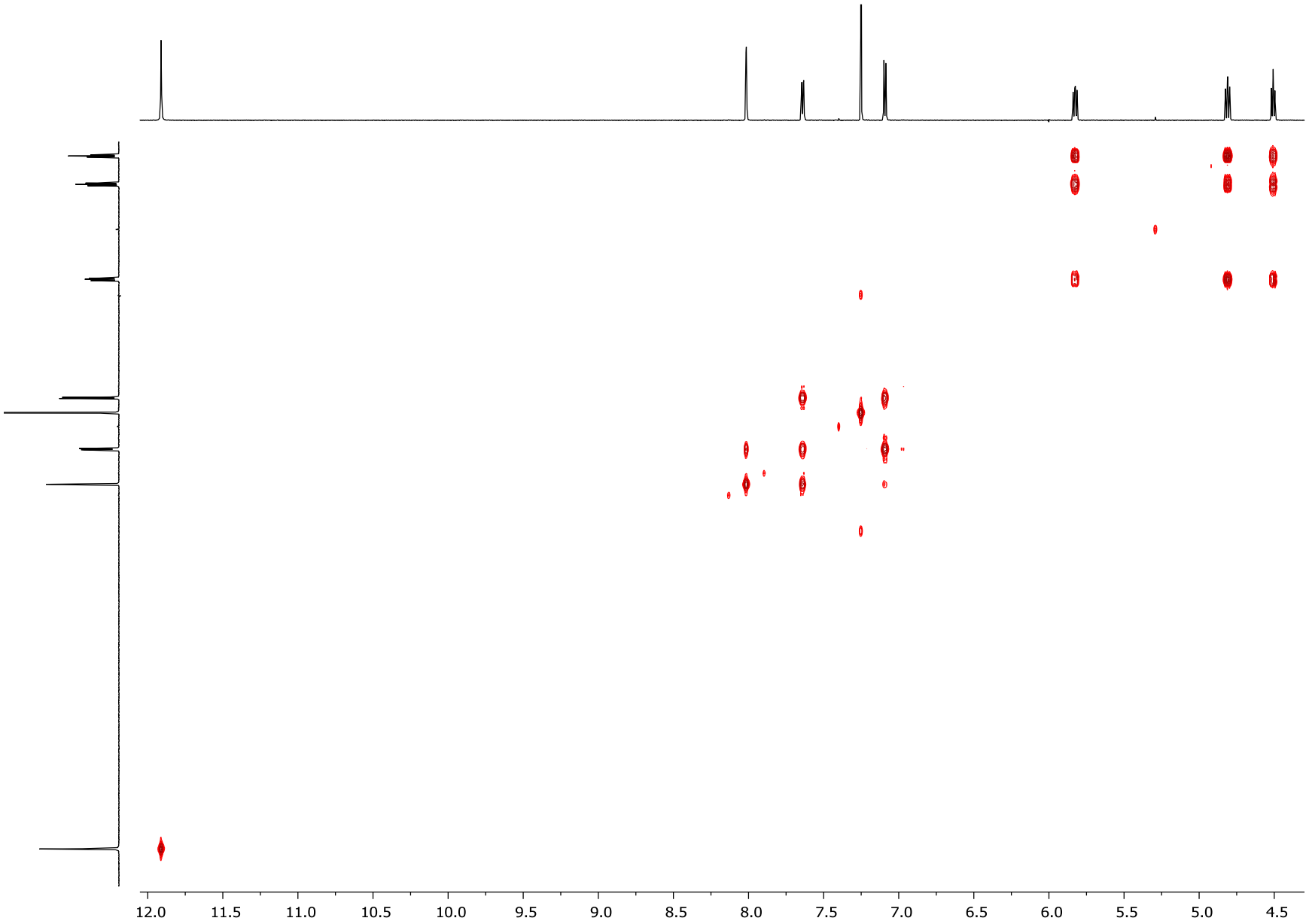


**Figure S16** $^{1}H-^{1}H$ COSY NMR spectrum of **6** in $CDCl_3$

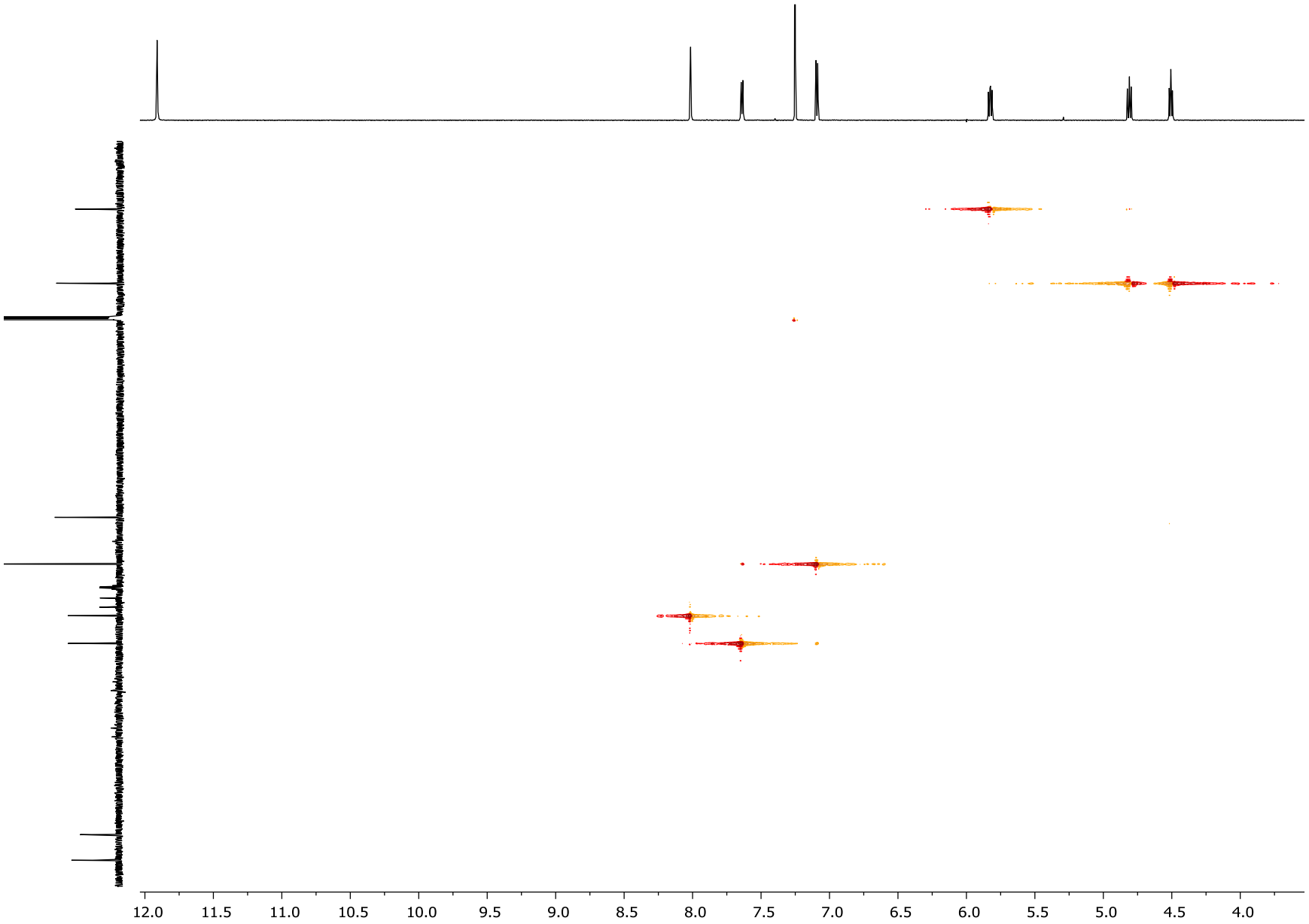


**Figure S17** $^{1}H-^{13}C$ HSQC NMR spectrum of **6** in $CDCl_3$

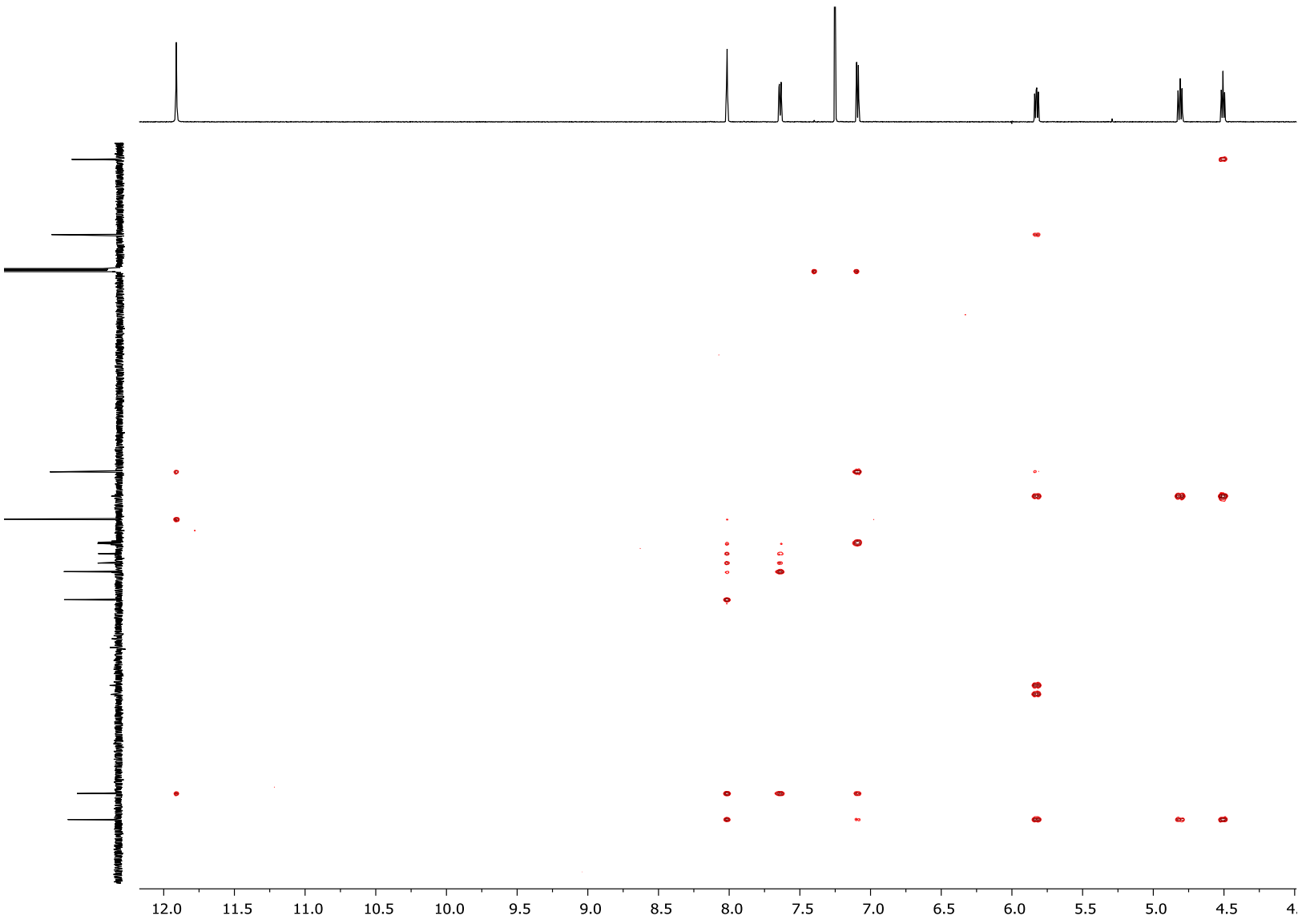


**Figure S18.** $^{1}H–^{13}C$ HMBC NMR spectrum of **6** in $CDCl_3$

## UV Detector Trace

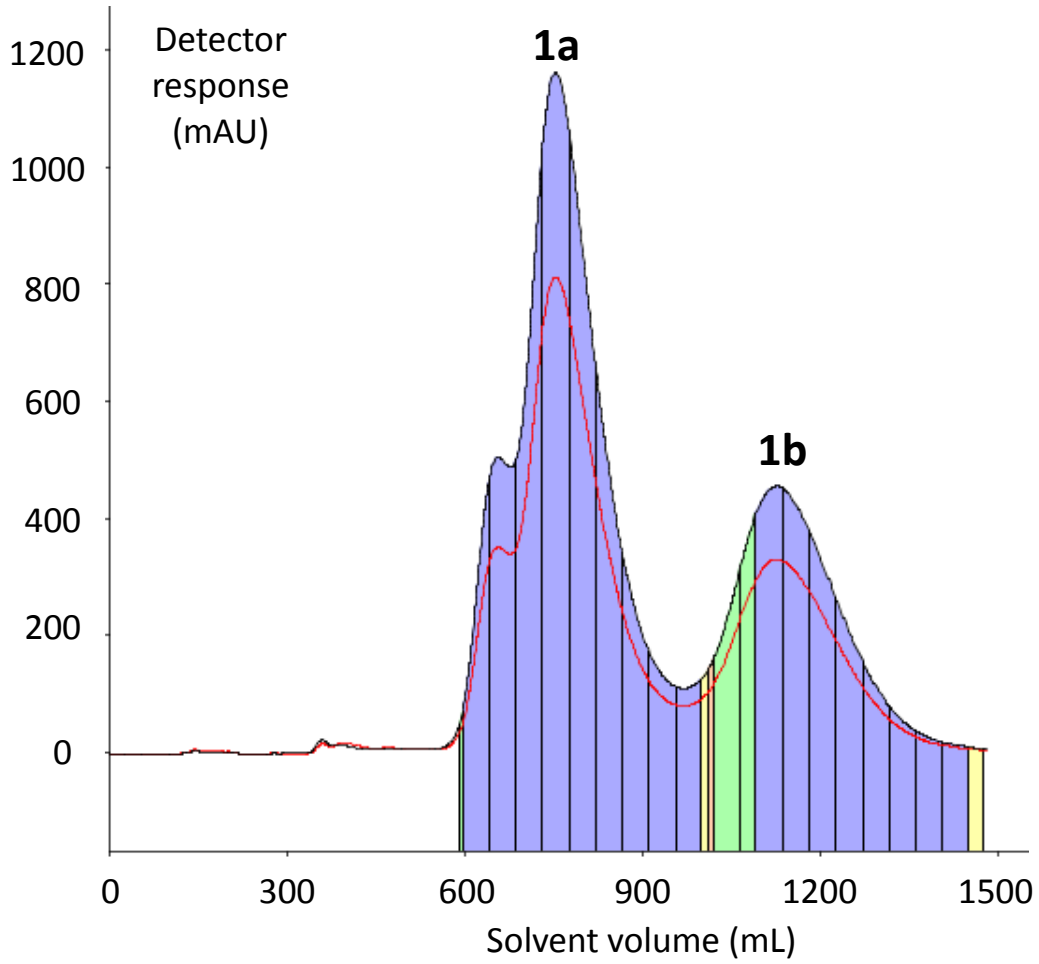


**Figure S19.** Trace of the UV detector output from a Biotage© Isolera flash chromatography system to highlight the diastereomeric ratio of **1a** and **1b** (2:1). The shoulder on band **1a** is an artefact due to imperfect column loading, which is confirmed by $^{1}$H NMR upon combining fractions.

## VT $^{19}$F NMR

As some signals coalescence within the solvent temperature window for **1b**, it is possible to use an approximate method to estimate the rate constants of exchange ($k_{coal}$) at the coalescence temperatures ($T_{coal}$) using Equation S1,[1] where $\delta v_{r.t.}$ is the difference in frequency between the two exchanging environments at room temperature.

$$k_{coal} = \delta v_{r.t.} \frac{\pi}{\sqrt{2}} = 2.22 \delta v_{r.t.} \quad (S1)$$

According to equation S1, for a given coalescence temperature the rate of exchange (rate of pentafluorophenyl rotation in this case) is proportional to $\delta v_{r.t.}$. This makes it even more significant that the signals for **1b** coalesce at below 100 °C while the signals for **1a** do not, as the $\delta v_{r.t.}$ values for **1b** are significantly larger than for **1a** (740 Hz vs. 330 Hz for the 2 and 6 positions, and 835 Hz vs. 550 Hz for the 3 and 5 positions).

For the signals corresponding to the 2 and 6 positions of **1b**, $T_{coal}$ = *ca.* 85 °C and $\delta v$ = 740 Hz. For the signals corresponding to the 3 and 5 positions $T_{coal}$ = *ca.* 95 °C, while $\delta v$ = 835 Hz. Using these values, the approximate rates of exchange at 85 °C and 95 °C for **1b** are calculated to be 1600 $s^{-1}$ and 1900 $s^{-1}$ (2 s.f.), respectively.

Using the same parameters, it is possible to apply the Eyring equation (Equations S2 and S3) to estimate the free energy barrier ($\Delta G^{\ddagger}$) for exchange at the coalescence temperatures.[1]

$$\Delta G^{\ddagger} = RT \left[ 23.76 - \ln\left( {}^{k}/_{T} \right) \right] \quad (S2)$$

$$\Delta G^{\ddagger} = RT_{coal} \left[ 22.96 + \ln\left( {}^{T_{coal}}/_{\delta v_{r.t.}} \right) \right] \quad (S3)$$

Using Equation S3, a $\Delta G^{\ddagger}$ value of 70 kJ $mol^{-1}$ (1 s.f.) is estimated for **1b** from the data obtained at either coalescence temperature. It should be emphasized that this obtained value for the energy barrier is temperature dependent due to the entropy term ($\Delta S^{\ddagger}$) in Equation S4,[1] which may limit its usefulness outside the coalescence temperatures.

$$\Delta G^{\ddagger} = \Delta H^{\ddagger} - T\Delta S^{\ddagger} \quad (S4)$$

Nevertheless, as the rotation of the pendant pentafluorophenyl ring in **1b** is an intramolecular process, and the complex is rather rigid, $\Delta S^{\ddagger}$ may be small. Therefore, while further detailed investigation is required to accurately determine the energy barrier at room temperature, 70 kJ $mol^{-1}$ may be a useful rough figure. It is noted that this value is comparable to the room temperature $\Delta G^{\ddagger}$ values reported by Cozzi and Siegel et al. for rotation of intramolecularly-stacked perfluoroaryl rings in diarylnaphthalenes, which are approximately 80 kJ $mol^{-1}$ (20 kcal $mol^{-1}$).[2,3]

In summary, the intramolecular π–π interactions between the pendant pentafluoroaryl rings and cyclometalating ligands in **1a** and **1b** are strong enough to restrict rotation of the pendant ring in solution. This can be observed through a breakdown in the symmetry of their $^{19}$F NMR spectra. From the room temperature and variable temperature NMR data for both systems, it can be

concluded that the barrier to rotation in **1a** is significantly greater than for **1b**. This is ascribed to stronger intramolecular π–π interactions, in agreement with the XRD data. As some signals coalescence at below 100 °C for **1b**, a value of 70 kJ mol$^{-1}$ could be roughly estimated for $\Delta G^{\ddagger}$, which is comparable to previously reported literature values.

A more accurate value could be achieved through carrying out a complete line shape analysis which involves comparing the line shapes of the spectra at varying temperatures with simulated spectra. However, this can require a large expenditure of time and effort.[1] In the case of **1a** and **1b**, it is qualitatively clear that the energy barrier to rotation of the perfluoroaryl ring is significantly larger for **1a**, which is attributed to more favorable intramolecular π–π interactions. Therefore, the detailed experiments that would be required to determine accurate physical parameters would not provide a hugely significant improvement to our understanding of this system.

## Electrochemistry

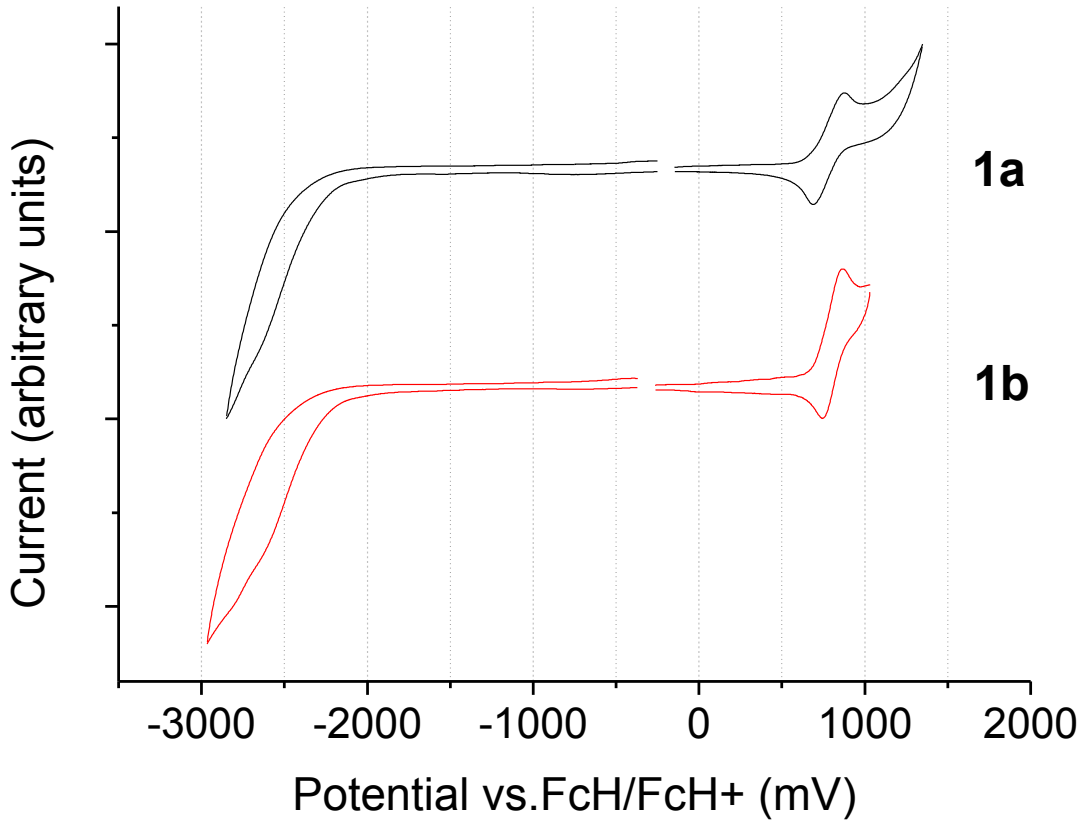


**Figure S20.** Cyclic voltammograms in 0.1 M *n*-$Bu_4NPF_6$/ THF showing the oxidation and reduction processes for complexes **1a** and **1b**.

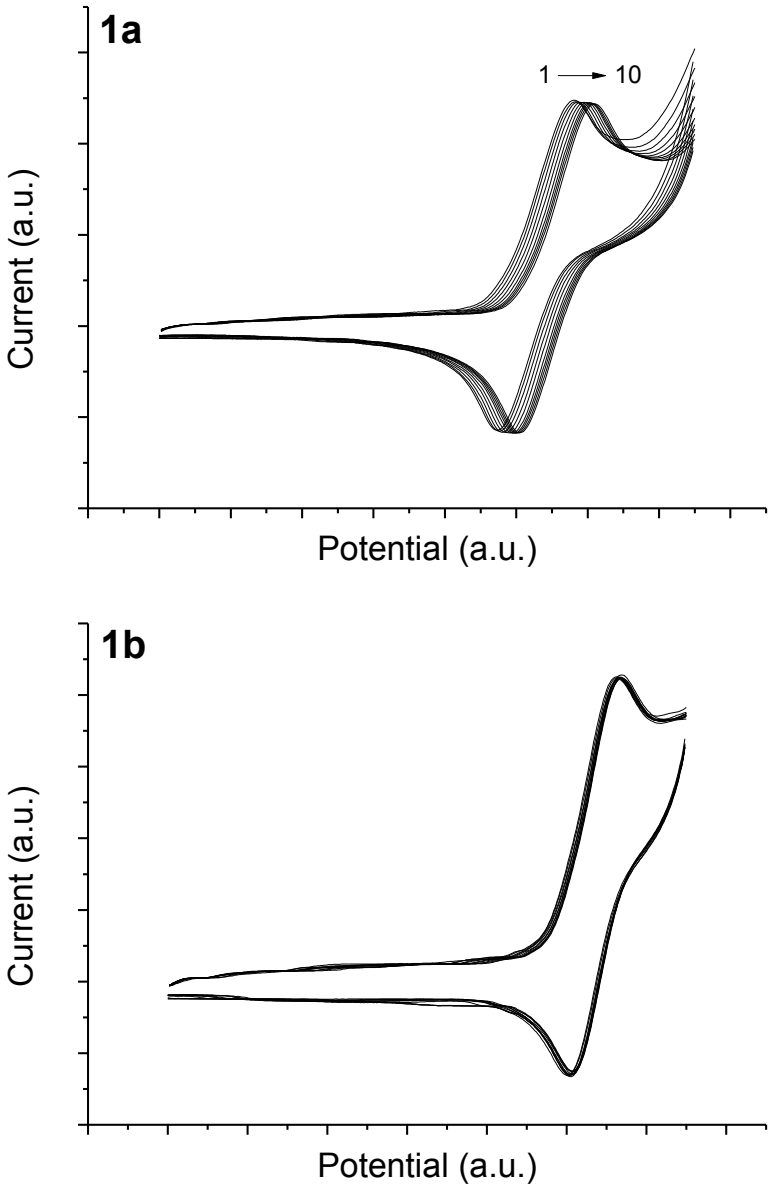


**Figure S21.** Cyclic voltammograms in 0.1 M *n*-$Bu_4NPF_6$/ THF showing the oxidation processes for complexes **1a** and **1b** over 10 consecutive scans. The potential axis is arbitrary due to the absence of internal ferrocene. The oxidation potentials slightly drift due to the use of a quasireference electrode.

## Photophysics

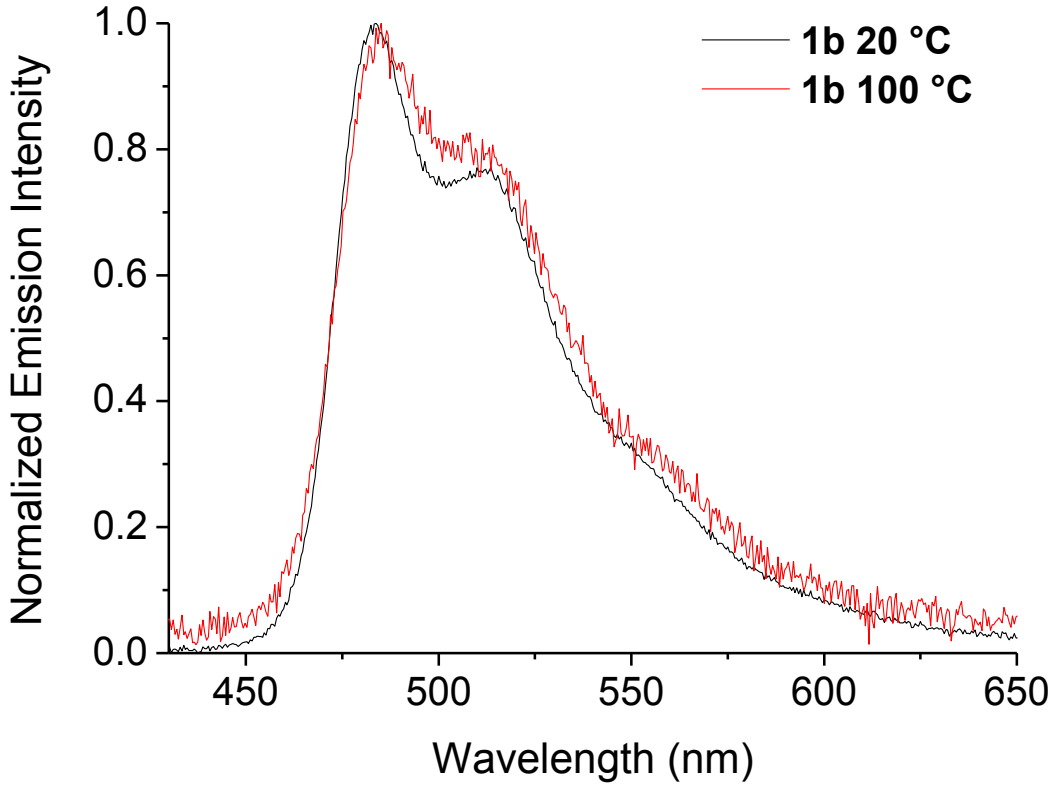


**Figure S22.** Normalized emission spectra for **1b** recorded in degassed xylenes at 20 °C and 100 °C. Temperatures are ± 5°C.

**DFT**

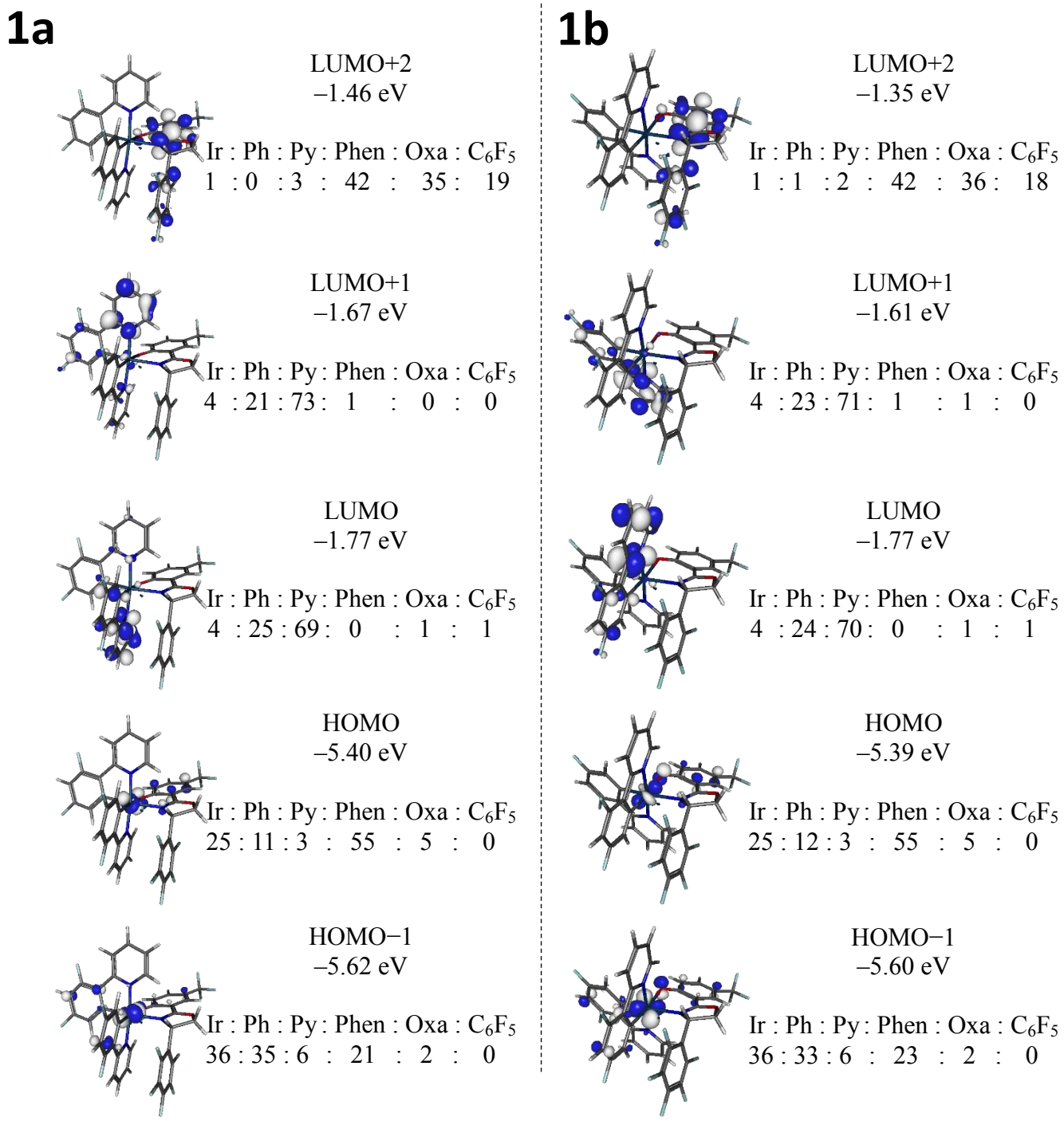


**Figure S23.** Molecular orbital compositions for **1a** and **1b**. The orbital contributions are percentages and the orbital energies were calculated at B3LYP/LANL2DZ:6–31G*. Phen = ancillary ligand phenoxy group; Oxa = auxiliary ligand oxazole group; Ph = cyclometalating ligand phenyl groups; Py = cyclometalating ligand pyridyl groups; $C_6F_5$ = pendant pentafluorophenyl.

**Table S1.** Orbital contributions for complexes **1a** and **1b**.

| Complex | Orbital | Ir | Ph[a] | Py[b] | Phenoxy | Oxazoline | $C_6F_5$[c] |
|---|---|---|---|---|---|---|---|
| | LUMO+2 | 1% | 0% | 3% | 42% | 35% | 19% |
| | LUMO+1 | 4% | 21% | 73% | 1% | 0% | 0% |
| **1a** | LUMO | 4% | 25% | 69% | 0% | 1% | 1% |
| | HOMO | 25% | 11% | 3% | 55% | 5% | 0% |
| | HOMO-1 | 36% | 35% | 6% | 21% | 2% | 0% |
| | LUMO+2 | 1% | 1% | 2% | 42% | 36% | 18% |
| | LUMO+1 | 4% | 23% | 71% | 1% | 1% | 0% |
| **1b** | LUMO | 4% | 24% | 70% | 0% | 1% | 1% |
| | HOMO | 25% | 12% | 3% | 55% | 5% | 0% |
| | HOMO-1 | 36% | 33% | 6% | 23% | 2% | 0% |

[a]Phenyl moieties of the cyclometallating ligands; [b]Pyridyl moieties of the cyclometallating ligands; [c]Pendant pentafluorophenyl group of the ancillary ligand

## TD-DFT

The lowest energy singlet and triplet states were also investigated at the $S_0$ geometries for **1a** and **1b**. The data for the three lowest energy triplet and singlet excited states for each complex are tabulated in Table S2. The dominant transitions contributing to each state (≥ *ca.* 20%) are included. The transitions to the lowest energy singlet states ($S_0 \rightarrow S_1$) for each complex primarily consist of HOMO → LUMO transitions, while the transitions to the second and third singlet states ($S_0 \rightarrow S_2$ and $S_0 \rightarrow S_3$) also involve the LUMO+1 and HOMO−1 orbitals. This is in good agreement with the data for literature analogues.[3]

For each of the complexes **1a** and **1b**, there are three triplet states within *ca.* 20 nm of each other, while the two lowest energy triplet states are within *ca.* 10 nm. From consideration of the lowest 2/ 3 triplet states of the complexes it is evident that their emissive states are likely to be broadly delocalized, with mixed LC (on both the cyclometalating and auxiliary ligands), MLCT (metal → cyclometalating ligand/ auxiliary ligand) and ILCT (auxiliary ligand → cyclometalating ligand) character. For **1a** the transition to the lowest energy triplet state ($S_0 \rightarrow T_1$) is primarily of HOMO → LUMO+2 character, while the second triplet state ($S_0 \rightarrow T_2$) involves both HOMO−1 → LUMO and HOMO → LUMO transitions. For **1b** the same transitions are involved, although the ordering of the states is inverted (Table S2). The small variation observed in the spectral profiles of **1a** and **1b**, most prominent in PMMA, may be related to this. However, as the experimentally determined photophysical parameters for **1a** and **1b** ($\lambda_{max}$, $E_T$, PLQY and $\tau$) are very similar, it is likely that their emission originates from analogous states. Therefore, the inversion of the character of the $S_0 \rightarrow T_1$ and $S_0 \rightarrow T_2$ transitions in the TD-DFT may not be significant.

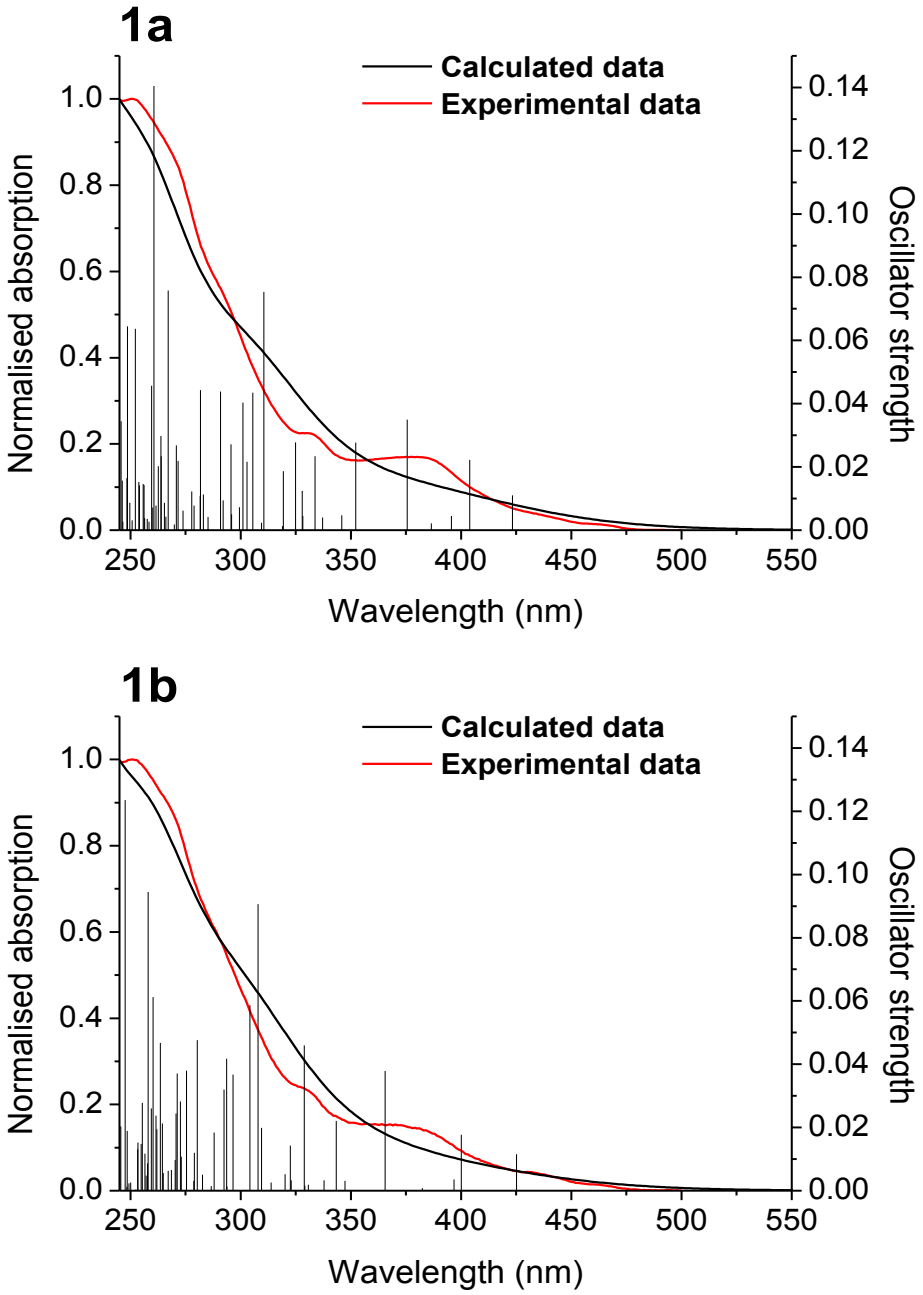


**Figure S24.** Simulated and experimental absorption spectra for complexes **1a** and **1b**. Experimental data were obtained in aerated DCM.

**Table S2.** Summary of the TD-DFT data for complexes **1a** and **1b**.

| Transition | 1a | | 1b | |
|---|---|---|---|---|
| | **Main orbital contribution** | **λ/ nm (*f*)** | **Main orbital contribution** | **λ/ nm (*f*)** |
| $S_0 \rightarrow T_1$ | HOMO → LUMO+2 | 463 | HOMO-1 → LUMO, HOMO→ LUMO | 460 |
| $S_0 \rightarrow T_2$ | HOMO-1 → LUMO, HOMO→ LUMO | 456 | HOMO → LUMO+2 | 449 |
| $S_0 \rightarrow T_3$ | HOMO-1 → LUMO+1 | 442 | HOMO-1 → LUMO+1 | 440 |
| $S_0 \rightarrow S_1$ | HOMO→ LUMO | 423 (0.011) | HOMO→ LUMO | 425 (0.012) |
| $S_0 \rightarrow S_2$ | HOMO → LUMO+1 | 404 (0.022) | HOMO-1 → LUMO, HOMO → LUMO+1 | 400 (0.018) |
| $S_0 \rightarrow S_3$ | HOMO-1 → LUMO | 395 (0.005) | HOMO → LUMO+1, HOMO-1 → LUMO | 397 (0.004) |

[a] $f$ = oscillator strength. It is only included for singlet transitions as it is zero for all triplet transitions. All listed orbital contributions are ≥ 20%.

# TGA

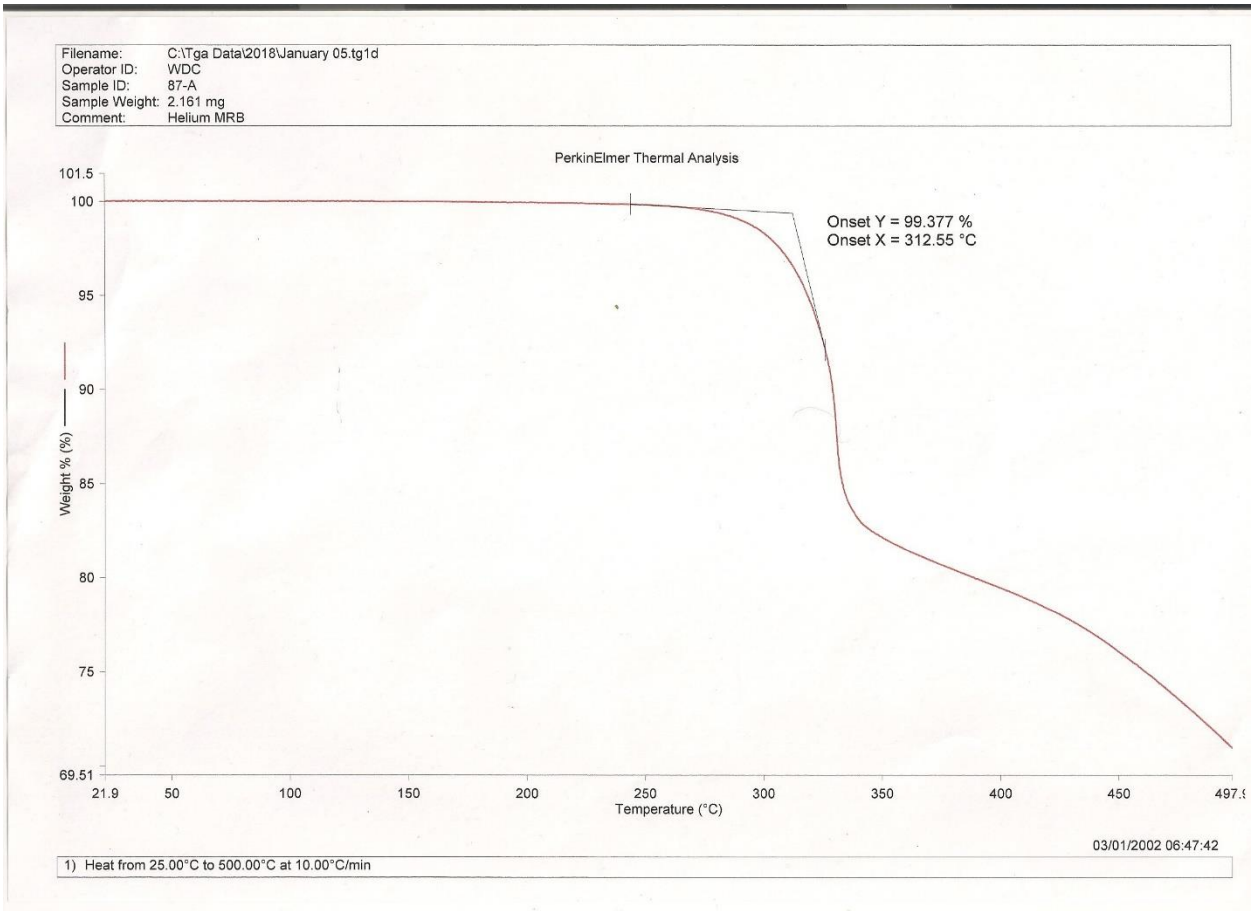


**Figure S25.** TGA trace for **1a.**

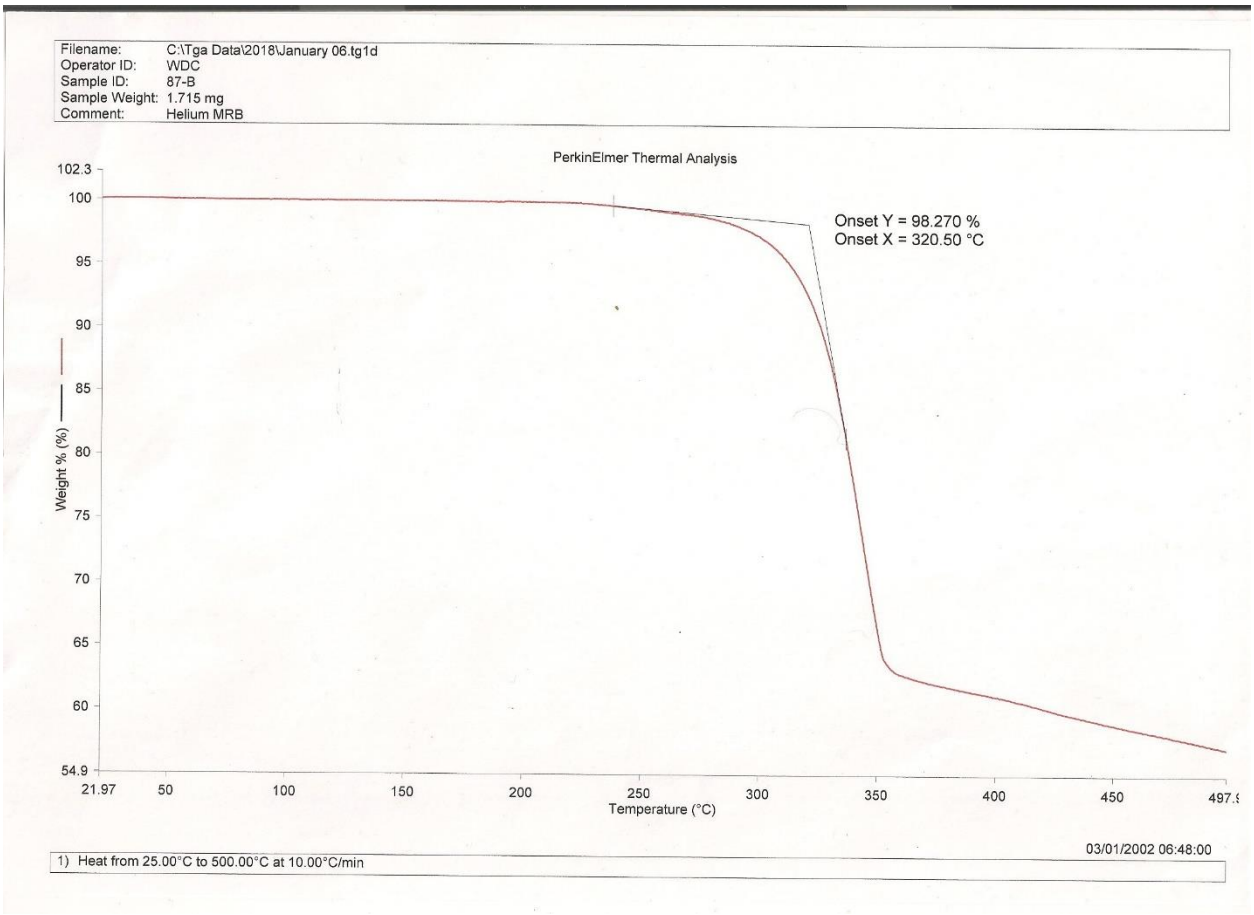


**Figure S26.** TGA trace for **1b.**

## PhOLEDs

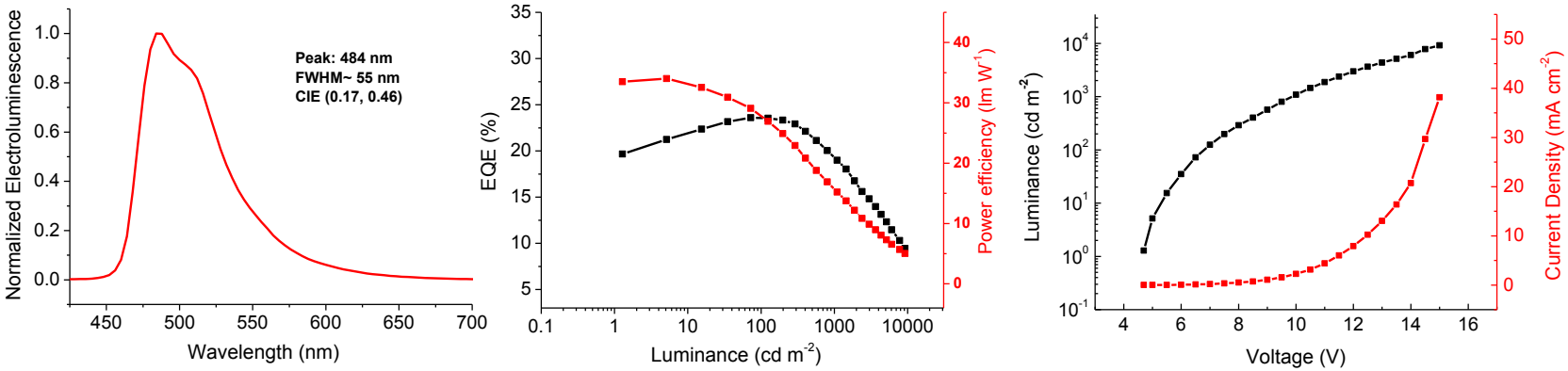


**Figure S27.** PhOLED device data (3.5 wt%) for **1a**. (left) EL spectrum at a luminance of 100 cd $m^{-2}$. (middle) External quantum efficiency and power efficiency curves vs. voltage. (right) Luminance and current density curves vs. voltage.

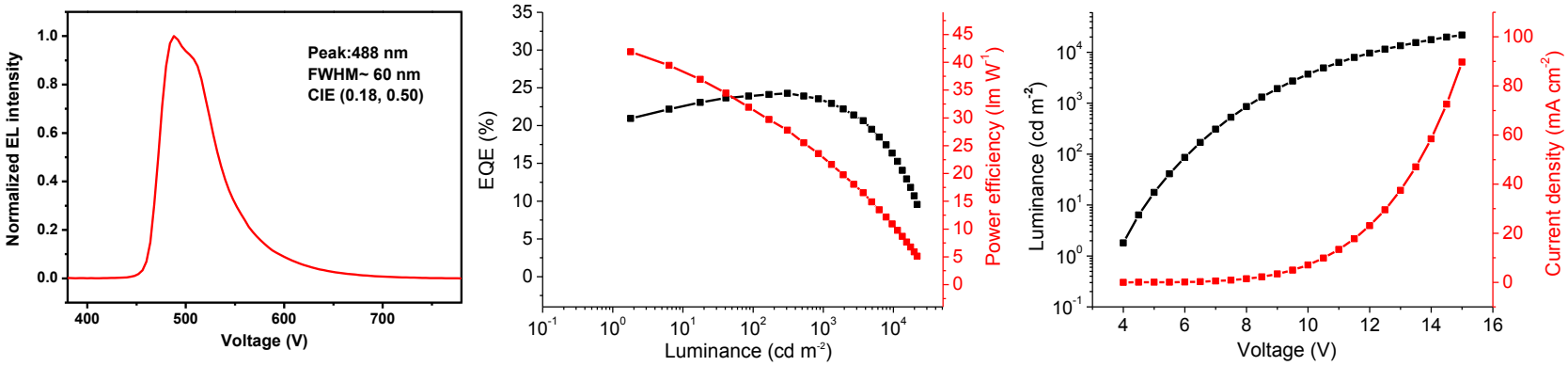


**Figure S28.** PhOLED device data (15 wt%) for **1a**. (left) EL spectrum at a luminance of 100 cd $m^{-2}$. (middle) External quantum efficiency and power efficiency curves vs. voltage. (right) Luminance and current density curves vs. voltage.

## X-ray Crystal Structures

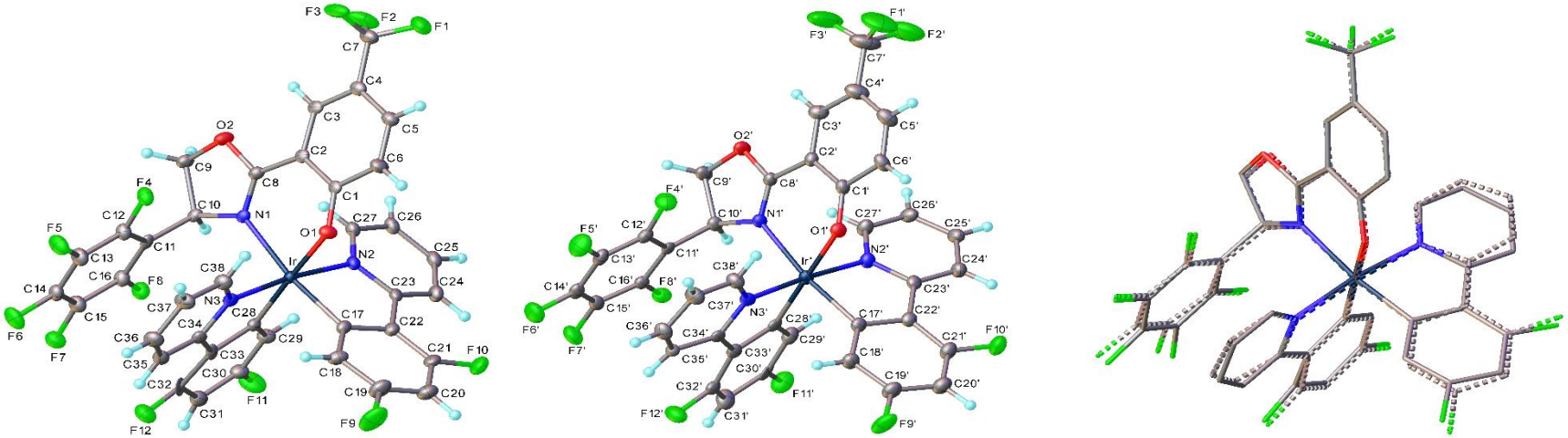


**Figure S29.** Two independent molecules in the structure of **1a** and their overlay (H atoms omitted).

## References


(1) Günther, H. *NMR Spectroscopy: Basic Principles, Concepts and Applications in Chemistry*, 2nd Edition.; John Wiley & Sons: Chichester, 1995.

(2) Cozzi, F.; Cinquini, M.; Annuziata, R.; Siegel, J. S. Dominance of Polar/pi over Charge-Transfer Effects in Stacked Phenyl Interactions. *J. Am. Chem. Soc.* **1993**, *115*, 5330–5331.

(3) Cozzi, F.; Ponzini, F.; Annunziata, R.; Cinquini, M.; Siegel, J. S. Polar Interactions between Stacked Pi Systems in Fluorinated 1,8-Diarylnaphthalenes: Importance of Quadrupole Moments in Molecular Recognition. *Angew. Chem. Int. Ed. Engl.* **1995**, *34*, 1019–1020.